The Effects of Build Orientation on Residual Stresses in AlSi10Mg Laser Powder Bed Fusion Parts

by

Jared A. Clark

Submitted in Partial Fulfillment of the Requirements

for the Degree of

Master of Science in Engineering

in the

Mechanical Engineering

Program

YOUNGSTOWN STATE UNIVERSITY

December, 2019

The Effects of Build Orientation on Residual Stresses in AlSi10Mg Laser Powder Bed Fusion Parts

Jared A. Clark

I hereby release this **thesis** to the public. I understand that this **thesis** will be made available from the OhioLINK ETD Center and the Maag Library Circulation Desk for public access. I also authorize the University or other individuals to make copies of this thesis as needed for scholarly research.

Signature:

_____

Jared A. Clark, Student Date

Approvals:

_____

Dr. Jason Walker, Thesis Advisor Date

_____

Dr. Brett Conner, Committee Member Date

_____

Dr. C. Virgil Solomon, Committee Member Date

_____

Dr. Salvatore A. Sanders, Dean of Graduate Studies Date

ABSTRACT

Additive manufacturing is one of the more recent advances in manufacturing technology. Additive manufacturing processes allow for the creation of parts in a layer-by-layer fashion. There are several materials that can be used in additive manufacturing processes including metal, ceramic, and polymers which each presenting their own challenges. This work focuses on metal based additive manufacturing parts made out of AlSi10Mg using a process called laser powder bed fusion. Laser powder bed fusion is one of the three major metal additive manufacturing processes with the other two being multi-pass welding and direct energy deposition. One of many challenges that occur with the laser power bed fusion process is minimizing the residual stresses and distortion that are present in the part during and after the build. During the early days of additive manufacturing that was mostly done through a trial-and-error process where multiple version of a part would be printed until a desired outcome was achieved, and this was often very expensive, and time consuming. There has been plenty of research in developing simulation models in order to predict the distortions and stresses that developed during the additive manufacturing process. These simulations allowed engineers to optimize parts before they were printed, and thus reduce the number of wasted prints. This work demonstrates and validates use of a software package call Autodesk Netfabb Simulation in order to find the optimal orientation of a complex part. The optimal orientation was selected for three categories: distortion, stress, and printability. Optimal orientations were selected from a selection of 23 orientations that were simulated. To validate the simulations, two test parts along with three of the aforementioned orientations were printed and measured using 3D scanning while still the build plate. The result of this was that the optimal orientation was different for each of three criteria meaning it is up to the part application to decide which one is best, and measurement techniques used yielded inconclusive results.

ACKNOWLEDGEMENTS

I would like to thank the following people for making this thesis possible.

- Dr. Walker: Thesis Advisor, and my boss during the research project
- Dr. Solomon: Academic Advisor, Committee Member, and helped me through my graduate years
- Dr. Conner: Committee Member, and the person that originally hired me on the research job
- Dr. Marie: Chair of Mechanical Engineering Department, connected me with Dr. Conner, and was extremely helpful during my undergraduate years
- Dean Sanders: Dean of the College of Graduate Studies
- Eric Dillinger, Michael Gouge, and Sulap Ozel: For helping me with the Netfabb software

TABLE OF CONTENTS

LIST OF FIGURES

LIST OF TABLES

NOMENCLATURE

Abbreviations

AM	Additive Manufacturing
3D	Three-Dimensional
CaP	Calcium Phosphate
Al	Aluminum
Zr	Zirconium
L-PBF	Laser Powder Bed Fusion
DED	Direct Energy Deposition
FEA	Finite Element Analysis
SMAW	Shielded Metal Arc
GMAW	Gas Metal Arc Welding
MIG	Gas Metal Arc Welding
GTAW	Wire Fed Tungsten Inert Gas Welding
TIG	Wire Fed Tungsten Inert Gas Welding
FCAW	Flux Corded Arc Welding
SAW	Submerged Arc Welding
HAZ	Heat Affected Zone
HPL	High-Powered Laser
EBEAM	Electron Beam
HSE	Heat Source Efficiency
LENS™	Laser Engineered Net Shaping
CNC	Computer Numerical Control
CAD	Computer Aided Drafting
AS	Aluminum-Silicon
TGM	Thermal Gradient Mechanism
MLCDP	Melted Top Layer Cool Down Phase
CMM	Coordinate Measuring Machine
FE	Finite Element
3mf	3D Manufacturing Format
POI	Point of Interest
POIs	Points of Interest
STL	Standard Tessellation Language
SLDPRT	SolidWorks Part
FHT	Fake Heat Treatment
PTS	Plasticity Time Step
UTS	Ultimate Tensile Strength
BRMC	Build's Minimum Recoater Clearance
SRTS	Substrate Removal Time Step
MPLPD	Maximum Previous Layer Protrusion Distance
GCX	Geomagic Control X
DXF	Drawing eXchange Format

Variables/Vectors/Matrices

$\boldsymbol{U}_{i+1}$	nodal solution vector either temperatures or displacements of the current iteration
$\boldsymbol{U}_i$	nodal solution vector of either temperatures or displacements of the previous iteration
$\boldsymbol{R}_i$	residual vector for the previous iteration
$\boldsymbol{U}_0$	initial guess for the nodal solution
$\boldsymbol{R}$	residual vector
$\frac{d\boldsymbol{R}_i}{d\boldsymbol{U}}$	stiffness matrix for the previous iteration
T	temperature
t	time
$\nabla \cdot$	divergence
$\boldsymbol{q}$	heat flux
$\boldsymbol{r}$	relative reference temperature
Q	body heat source
k	isotropic temperature dependent thermal conductivity
∇	gradient
T_0	initial temperature
T_∞	ambient temperature or the preheat temperature of the build plate
P	heat source power
η	heat source efficiency
a	width in the of the ellipsoid in the x-direction
c	length of the ellipsoid in the z-direction
b	depth of the ellipsoid in the y-direction
v_s	speed of the heat source
S_q	surface where the heat flux is applied
q_{conv}	convective heat flux
h	heat transfer coefficient
T_s	surface temperature at the boundary
h_{free}	heat transfer coefficient due to natural or free convection
h_{forced}	heat transfer coefficient due to forced convection
h_{rad}	heat transfer coefficient due to radiation
ε_{rad}	surface emissivity
σ_{SB}	Stefan-Boltzmann constant
$\boldsymbol{\sigma}$	stress vector
$\boldsymbol{C}$	fourth order material stiffness tensor
$\boldsymbol{\varepsilon}_e$	elastic strain
$\boldsymbol{\varepsilon}$	total stain
$\boldsymbol{\varepsilon}_T$	thermal strain
$\boldsymbol{\varepsilon}_p$	plastic strain
$\boldsymbol{\alpha}$	thermal expansion coefficient
T_{ref}	reference temperature

f_Y	yield function
σ_{vm}	Von Mises stress
σ_Y	yield strength
$\boldsymbol{\varepsilon}_q$	equivalent plastic strain
$\boldsymbol{\alpha}_{flow}$	flow vector
$\Delta_{\%,x}$	percentage difference for the x-displacement
$\delta_{x,i}$	x-displacement for the new mesh
$\delta_{x,i-1}$	x-displacement for the previous mesh
$\Delta_{\%,y}$	percentage difference for the y-displacement
$\delta_{y,i}$	y-displacement for the new mesh
$\delta_{y,i-1}$	y-displacement for the previous mesh
$\Delta_{\%,z}$	percentage difference for the z-displacement
$\delta_{z,i}$	z-displacement for the new mesh
$\delta_{z,i-1}$	z-displacement for the previous mesh
$B_{p,max}$	MPLPD
$C_{r,min}$	BMRC
t_l	layer thickness
$\boldsymbol{G}_{GCX}$	GCX gap distortion vector
$\boldsymbol{\delta}_N$	Netfabb distortion vector
$\|\boldsymbol{G}_{GCX}\|$	magnitude of the GCX gap distortion vector
$\boldsymbol{G}_N$	Netfabb gap distortion vector
$(GD)_N$	Netfabb gap distance
E_{GD}	gap distance error
$(GD)_{GCX}$	GCX gap distance
$(PE)_{GD}$	gap distance percentage error
$(PE)_Z$	z-displacement percentage error
Z_v	measurement made by the Vernier height gauge
δ_x	x-displacement
δ_y	y-displacement
δ_z	z-displacement
σ_{xx}	XX Cauchy stress
σ_{yy}	YY Cauchy stress
σ_{zz}	ZZ Cauchy stress

CHAPTER 1 :
INTRODUCTION AND BACKGROUND

1.1: Introduction to Additive Manufacturing

One of the most recent advancements in manufacturing technology is the creation of Additive manufacturing (AM) also known as three-dimensional (3D) printing. Compared to a lot of manufacturing technologies the use of 3D printing is fairly recent starting about 40 years ago, though public interest in 3D printing is more recent then that. 3D printing is essentially the process of creating a part by adding material together, and for the majority of 3D printing process the act of adding material is done in layer-by-layer fashion were layers of material are placed on top each other until the part is completed. A layer being a horizontal slice, or a cross section in which its normal direction is parallel to build direction, of the final part with specified thickness usually having the order of magnitude of micrometers (microns) [1]. Parts made using 3D printing can be made of a variety of materials such as polymers, ceramics, and metals [[2]-[4]]. In reference to polymer 3D printing, Christopher Xu Fu Lam *et al.* [2] used a blend of cornstarch, dextran, and gelatin all of which are starch based polymer powders to order to create scaffold geometries. For ceramic 3D printing, Ryan Trombetta *et al.* [5] studies the 3D printing of scaffolds made of calcium phosphate (CaP) which are used for applications pertaining to bone tissue engineering. For an example of the use metal 3D printing, John H. Martin *et al.* [4] printed parts made of 7075 aluminum (Al), and 6061 Al mixed with zirconium (Zr) particulates to show that the addition of Zr particulates make the two aforementioned alloys able to be used for printing. The main emphasis for this work will be metal 3D printing using a process called laser powder bed fusion (L-PBF). L-PBF is one of the three major processes of metal 3D printing, the other two being multi-pass welding, and direct energy deposition (DED) [[6]-[9]].

1.1.1: Multi-pass Welding

The oldest of the three major metal 3D printing processes was multi-pass welding. Multi-pass welding can create freeform structure as well as join, fill, or even repair parts, and the ability to make part using freeform techniques is what makes it a metal 3D printing process despite the fact that more commonly known 3D printing machines of today are not used [[6], [7]]. Research on multi-pass welding has been a topic of research since the 1970s and has continued on to present day [[6], [7], [10]-[12]]. Yukio Ueda *et al.* [6] studied multi-pass welded joints between the head and the cylinder of pressure vessels before and after a stress reliving process in terms of residual stress using experimental and theoretical methods. R.E. Nickell and H.D. Hibbitt [7] discussed various factors involving the use of finite element analysis (FEA) programs to find the residual state of stress and deformation in a welded structure and applied that analysis to an omega weld seal. Yukio Ueda *et al.*

[10] analyzed transient and residual stresses and strains caused by the act of multi-pass welding connections for a pressure vessel with 167 passes. Yukio Ueda *et al.* [11] preformed a study on the effect of the narrow gap arc welding method of multi-pass welding on SM-50 steel plates in terms of the creation of residual stresses and deformations by the use of finite element method based thermal elastic-plastic analysis. Lars-Erik Lindgren *et al.* [12] compared the use of two different FEA approaches active and inactive elements to simulate a 28-pass multi-pass butt weld, and described the advantages and disadvantages of each FEA method.

There are several common of multi-pass welding types, the most common of these are: shielded metal arc welding (SMAW), gas metal arc welding (GMAW or MIG), wire fed tungsten inert gas welding (GTAW or TIG), flux corded arc welding (FCAW), and submerged are welding (SAW) [[13]-[17]]. In Ref. [13], Brickstad and Josefson conducted a parametric study of stainless steel piping systems that either was welded by a multi-pass TIG, SMAW, or SAW in order to propose a procedure for calculating a residual stress fields generated by multi-pass butt-welds. In Ref. [14], Heinze *et al.* performed experimental and numerical investigation of residual stresses generated by the welding of two 20 mm thick structural steel S355J2+N plates with a multi-pass GMAW. In Ref. [15], Mirshekari *et al.* studied the hardness, microstructure and corrosion behavior of the welding of 304L stainless steel by single-pass GTAW and multi-pass GTAW. In Ref. [16], Zhang *et al.* investigated the effects using GTAW and FCAW to create duplex stainless steel welding joints in terms of microstructure, impact toughness, and corrosion resistance. Kolhe and Datta [17] studied multi-pass SAW weld of a 16 mm thick mild steel plate in terms of its microstructure, phase, phase properties, mechanical properties, and heat affected zone (HAZ) width. One of the major issues with the multi-pass welding process was that the freeform builds created using the multi-pass welding process were not accurate nor repeatable, because of the manual nature of the process [1].

1.1.2: Direct Energy Deposition (DED)

After the use multi-pass welding to create metal 3D printed parts, the next 3D printing process was DED, and these machines first came about in the 1980s [18]. The DED process uses a machine that melts a metallic material that is in either wire or powder form by a computer controlled heat source, and the heat source is either a high-powered laser (HPL) or an electron beam (EBEAM) [[19]-[20]]. In Ref. [19], Keist and Palmer studied effects that geometry has on the microstructure, and mechanical properties that resulted from the printing of several wall structures made out of Ti-6Al-4V using a DED machine with a laser heat source. In Ref. [20], Al-Bermani *et al.* used a DED machine with an EBEAM heat source in order to print samples of Ti-6Al-4V to study the microstructure, texture, and mechanical properties of those samples. There are serval differences between the laser and EBEAM heat sources. First, DED machines with laser heat source have

throughput powers that range from 100 to 5000 W, while DED machines with EBEAM heat sources have throughput powers that extend up to 10,000 W [[18], [21], and [22]]. Second, laser-based DED machines can make parts either in open air or in a closed chamber with the close chamber variation being chosen in order to prevent atmospheric contamination of metals while in a molten state by the filling the chamber with an inert gas [23]. On the other hand, EBEAM-based DED machines can only produce parts in a vacuum environment, meaning the other two methods heat transfer from the heat source are radiation and conduction [24]. Third, laser-based DED machines have 30 to 50 percent heat source efficiency (HSE) which is far lower than the EBEAM-based DED machines, which have an HSE of 90 to 95 percent. HSE is defined as how much heat from the heat source is being absorbed by the build [[22], [25], and [26]].

The start of the popularity of the DED process in industry can be attributed to the building of the first laser engineered net shaping (LENS^{TM}) machines by Sandia National Laboratories. In addition, compared to many traditional manufacturing methods, particularly casting, LENS^{TM} machines offered near-net shape parts for a lower cost, which in turn made them an attractive alternative for manufactures [[27]-[29]]. DED machines use a variety of motion controllers, the most common of which are 3-axis systems such as the LENS^{TM} machines. The 3-axis controllers found in a LENS^{TM} machine only allow movement along the primary axes of a Cartesian coordinate system (x, y, or z) [[27], [30]]. In addition, DED machines that use a similar process utilize layer-by-layer deposition to create a variety of parts. However, there are some DED systems called multi-axis systems that have anywhere from four to six degrees of freedom, and the extra one to three degrees of freedom comes from adding one to three rotational axes on top of the 3-axis system. The rotational degrees of freedom are accomplished by a combination of rotating the deposition head and rotating the build platform. The use of a multiaxis DED machine allows for an increased range of possible part geometries and allows the deposition of material to be in any direction. Compared to multi-pass welding, parts made by the DED process are more repeatable and accurate, and this in turn helped push the DED process into industry. The main reason for increased accuracy and repeatability of the DED process over multipass welding is that multi-pass welding typically was performed by a human operator instead of using numerical control like in the cases of the DED process [1].

1.1.3: Laser Powder Bed Fusion (L-PBF)

After the DED machines, another metallic AM innovation that came along was the L-PBF machines, which come in several variations. In short, the L-PBF process involves printing a part by the use a small heat source that move quickly to melt potions of a layer of powder that was spread across the build plate beforehand [[31]-[33]]. The heat sources used for L-PBF machines are either a laser or an EBEAM. The power for the laser heat source comes from a coherent light source, while the power for the EBEAM heat source

come from an electron current source [34]. The procedure used for the L-PBF process is as follows. First, a layer of metallic powder is placed on the build plate. Second, a heat source is used to melt then solidify the powder to form a layer of the part. Third, a new layer of power is swept across the build plate by a recoater blade after the plate has been lowered by one-layer height. Fourth, steps two and three are completed until the part is finished [9]. Once the L-PBF machines were standardized, the 3D printing processes became more deeply adapted in industry [1].

There are several of noteworthy differences between the DED processes and L-PBF processes. First, DED machines fed the metal powder directly into the melt pool, while for L-PBF machines the metallic powder is preplaced [32]. Second, the diameter of the heat sources used in L-PBF machines are a $1/10^{th}$ to $1/20^{th}$ the size as those used in DED machines. The smaller heat source also means that L-PBF machines can produce parts at much higher resolution than their DED counterparts can. Third, L-PBF uses a throughput power ranging from 100 to 250 W, which is significantly smaller than the throughput power range of DED machines. Fourth, L-PBF machines typically are able to move their heat sources at speed ranging between 500 to 1000 mm/s, which is a direct result of the material deposition speeds being 50 to 100 times faster than a common DED machine [35]. Fifth, L-PBF process is less of a hassle to setup the DED because the L-PBF machine need only a computer aided drafting (CAD) source file for the part and a printer processing (i.e. slicing) software in order to print part, while DED machines require an Computer Numerical Control (CNC) machine code that is manually written. The printer processing software splits up the part file into the layers and with minimum effort the software grants the user a great level of control over the build. Sixth, unlike DED machine builds, L-PBF machines have two additional components to them: support structures, and the recoater blade [1].

To assist in the reduction of the part distortion of L-PBF parts, support structures, or just supports, are used, and these structures are usually sacrificial low volume builds [36]. In the L-PBF process, the supports usually consist of lattice structure with thin walls. Additionally, the thin walls are attached to the part by a limited number of connections that are frequently in the shape of a sawtooth. The method in which the supports of the build reduce the distortion of a part is by holding down the part to the build plate and conducting heat away from part while the material is being deposited. The sacrificial nature of the build supports stems from the fact that after the build is completed the support structure is removed from the build plate first followed by the part. Once removed, the supports are then discarded or recycled. Sometimes the stresses that are incurred during the L-PBF building process are so immense that the weaker areas of the support structure will break away from the build plate or the part, and this event is categorized as a support structure failure [37].

1.2: AlSi10Mg

AlSi10Mg comes from an aluminum-silicon (AS) family of alloys [38]. These alloys are known to perform well in terms of castablity, weldability, and corrosion resistance. Industries that use AS alloys include automotive and aerospace, and the reason for their use in these industries is due to a combination of mechanical properties, high heat conductivity, and low weight [39]. The Mg portion of the AlSi10Mg alloy stems from the alloying process of AS alloy where precipitates of Mg_2Si are added, and the purpose of the precipitate is to improve the strength of the alloy while other mechanical properties remain unaffected. The amount of Mg in the AlSi10Mg in terms of weight percentage (wt. %) ranges from 0.4 to 0.6, and when a specific heat treatment is applied the alloy will harden because of the Mg_2Si participate [40]. AlSi10Mg is known to have a small solidification range due to it having a near-eutectic composition of Al and Si, which makes this alloy easy to process for laser applications [41]. In terms of L-PBF machines, powders that consist of aluminum offer high geometrical freedom allowing it to be in the creation of complex structures and structures with internal cavities [42].

Compared to other material powders used in the L-PBF process, aluminum powder has higher reflectivity, higher thermal conductivity, and lower flowability. This is shown in detail in Table 1 below where Ti64, Stainless Steel 316, Al6061, and AlSi10Mg are compared. Because of the high thermal conductivity, aluminum-based materials tend to dissipate heat more rapidly than other L-PBF materials, and thus require a higher laser to overcome this heat dissipation as melt the powder. However, the heat dissipation effects of aluminum are less common in its powder form and more common in solid form like what would be used for the build plate [43].

Table 1: Comparing Al-based L-PBF materials against other L-PBF materials [43]

L-PBF Material	Flowability (s/(50g))	Thermal Conductivity (W/ (m*K)	Reflectivity (%)
Ti64	47	6.4 [44]	53-59 [45]
Stainless Steel 316	14.6	21.4 [46]	60 [47]
Al6061	77	172 [46]	91 [48]
AlSi10Mg	No Flow	146 [46]	91 [48]

In Table 1, the flowability data values are experimentally determined using the testing methods from ASTM standard B213-13 [[43], [49]]. Another property that aluminum alloys have is that they oxidize easily, and oxidization tends to create porosity in a given L-PBF build [[50], [51]]. Inside the L-PBF build chamber, AlSi10Mg is known to have a convective heat transfer coefficient of 80 W/ (m^2K), this value be used later in this work (see Section 2.2.3) [52].

1.3: Residual Stress

One of the largest issues when it comes to 3D printed metal parts is minimizing residual stress. In short, residual stress are internal stresses that are brought on by expansion and contraction of both the added material and the existing component, and these stresses can lead to permanent warping of the part [[22], [53]]. In the case of 3D printing, the expansion and contraction is caused by the melting of a layer of material on top of a lager cooler body mostly consisting of previously added layers [1]. During post-processing by either machining or heat treatment, residual stresses cause additional deformation or cracking of the component, and residual tensile stress near the surface can reduce the fatigue strength of a component [53].

Thermal gradient mechanism (TGM) is one of the mechanisms that can cause residual stress. TGM causes a steep temperature gradient around the point-of-contact between the laser and the material due to the laser rapidly heating the upper surface for of the component, or in the case of 3D printing machines the top surface of the upper-most area. In addition, the heating also causes a reduction of material strength. This would not be a large issue if the heated top layer could freely expand by in the case of most 3D printing processes the layers underneath the top layer restrict the top layer which induces compressive strains. The strains start out as elastic that often time will turn plastic due the material yield strength being reached or passed. The top layer of the final part will bend away from the laser beam (or in the negative z-direction) in a convex fashion, because of the lack of mechanical constants on the layer. However, the top layers will bend upwards toward the laser beam (positive z-direction) during the cooling of the printed component because upper layers shrink while being cooled. In the L-PBF process, the deposited material does not have to be molten for this to occur. Another mechanism that causes residual stress is the melted top layer cool down phase (MLCDP). During the MLCDP the melted top layers of the build suffers from thermal contraction, which causes them to shrink. This often will cause tensile stress in those layers due the shrinkage being inhibited by the previously solidified material [54].

There has been a variety of research in terms investigating residual stresses for various scenarios involving each of the three major metal 3D printing processes. However, for the scope of this work, the following examples will mainly be on studies based on L-PBF machines. Ganeriwala *et al.* [55] studied the effect of four different scanning strategies on residual stress using simulation software and by printing four parts made of Ti-6Al-4V using L-PBF, one per scan strategy. The four scanning strategies they studied are as follows. The first scan strategy was a continuous scan where the odd number layers are scanned parallel to the x-axis and the even number layered layers are scanned parallel to the y-axis. The second scan strategy was a continuous scan where the odd numbered layers are scanned at 45 degrees counter-clockwise about the x-axis and the even numbered layers

are scanned at 45 degrees clockwise about the x-axis. The third scan strategy was an island scan. Every island in the island scan was is 2.5 mm by 2.5 mm in size. The islands in the odd numbered layers alternate between being scanned parallel to the x-axis and parallel to the y-axis, and each island that was scanned parallel to the x-axis in the odd number layers was scanned parallel to the y-axis in the even layers and vice-versa. The final scan strategy was also an island scan strategy where every island is 2.5 mm by 2.5 mm in size. The islands in the odd numbered layers alternate between being scanned at 45 degrees counter-clockwise about the x-axis and 45 degrees clockwise about the x-axis, and each island that was scanned 45 degrees counter-clockwise about the x-axis in the odd number layers was scanned 45 degrees clockwise about the x-axis in the even layers and vice-versa. At the conclusion of their study, they found that the parts that were built with the island scan strategies had higher residual strains compared to the parts built with continuous scanning strategies, and the higher strains were especially apparent near the part's boundaries. They also provided two explanations to this: the island scanning creates additional mechanical constraints due to having fewer free surfaces for the material powder to expand, and the path generation software used for the simulation of the process creating mini-islands.

Denlinger *et al.* [9] studied the in situ residual stress behavior of a small block geometry printed using the L-PBF process. The study included developing a finite element model to simulate the block geometry being printed out of Inconel 718 using the L-PBF process and experimentally verifying that model using distortion and temperature in situ measurements shown in Ref. [56]. The block geometry used in Denlinger *et al.*'s [9] study: had base dimensions of 6.3 mm by 6.3, had a height of 2.3 mm, had a volume of 91 mm^3, and when the part was printed contained 38 layers. They found out the following from their study. First, high tensile stress levels that are usually above a materials yield strength are shown to exist in the most recently deposited layers and this forces the layers beneath the newly deposited layer to be in compression. For the their build, the top surface of the build plate as well as layers 1-20 of the final build are in compression, and the layers 21-38 of the final build are in tension. Second, for the layers below the last deposited layer the x component and y component of the residual stress are similar, and the explanation they provided was that this behavior of stress homogenization was due to the hatch rotation angle being 67 degrees. Third, in the longitudinal direction of the scan, the residual stress magnitude in the deposited material is at its maximum.

Shiomi *et al.* [53] studied the distribution of residual stress of L-PBF produced part made of mixture of SCM440, copper phosphate, and nickel, as well as discussing the reduction of residual stress using three different methods. The study portion of their work consisted of them measuring the stress during the L-PBF printing process using a strain gauge and developing a mathematical model to calculate residual stress. The three methods of stress reduction they discussed are heat treatment, re-scanning of laser, and heating of the powder bed. To demonstrate the effects of the heat treatment they placed the finished

part still attached to the base plate in muffle finance and heated it to three distinct temperatures: 500°C, 600°C, and 700°C for one hour without controlling the atmosphere. For the re-scanning of laser method, they used the same laser used in the forming process in order the heat up the top surface after the creation of each layer. For the heating of the powder bed method, they heated up the base plate 80°C, 120°C, and 160°C and then printed the part as normal. They drew the following conclusions from the study. First, the effect that scan speed has on average tensile stress is negligible. Second, the top of the model contained the largest value of tensile residual stress irrespective of the scan speed. Third, their heat treatment method showed that heating the part and base plate to a temperature to 600 °C and 700 °C reduced the residual tensile stress in the top layer by 70 percent. Fourth, their re-scanning of laser method showed that as the energy input for the laser during the re-scanning process increases the residual stress in the top layer decreases, and the when that energy input was set to 12.4 J/mm^2 the residual stress of the top layer was reduced by 55 percent. Fifth, when the build plate is heated to a temperature of 160 °C the residual stress of the top layer was reduced by 40 percent.

Zach and Branner [57] also studied the effects of scan strategy on residual stresses, by using the following method. They printed a build consisting of multiple T-bar parts made of 1.2709 tool steel. Each T-bar on that plate being built with one of the following scan strategies: x-scanning, y-scanning, xy alternating scanning, and island scanning. Then for each of the scanning strategies they measured, using neutron diffraction, the longitudinal (x-axis), normal (y-axis), and transverse (z-axis) residual stresses of the parts at twelve different points: eight point going along the top horizontal portion of the T-beam, and four points along center vertical portion of the T-beam. For the residual stress measurements made on the horizontal portion, they found that the x-scanning and the xy alternating scanning strategies created the most tensile residual stress with the x scanning strategy having the highest. However they found that the y-scanning and island scanning strategies produced lower residual stresses with the island strategy having the lowest. For the longitudinal residual stress measurements on the vertical portion, they made the following two observations. First, the x-scanning and the island scanning strategies exhibited the behavior of continuously increasing stress starting with the first layer. Second, for the y-scanning and alternate scanning strategies they found that the residual stress at the bottom layer had values between 220 MPa and 263 MPa and then between base and measuring point above it the stresses decreased, followed by an increase from thereon out. For the normal stresses measured from the vertical portion, they found that the trends of both the x-scanning and island scanning strategies followed similar trend compared to the longitudinal stresses. Additionally, the y-scanning strategy had continually decreasing stresses starting at the bottom, the order of scanning strategies based on residual stress is similar to the longitudinal stresses measured on the vertical portion, and the island scanning strategy had higher stress than the xy alternating scanning strategy at the top layer. For the transverse residual stresses on the vertical portion, they made the following three

observations. First, the y-scanning and the xy alternating scanning strategies had tensile stresses at the base while the x-scanning and the island scanning strategies had compressive stresses at the base. Second, the top layer was in tension regardless and scanning strategy. Third, the order of scanning strategies based on residual stress is similar to the longitudinal stresses measured on the vertical portion.

1.4: Distortion in the L-PBF Process

One of the most common negative effects of residual stress is part distortion. During the study of residual stresses in L-PBF parts distortion measurements are taken of the part either during or after the completion of the printing process in order to verify a finite element model used the simulate the L-PBF printing of said part [[58], [59]]. In Ref. [58], Dunbar et al used both ex situ and in situ measuring techniques to verify an FEA model of the L-PBF process. They printed two builds each with different build heights and different scanning strategies: rotating, and constant. In addition, both parts were made out Inconel 718. The in situ displacement measuring method they used was a displacement sensor attached to the build plate of the L-PBF machine, which measures the z-displacements with an accuracy of ± 15 μm, and the ex situ displacement measurements were taken using coordinate measuring machine (CMM). All in situ and ex situ displacement measurements they took was at four different areas on the part. The FEA model that they used was Project Pan Version 2.81 by Autodesk Inc. From their study they drew the following four conclusions. First, for any measurement location, they found that the max average percentage error of the distortion profile is 12% between the FEA model and the measured results. Second, their FEA software was able to calculate the distortion in the z-direction within 10 percent of the in situ measurements. Third, they found during the build process that the peak distortion is usually a several layers below the top layer, and the top layer's distortion is usually less that 30 percent peak distortion. Fourth, they found that after their builds reached a certain build height, the build height and the peak distortion value of the build become independent of one another.

In Ref [59], Yaghi *et al.* experimentally measured and numerically simulated (finite element method) the distortion and residual stress of an impeller made of stainless steel 316L. The impeller they studied was first made by 3D printing and then had 0.5 mm removed from a few surfaces of the impeller blades and hub. They found that the distortion measurements found using the GOM ATOS triple measurement system were found to be very close to the finite element (FE) method distortion results. Also, after the creation of the original impeller they designed a new "distortion-compensated" impeller using the data from the FE model, and when the peak distortions were measured they found the distortion were less than 50 percent of the peak distortion values of the original impeller.

Yaghi *et al.* [60] printed three impeller samples in an L-PBF machine each made out of different material: Ti64, Inconel 718, and AlSi10Mg. These samples were experimentally measured for distortion as well as residual stress. The printing of the samples were also numerically simulated using two different FE method techniques: inherent stain method and analytical temperature field method. They then compared the experimental and numerical results. They found that the distortion and stress values calculated from the analytical temperature field method and the elasto-plastic inherent stain method were decently accurate to the experimental results, however the elasto-plastic method's distortion-profile was the most accurate compared to the experimental values. In addition, they found that the elastic inherent strain method was the least accurate of the FE techniques studied due to the technique overestimating the peak stress values.

Yang *et al.* [61] printed a bridge structure built out of Inconel 718 on L-PBF machine in order to collect distortion data to compare to two finite element models: the line-heating model, and layer-heating model. They found that the layer-heating model took less time the line-heating model due to the fact that the line-heating model requires a much finer mesh than the other method; therefore, for analyzing larger parts, the line-heating model is unsuitable. They also noted that structural stiffness play a large role in the residual stress and deformation in an L-PBF build, and a sequentially coupled thermal model can be used to model the L-PBF process. They showed that the deformation profile of the top surface of the bridge structure from the two FE models matched to those experimentally measured; the deformation profile shown being a convex curve with the end curving up about 0.2 mm relative to the center of the bridge.

Papadakis *et al.* [62] printed a twin cantilever out of Inconel 718 using the L-PBF process in order to experimentally verify a commercial FE software package. Once printed they cut the supports of the substrate and measured the distortion by use of a perthometer which had a resolution of 0.1 mm. They showed that distortion profile of the cantilever was that it the both sides of the twin cantilever bent up in a convex fashion leading to vertical distortion of 0.8 mm, relative to the center, on the ends. The vertical distortion values from the FE modeling method they used had about a 26 percent error compared when compared to the measured results; they cited the cause to be from the simplifications made in the FE modeling. They completed a parameter study on the twin cantilever builds in which they varied the thickness of the cantilever. They found that the minimum distortion values occurs with the thickness of the part is set to 550 microns, with the distortion increasing as the thickness is increased or decreased from that value. Also, they found at thickness above 910 microns the vertical distortion does not change even with increasing heat input, and this is due to there being enough stiffness in the part at those thicknesses that the stiffness does not allow any additional vertical distortion.

1.5: Research Goals and Motivation

The objective of this work is to demonstrate and validate the used of simulation tools in order to find the optimal orientation of additive manufactured parts. The optimal orientation is determined by the following criteria: displacement, stress levels, and printability. Displacement being how much the part distorts form the ideal or theoretical geometry. Stress level being mainly due to residual stress. Printability describes how likely the part is going to complete the process of being additively manufactured without failure. An orientation that minimizes distortion and stress as well as maximizes printability would be the most optimal. The reason for the use of simulation software is to eliminate the need to print multiple in a train-and-error fashion in order to determine the optimum build. This in turn will reduce the number of build failures, reduce the amount of material scrapped, reduce the cost of production associated with the builds, and improve the quality control of the additive manufactured process.

CHAPTER 2 :
RESEARCH METHODOLOGY

2.1: Overview

In order to complete the objectives of this work, the following methodology was used. First, the two test builds were designed, printed, and simulated. Second, a part with a more complex geometry was simulated in various orientations. Third, three of the simulated complex part orientations were printed. Fourth, measurements were taken of the printed builds while still on the build plate. Fifth, all of the printed builds had their build plates (substrates) removed. Sixth, measurements were taken of the printed builds after substrate removal. Seventh, the simulation and measured data were used to determine the best orientation to print the complex geometry. Detailed descriptions of each of the aforementioned steps are discussed below.

2.1.1: Test Build #1

The first of test build is shown in Figure 1 below. The build contained 24 thin flat plates with dimensions of 50 x 10 x 2 mm (length x width x height). The build's supports consisted 50 x 10 x 10 mm placed underneath the thin plates with four different hole-geometries as seen in Figure 2. The hole-geometries are described in Table 2 below. In addition, for support styles one through three, there is 10 x 10 mm portion that contains no holes, and this along with the flat plates is used to replicate a cantilever-beam-like structure. The exact positions of the parts on the build relative to the center are shown in Table 3. In Table 3, the Z rotation angle is positive in the counter-clockwise direction, and its zero is along the horizontal (x-axis) with the 10 x 10 mm non-holed portion being on the left side. The material chosen for both the thin plates and the supports for this build was AlSi10Mg, and both the plates and supports for this test build were generated in SolidWorks software package.

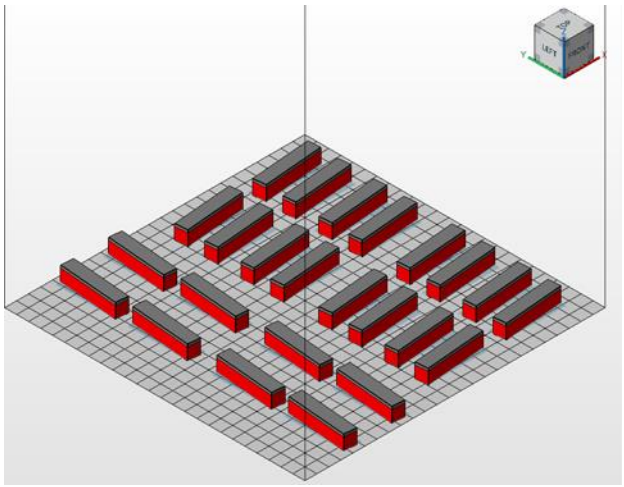

Figure 1: Test Build #1 full layout (isometric view)

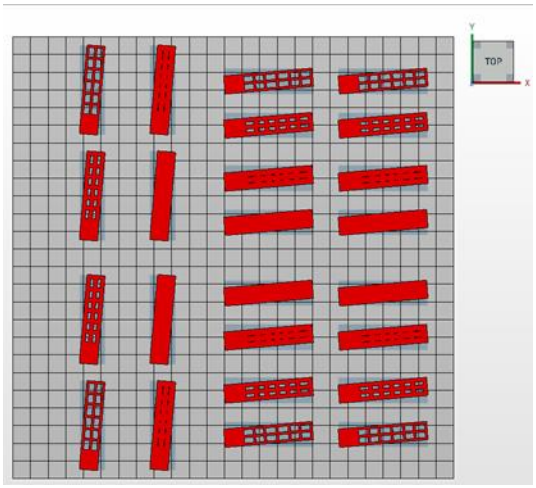

Figure 2: Test Build #1 support layout (top view)

Table 2: Support style descriptions for Test Build #1

Support Style #	Description
1	5x2 grid of 1 mm holes
2	5x2 grid of 2 mm holes
3	5x2 grid of 3 mm holes
4	No holes

Table 3: Part with support placement relative to center of build plate for Test Build #1

Support Style #	X (mm)	Y (mm)	Z Rotation Angle (deg)
1	85	100	5
2	85	75	5
3	85	45	5
4	85	20	5
4	85	-20	5
3	85	-45	5
2	85	-75	5
1	85	-100	5
1	-80	95	85
2	-80	35	85
3	-40	95	85
4	-40	35	85
1	-80	-95	85
2	-80	-35	85
3	-40	-95	85
4	-40	-35	85
1	20	100	5
2	20	75	5
3	20	45	5
4	20	20	5
1	20	-100	5
2	20	-75	5
3	20	-45	5
4	20	-20	5

2.1.2: Test Build #2

The second test build is shown in Figure 3 below. The build contains 16 cantilever beams with 2 different heights; the beams on the lower half on the build plate have dimensions of 102 x 14 x 24 mm and the beams on the upper half of the build plate have dimensions of 102 x 14 x 22 mm (see Figure 4). All the supports used in this build an array of 2 x 2 x10 mm pillars that were spaced 2 mm apart from each other along the x and y axis and filled up the space underneath the lever portion of the cantilever. The layout of the pillars within the support is further shown in Figure 5. The coordinates for the positions of the cantilevers relative to the center of the build plate in displayed in Table 4, and in Table 4 the 2 mm and 4 mm part styles represent the two different heights parts with 2 mm meaning the 22 mm height and 4mm meaning the 24 mm height. The material chosen for

both the thin plates and the supports for this build was AlSi10Mg, and both the cantilevers and supports for this test build were generated in SolidWorks software package.

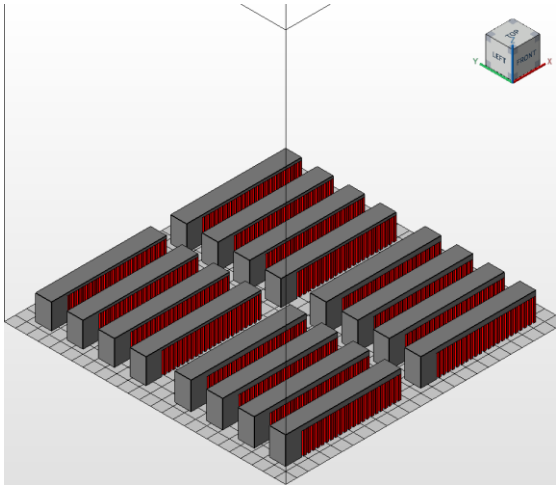

Figure 3: Test Part #2 full layout (isometric view)

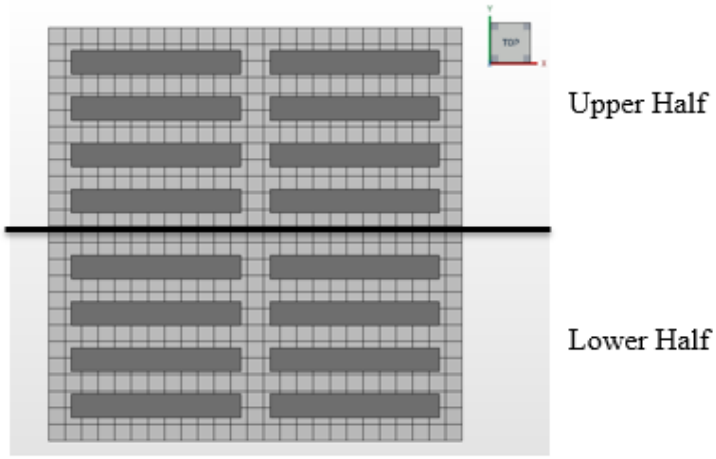

Figure 4: Test Build #2 (top view)

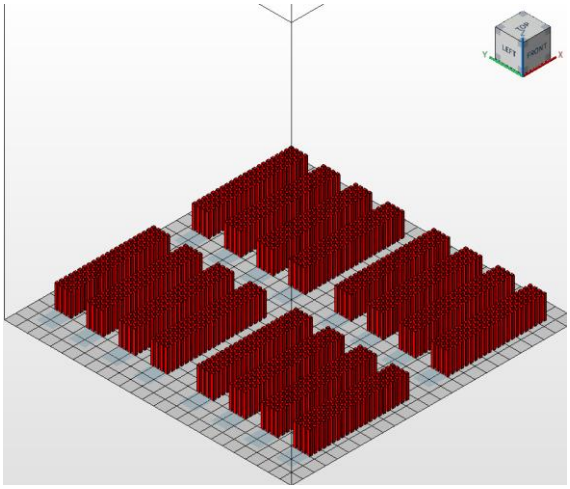

Figure 5: Test Build #2 support layout (isometric view)

Table 4: Part with support placement relative to center of build plate for Test Build #2

Part Style	Part X (mm)	Part Y (mm)	Support X (mm)	Support Y (mm)	Z Rotation Angle (deg)
2 mm	60	104	68	104	0
2 mm	60	76	68	76	0
2 mm	60	48	68	48	0
2 mm	60	20	68	20	0
4 mm	60	-20	68	-20	0
4 mm	60	-48	68	-48	0
4 mm	60	-76	68	-76	0
4 mm	60	-104	68	-104	0
2 mm	-60	104	-52	104	0
2 mm	-60	76	-52	76	0
2 mm	-60	48	-52	48	0
2 mm	-60	20	-52	20	0
4 mm	-60	-20	-52	-20	0
4 mm	-60	-48	-52	-48	0
4 mm	-60	-76	-52	-76	0
4 mm	-60	-104	-52	-104	0

2.1.3: Printing of Both Test Builds

The printing of the first test build was done on the EOS M 290 metal printer with the chosen materials for the parts and supports, an aluminum alloy (not AlSi10Mg), and the process parameters outlined in Table 5 below. The first test build after being printing is shown in Figure 6 below. The printing of the second test build was done on the #D Systems ProX DMP 320 metal printer with the chosen materials for the parts and supports,

an aluminum alloy (not AlSi10Mg), and the process parameters outlined in Table 5. The result of printing the second test build is shown in Figure 7 below. The numbers embossed on the cantilevers as shown in Figure 7 are for identification purposes are were not on the original part file. The purpose for the two test builds was to assist in the verification of the simulations. The choice of a cantilever design for the test build due it being simple geometry and have a known deformation profile. The known deformation profile allowed for the visual inspection of the deformed model produced by the simulation to determine how realistic the deformed model was.

Table 5: Printing process parameters

Parameter	Value
Laser Power	370 W
Heat Source Absorption Efficiency	20%
Laser Beam Diameter	0.08 mm
Travel Speed	1400 mm/s
Layer Thickness	60 μm
Hatch Spacing	110 μm
Recoater Time	10 sec
Interlayer Rotation Angle	115 deg

Figure 6: Test Build #1 post-print still on substrate

Figure 7: Test Build #2 post-print still on substrate

2.1.4: "Bracket" Builds

The complex part that was selected for this work was a part that was called the "Bracket", and the "Bracket" is shown in Figure 8 and Figure 9 below. The "bracket" was generated in SolidWorks. In addition, the "Bracket" was elevated 6.34mm (about 0.25 in) above the build plate. The supports for this part (the blue structures in Figure 8 and Figure 9) were generated in the Netfabb Ultimate software package using there SLM support script. The support script calls for area with volume support this means that supports critical areas with supports that fill up the space between the critical area and the build plate. The orientations that were chosen to be simulated are as follows: Counter-clockwise rotations about the x-axis in 30-degree increments from 0 to 330 degrees while having no rotations about the y and z axis, and counter-clockwise rotations about the y-axis in 30-degree increments from 0 to 330 degrees while having no rotations about the x and z axis. In addition, the orientations of the "Bracket" are labeled with an XmYn notation where m is the counter-clockwise rotation in degrees about the x-axis and where n is the counter-clockwise rotation in degrees about the y-axis; in Figure 8 and Figure 9, the orientation of the "Bracket" that is shown is X0Y0. For each orientation of the "Bracket" that was simulated, the part was placed at the center of the build plate. The material chosen for the "Bracket" and the supports was AlSi10Mg. The purpose of the "Bracket" is to demonstrate the use of the software in finding the optimum orientation.

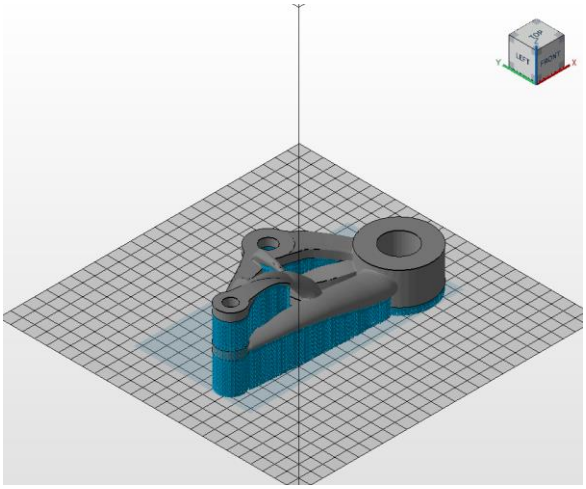

Figure 8: "Bracket" (font isometric View)

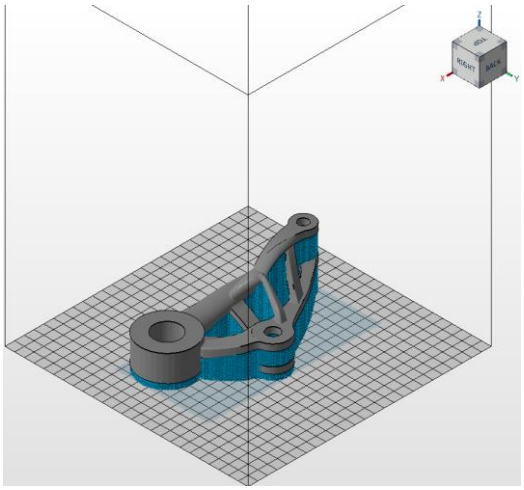

Figure 9: "Bracket" (rear isometric View)

2.1.5: Printing of the "Bracket" Builds

The "Bracket" orientations that were printed were X0Y0, X60Y0, and X0Y90. The printing of the chosen "Bracket" orientations were done with the EOS M 290 metal 3D printer, the chosen materials for the parts and supports, an aluminum alloy (not AlSI10Mg) for the build plate, and the process parameters outlined in Table 5. The resulting prints for the three "Bracket" orientations are shown in Figure 10, Figure 11, and Figure 12 below. Similar to the two test builds, the purpose of printing the three "Bracket" orientations was to assist in the verification of the simulations.

Figure 10: X0Y0 “Bracket” orientation build post-print still on substrate

Figure 11: X60Y0 “Bracket” orientation build post-print still on substrate

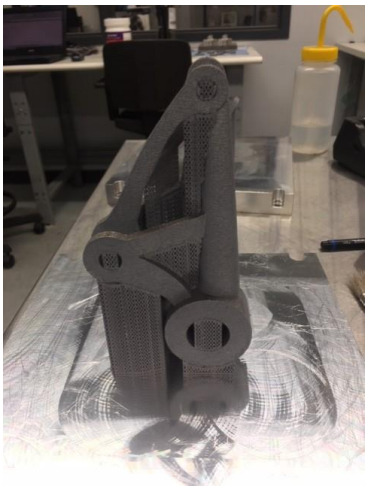

Figure 12: X0Y90 “Bracket” orientation build post-print still on substrate

2.2: Simulation Methodology

The following procedure was used in order to complete the required simulations for this work. First, the parts were imported into the Netfabb Ultimate software package. Second, the parts were placed and organized in the Netfabb Ultimate software package (see Section 2.1.1, 2.1.2, and 2.1.4). Third, supports were generated in Netfabb Ultimate software package if a part did not already have supports that were already imported (see Section 2.1.1, 2.1.2, and 2.1.4). Fourth, the builds were exported into Netfabb's Simulation Utility as a 3D Manufacturing Format (3mf) file to be simulated. Fifth, the desired simulations of the builds were set up in the Simulation Utility. Sixth, the simulations were running in the Simulation Utility. Seventh, points of interest (POIs) on each build were selected and mapped using Netfabb Ultimate software package. Eighth, the data was recorded and analyzed in Microsoft Excel. Detailed descriptions of each of the aforementioned steps are discussed below.

2.2.1: Netfabb Simulation Theory

As stated previously Netfabb Simulation software is used for all the simulations in this work. The goal of this section is describe the FE method that Netfabb uses in order to do its simulations, and the information presented in this section comes from Ref. [63]. In short, Netfabb is non-linear decoupled 3D transient FE solver which is used to thermo-mechanically model either a DED or an L-PBF 3D printing process. In a decoupled model the thermal behavior affects the mechanical behavior, but also assumes that the relationship does not work the other way around. The non-liner aspect of Netfabb's FE model stems from the weak formation which is derived from the governing mechanical and thermal equations by the use of the Galerkin approach. The thermal governing equation being energy balance, and the mechanical governing equation being stress equilibrium. The nodal solution vectors for both temperature and displacement is then derived from the aforementioned weak formulation. The nodal solution vectors are solved from by an iterative application Newton-Raphson method as shown in Equation (2-1) where $\boldsymbol{U}_{i+1}$ is the nodal solution vector of either temperatures or displacements of the current iteration, $\boldsymbol{U}_i$ is the nodal solution vector of either temperatures or displacements of the previous iteration, $\boldsymbol{R}_i$ is the residual vector for the previous iteration, and $\frac{d\boldsymbol{R}_i}{d\boldsymbol{U}}$ being the stiffness matrix for the previous iteration.

$$\boldsymbol{U}_{i+1} = \boldsymbol{U}_i - \left[\frac{d\boldsymbol{R}_i}{d\boldsymbol{U}}\right]^{-1} \boldsymbol{R}_i \tag{2-1}$$

For a given time step, the iterations start with an initial guess of $\boldsymbol{U}_0$ which is either a chosen value of the solution from the previous time step, and the iterations continue until an specific norm of the vector $\boldsymbol{R}$ is less than a specified threshold.

The thermal portion of model used in the software starts with the thermal equilibrium equation with conditions of constant density ρ and an isotropic heat capacity C_p as shown in Equation (2-2) below where T is temperature, t is time, $\nabla \cdot$ is divergence, $\boldsymbol{q}$ is the heat flux, $\boldsymbol{r}$ is the relative reference temperature, and Q is the body heat source. Fourier conduction equation is used in the model to describe the distribution of heat within the part as shown in Equation (2-3) where the scalar k is the isotropic temperature dependent thermal conductivity, and ∇ is the gradient.

$$\rho C_p \frac{dT}{dt} = -\nabla \cdot \boldsymbol{q}(\boldsymbol{r}, t) + Q(\boldsymbol{r}, t) \quad \textbf{(2-2)}$$

$$\boldsymbol{q} = -k\nabla T \quad \textbf{(2-3)}$$

To solve Equations (2-2) and (2-3), initial conditions, heat input model, and boundary conditions need to be applied. The applied initial condition is $T_0 = T_\infty$ were T_∞ is either the ambient temperature or the preheat temperature of the build plate. There are two heat input models that can be applied: surface heat flux or a volumetric heat source model with the chosen heat flux model being 2D Gaussian ellipsoidal distribution shown in Equation (2-4), and the chosen volumetric heat source model being the Goldak's 3D Gaussian ellipsoidal distribution shown in Equation (2-5). In the Equations (2-4) and (2-5), P is the heat source power in [W], η is the heat source efficiency, a is the width in the of the ellipsoid in the x-direction in [m], c is the length of the ellipsoid in the z-direction in [m], b is the depth of the ellipsoid in the y-direction in [m], v_s is the speed of the heat source [m/s], t is time [sec], and S_q is the surface where the heat flux is applied. In addition, the axis for Equations (2-4) and (2-5) are as follows: the x-direction is normal the direction of the heat source and parallel to the surface S_q, the y-direction is normal to the surface S_q, and the z-direction is parallel to both the direction of the heat source and the surface S_q.

$$q_{surface} = \frac{3P\eta}{\pi ac} \exp\left(-\frac{3x^2}{a^2} - \frac{3(z + v_s t)^2}{c^2}\right) \quad \textbf{(2-4)}$$

$$Q_{volume} = \frac{6\sqrt{3}P\eta}{abc\pi\sqrt{\pi}} \exp\left(-\frac{3x^2}{a^2} - \frac{3y^2}{b^2} - \frac{3(z + v_s)^2}{c^2}\right) \quad \textbf{(2-5)}$$

The thermal boundary condition that is applied to the boundaries of the part in the thermal model is Newton's Law of cooling as shown in Equation (2-6) where q_{conv} is the convective heat flux, h is the heat transfer coefficient, and T_s it the surface temperature at the boundary. The heat transfer coefficient used in Equation (2-6) is a single effective heat transfer coefficient which was the result of combining the effects of convection and radiation, and this coefficient is calculated from Equation (2-7) where h_{free} is the heat transfer coefficient due to natural or free convection, h_{forced} is the heat transfer coefficient due to forced convection, and h_{rad} is the heat transfer coefficient due to radiation.

	$q_{conv} = h(T_s - T_\infty)$	**(2-6)**

	$h = h_{free} + h_{forced} + h_{rad}$	**(2-7)**

In Equation (2-7) the two convection heat transfer coefficients (h_{free}, h_{forced}) can be found using empirical or analytical methods with reasonable values being between 5 to 15 W/(m^2°C) for free convection, and 5 to 20 W/(m^2°C) for forced convection in the case of L-PBF. However, the value for h_{rad} is calculated using Equation (2-8) where ε_{rad} is the surface emissivity and σ_{SB} is the Stefan-Boltzmann constant which has a value of 5.67 x 10-8 W/(m^{2}K^4). Equation (2-8) is derived from the Stefan-Boltzmann law shown in Equation (2-9).

	$h_{rad} = \varepsilon_{rad}\sigma_{SB}(T_s + T_\infty)(T_s^2 + T_\infty^2)$	**(2-8)**

	$q_{rad} = \varepsilon_{rad}\sigma_{SB}(T_s^4 - T_\infty^4)$	**(2-9)**

The mechanical side of the model used by Netfabb starts with the thermal history provided by the thermal model and stress equilibrium equation shown in Equation (2-10) where the vector $\boldsymbol{\sigma}$ is the stress. To solve the stress equilibrium equation an equation the relates stress, strain, and the material properties, and this was accomplished using the mechanical constitutive law shown in Equation (2-11) where $\boldsymbol{C}$ is the fourth order material stiffness tensor and $\boldsymbol{\varepsilon}_e$ is the elastic strain.

	$\nabla \cdot \boldsymbol{\sigma} = 0$	**(2-10)**

	$\boldsymbol{\sigma} = \boldsymbol{C}\boldsymbol{\varepsilon}_e$	(2-11)

From here the model can go down two different paths base on either using small deformation theory or large deformation theory, and since large deformation theory was not used in this work it will be omitted from the mechanical model discussion. For small deformation theory, Equation (2-12) can be used calculate the total strain at a given node. In Equation (2-12), $\boldsymbol{\varepsilon}$ is the total strain, $\boldsymbol{\varepsilon}_p$ is the plastic strain, and $\boldsymbol{\varepsilon}_T$ is the thermal strain.

	$\boldsymbol{\varepsilon} = \boldsymbol{\varepsilon}_e + \boldsymbol{\varepsilon}_p + \boldsymbol{\varepsilon}_T$	(2-12)

Equations (2-13) through (2-15) are used in the calculation of thermal strain ($\boldsymbol{\varepsilon}_T$), and in those equations $\boldsymbol{\alpha}$ is a thermal expansion coefficient matrix, and T_{ref} is the reference temperature.

	$\boldsymbol{\varepsilon}_T = \boldsymbol{\varepsilon}_T \boldsymbol{j}$	(2-13)

	$\boldsymbol{\varepsilon}_T = \boldsymbol{\alpha}\left(T - T_{ref}\right)$	(2-14)

	$\boldsymbol{j} = [1\ \ 1\ \ 1\ \ 0\ \ 0\ \ 0]^T$	(2-15)

As for the plastic strain ($\boldsymbol{\varepsilon}_p$), it is calculated by Equations (2-16) through (2-18) which are derived from the Von Mises yield criterion and the Prandtl-Reuss flow rule. In Equations (2-16) through (2-18) f_Y is the yield function, σ_{vm} is the Von Mises stress, σ_Y is the yield stress, $\boldsymbol{\varepsilon}_q$ is the equivalent plastic strain, and $\boldsymbol{\alpha}_{flow}$ is the flow vector.

	$f_Y = \sigma_{vm} - \sigma_Y\left(\boldsymbol{\varepsilon}_q, T\right) \leq 0$	(2-16)

	$\dot{\boldsymbol{\varepsilon}_p} = \dot{\boldsymbol{\varepsilon}_q}\boldsymbol{a}_{flow}$	(2-17)

	$\boldsymbol{a} = \left(\frac{\partial f_y}{\partial \boldsymbol{\sigma}}\right)^T$	(2-18)

2.2.2: Importing the Part Files

The parts were imported as Standard Tessellation Language (STL) file. For the parts and supports that were created in SoildWorks, they had to be converted for a SolidWorks Part (SLDPRT) file to an STL file; this conversion was performed in the SolidWorks the fine preset, as shown in Figure 13 below. The fine preset is one of three presets used to control the resolution of exported STL file, and the resolution settings have two major parameters Deviation and Angle Tolerances (see Figure 13). In addition, the aforementioned two parameters set by the coarse and fine presents vary based on the part that is being converted. Note that there two different types of STL files available for use: Binary and ASCII; ASCII STL files provide greater detail but are larger in file size while Binary STL files are simpler in detail and are smaller in file size. For the entirety of this work, Binary STL files used. A summary of the imported STL files for each build can be seen in Table 6 below. For the construction of the first test build, all the supports were imported and placed first followed by the thin plates. For the construction of the second test build, the parts the opposite took place where the cantilevers were imported and placed first followed by the supports.

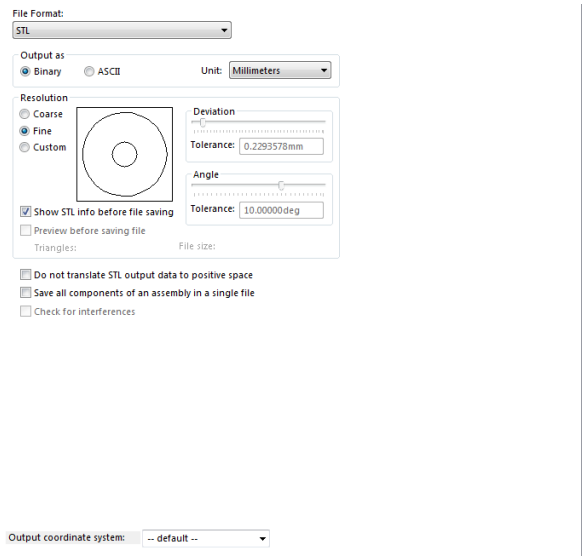

Figure 13: STL export settings for SolidWorks

Table 6: Imported STL file summary for simulated builds

Build	Total # of STL Files	Total # of Part STL Files	Total # of Support STL Files
Test Build #1	48	24 (24 duplicates of a single part)	24 (6 of each support style)
Test Build #2	32	16 (8 duplicates of each cantilever height)	16 (16 duplicates of the same support structure)
"Bracket" (per Orientation)	1	1	0 (Support was generated within Netfabb)

2.2.3: Setup: Overview & Process Parameters Settings

For the setup, the settings that needed to be set were split up into six categories: process parameters, machine, build plate, operating conditions, heat treatment, and solver settings. The process parameters can either be ones that are premade in the software or user created custom ones, and for the custom process parameters, the software must first perform a set of calculations before the custom process parameters are ready for use in the software. The options for a new set of custom process parameters are shown in Figure 14, Figure 15, and Figure 16. The custom process parameters used for the simulations in this work are outlined in Table 7 below. The default settings were used for any setting that is exists in Figure 14, Figure 15, and Figure 16 but is not listed in Table 7, and the existence of the parameters “Lack of Fusion Temperature”, “Hot spot Temperature”, and “Interlayer Temperatures” in Table 7 infer that option of “Hot spots and lack of fusion” in Figure 15 was checked.

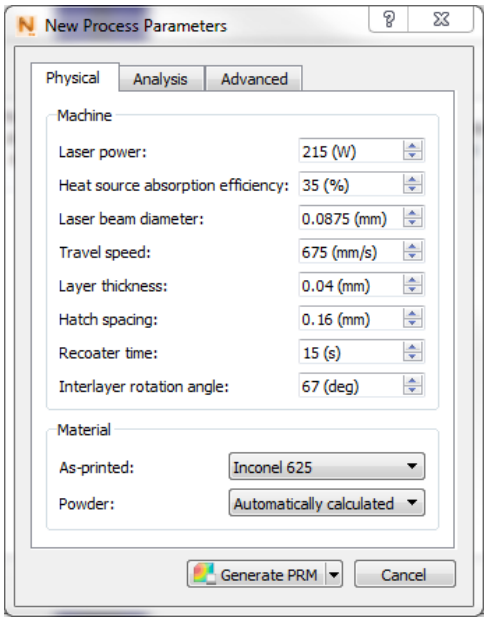

Figure 14: New custom process parameters (physical settings)

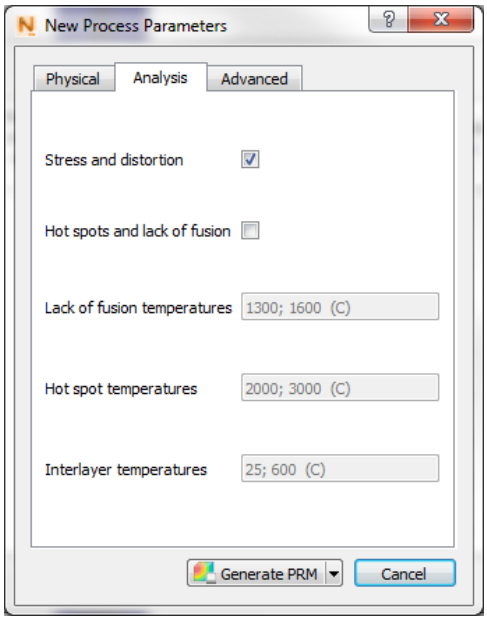

Figure 15: New custom process parameters (analysis settings)

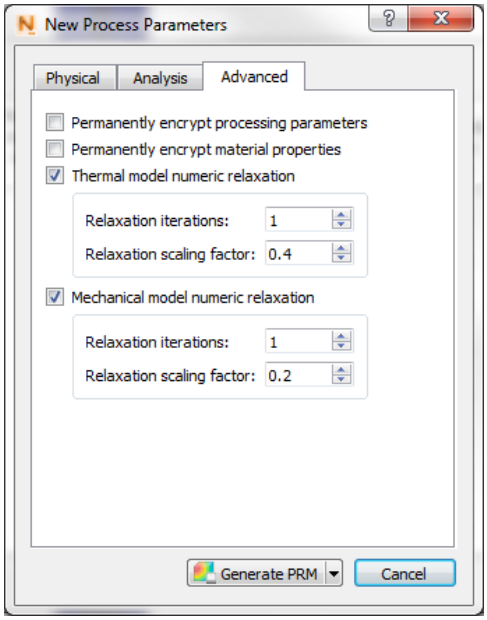

Figure 16: New custom process parameters (advanced settings)

Table 7: Simulation process parameters

Parameter	Value
Material	AlSi10Mg
Laser Power	270 W
Heat Source Absorption Efficiency	20%
Laser Beam Diameter	0.08 mm
Travel Speed	1400 mm/s
Layer Thickness	30 µm
Hatch Spacing	105 µm
Recoater Time	10 sec
Interlayer Rotation Angle	115 deg
Lack of Fusion Temperature	580 °C
Hot Spot Temperatures	880 °C
Interlayer Temperatures	25; 290 °C

2.2.4: Setup: Machine Settings

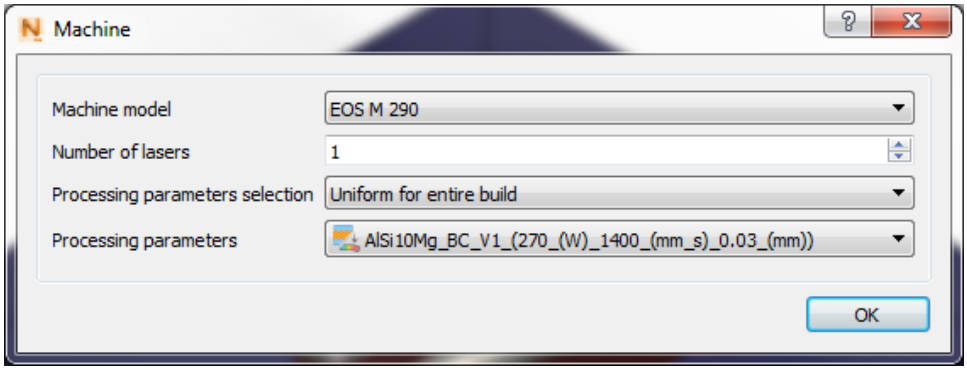

Figure 17: Simulation machine settings

The machine settings for all the simulations in this work are outlined in Figure 17 above. Note that the machine model setting in Figure 17, only contains reported data for the number of lasers and the build plate size, which can be ignored by the user if necessary. Which is why it was ok for the second cantilever build was simulated with these parameters even though it was printed on a different machine.

2.2.5: Setup: Build Plate Settings

The build plate settings for all the simulations are shown in Figure 18 and Figure 19 below. The build pate in the simulation was set to use the same material as the part as shown by the "Match part deposition material" option being checked in Figure 18. The settings for the operating conditions used for all the simulations are shown in Figure 20 below.

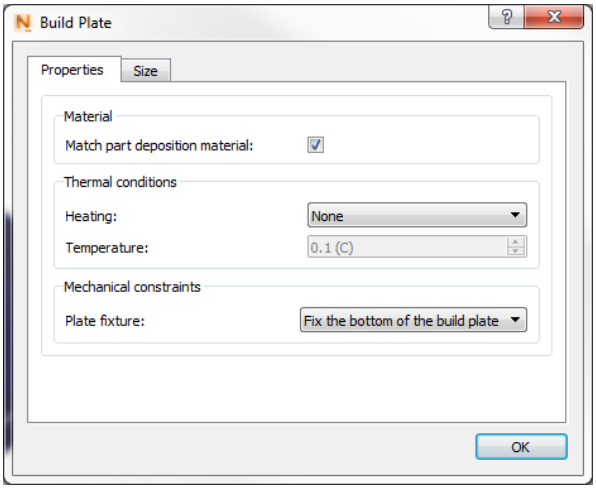

Figure 18: Simulation build plate properties

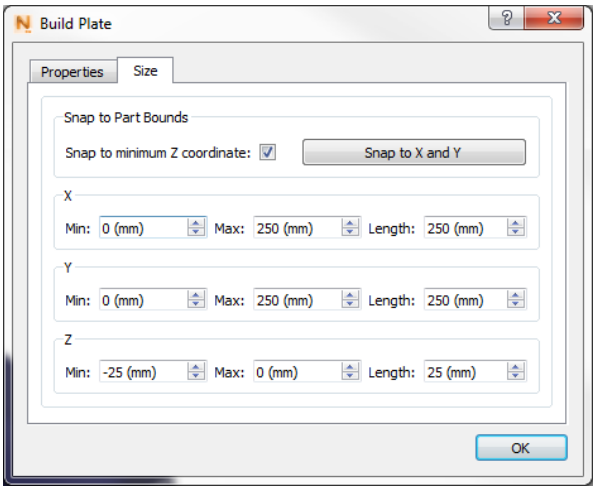

Figure 19: Simulation build plate size settings

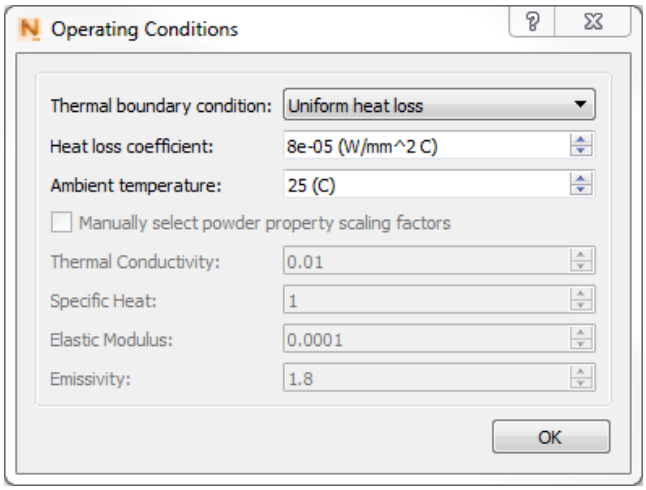

Figure 20: Simulation operating conditions

2.2.6: Setup: Stress Relief (Heat Treatment) Settings

The heat treatment settings are used for simulating a stress relief that occurs after a printing has been completed, and the information that can be entered is shown in Figure 21 below. Note that these settings can only be set if the "Simulate heat treatment" option is checked, and that the "Build plate annealing temperature" option is only available if the build plate material is different that the part deposition material (see Figure 18). The inputs for the stress relief schedule (Heat treatment process) (see Figure 21) are list of set points that basically sets a "virtual furnace" to specified temperatures at specified times with temperatures in between two set points ramping up at a constant linear rate. The material annealing temperature is best described as the temperature in which stresses are relieved for a given build. This parameter must be found by trial and error because it must be set based on how hot the builds gets, not how high the maximum temperature of the stress relief is set to. For most of the simulations in this work, a stress relief was not required and thus the heat treatment settings for those simulations are the same as Figure 21. However, for the simulations that did require a stress relief, those settings can be found in Figure 22 and Figure 23. As can be seen in Figure 22, the "virtual furnace" is set to 25°C or the ambient temperature (see Figure 20) which is lower than the set material annealing temperature. The purpose of this "fake heat treatment" (FHT) is described in detail in Section 2.2.13. The other set of heat treatment settings shown in Figure 23 was used only on the X0Y0 "Bracket" orientation build, and the settings were based on Condition SR1 from the ASTM F3318-18 standard. This standard states the annealing for the part requires that the temperature of 285°C (±14°C) be held within 120 minutes (±15 minutes), that the part then be cooled at rate equivalent to that of air cooling or faster, and the remainder of the annealing process be done in accordance with AMS 2771. [[64], [65]]. The real heat treatment (Figure 23) differs from the standard in that it simulates the build being cooled in the furnace for 24 hours instead of being air-cooled.

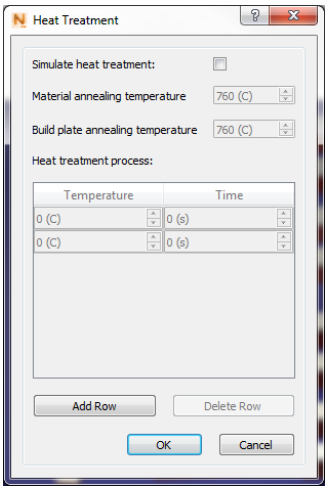

Figure 21: Heat treatment settings example (no stress relief scenario)

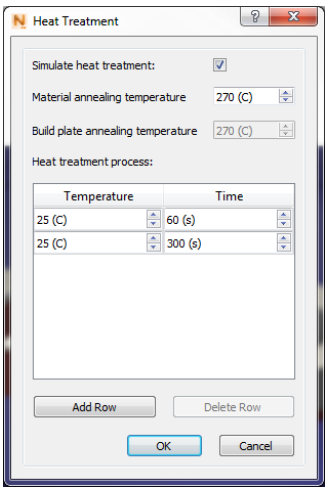

Figure 22: FHT settings

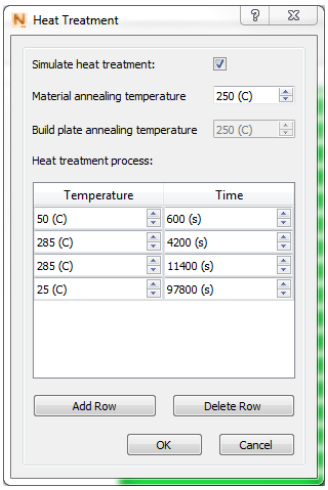

Figure 23: Real heat treatment settings (X0Y0 "Bracket" orientation simulation only)

2.2.7: Setup: Solver Settings

The solver settings used across all the simulations is shown in Figure 24 and Figure 25 below. The structural plasticity option (see Figure 25) inserts an additional time step called the plasticity time step (PTS) into the simulation. The PTS is inserted after the completion of the build and is where all the effects of plasticity on the model are calculated. The software has specific parameters that deal with plasticity for a given material: yield strength and ultimate tensile strength (UTS), and for the material used in the simulation (see Figure 17), and the plasticity information as a function of temperature is shown in Figure 26. In the plasticity data, the stresses that correspond to a plastic stain 0 are the yield strengths and the stresses that correspond to a plastic stain of 0.05 are the UTSs. Note that the options for displaying the "plastic strain" and the "equivalent plastic strain" become unavailable if plasticity is disabled (see Figure 25). The recoater tolerance setting in the

analysis settings (see Figure 24) sets the minimum amount of recoater clearance that is allowed. On a related note, if the "stop if recoater interference detected" setting (see Figure 24) is checked, the simulation will stop if the recoater clearance drops below the set amount. In addition, if the setting is not checked then after a given simulation the software will alert you if the recoater clearance dropped below the set amount during the simulation by reporting what the recoater clearance was at its minimum and at which layer. Recoater clearance is defined as the percentage of layer thickness the recoater is above the previous layer during the printing of a given current layer.

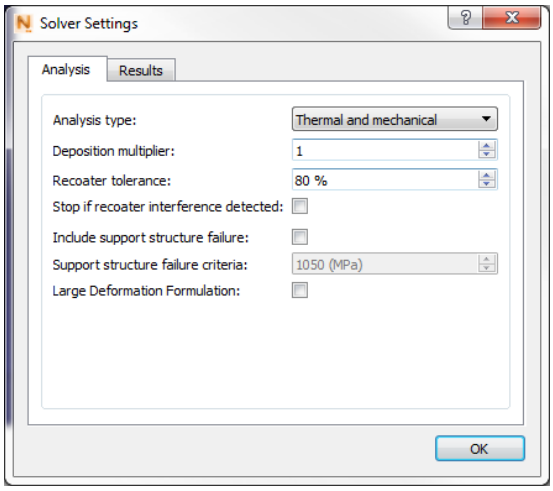

Figure 24: Simulation solver settings for the analysis

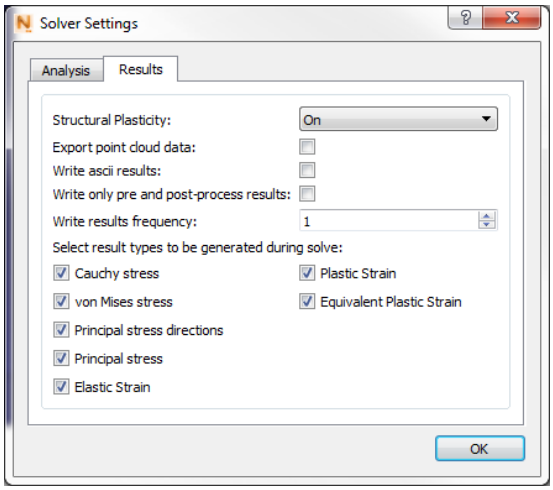

Figure 25: Simulation solver settings for the results

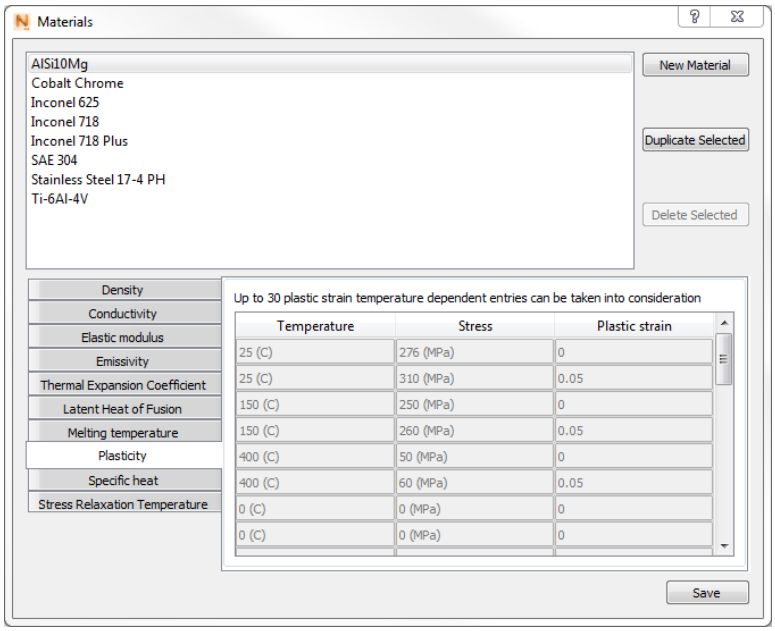

Figure 26: Netfabb plasticity properties for AlSi10Mg

2.2.8: First Run of the Simulations

The simulations started with running only the following builds: Test Build #1, Test Build #2, and X0Y0 "Bracket" Orientation Build. The first run of each of the aforementioned simulations in the work was done mesh setting shown in Figure 27 through Figure 29 below; the mesh settings used for Test Build #1 is shown in Figure 27, Test Build #2 is Figure 28, and the X0Y0 "Bracket" Orientation Build in Figure 29. As a side note, the meshing used in the Simulation Utility offers two different meshing approaches "Wall Thickness" and "Layer Based" each that offer different options on what setting is chosen. However, there are two options that apply to either meshing approach: "Padding Tolerance" and "Max Adaptivity levels". The "Padding Tolerance" options sets the distance in which the STL files are expanded in all directions, while the "Max Adaptivity levels" option set the maximum number of times a mesh can be coarsened for a given simulation it can have a value of zero through six. Mesh coarsening works by reducing the numbers of elements in a mesh the closer you get to the build plate in sections. The meshes that the Simulation Utility creates uses cube elements that are aligned with the software's global coordinate system, and the software applies a mesh to the build plate. Other than the settings presented in Figure 27, Figure 28, and Figure 29, another factor that effects meshing is thermal boundary condition that is set (see Figure 20). In Netfabb's Simulation Utility, there are two options for the thermal boundary condition: "Uniform heat loss" and "Conduction to loose powder". The "Uniform heat loss" condition applies a heat transfer coefficient to all the surface elements of a given mesh, and the STL is meshed as is; however, the "Conduction to loose powder" condition applies a box-like mesh that covers the entire exterior build volume of the build.

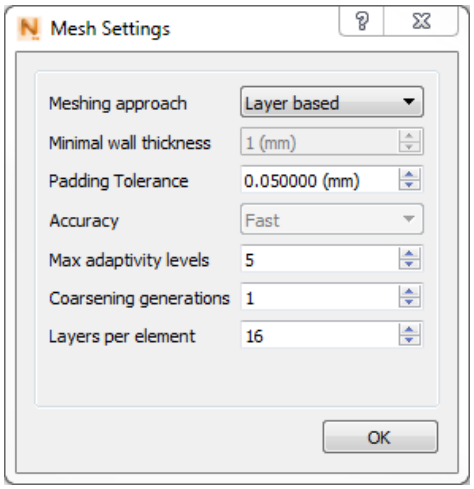

Figure 27: The settings for the first mesh of Test Build #1

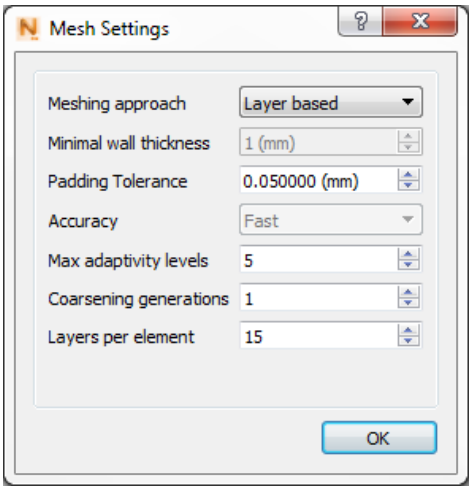

Figure 28: The settings for the first mesh for Test Build #2

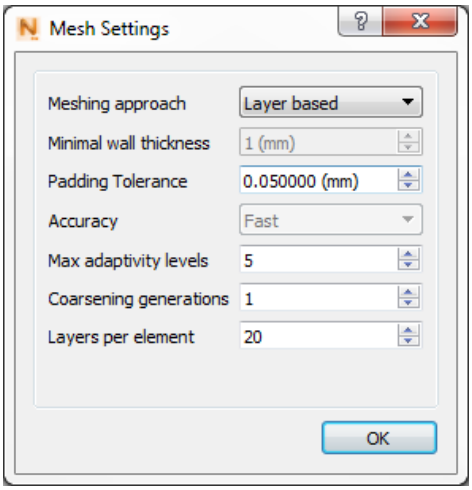

Figure 29: The settings for the first mesh for X0Y0 "Bracket" orientation build

2.2.9: Grid Convergence Study

At the conclusion of the initial simulations of Test Build #1, Test Build #2, and X0Y0 "Bracket" Orientation Build simulations, a grid convergence study was performed on each of the simulations, and the procedure use is as follows. First, a point was selected on the part at the final time step of the simulation. Second, one the following displacement results were selected for comparison: x-displacement, y-displacement, or z-displacement. Third, the value for that chosen displacement result was collected at the selected point. Fourth, the mesh settings were adjusted to produce a finer mesh. Fifth, the simulations were run again, and the displacement value was collected with the new mesh. Sixth, the displacement values for the new mesh were compared using the previous mesh. The displacement values were compared by calculating a percentage difference as shown in Equations (2-19), (2-20), and (2-21) below depending on which of the displacement results was chosen. In equation (2-19) : $\Delta_{\%,x}$ was the percentage difference for the x-displacement, $\delta_{x,i}$ was the x-displacement for the new mesh in mm, and $\delta_{x,i-1}$ was the x-displacement for the previous mesh in mm. In equation (2-20): $\Delta_{\%,y}$ was the percentage difference for the y-displacement, $\delta_{y,i}$ was the y-displacement for the new mesh in mm, and $\delta_{y,i-1}$ was the y-displacement for the previous mesh in mm. In equation (2-21): $\Delta_{\%,z}$ was the percentage difference for the z-displacement, $\delta_{z,i}$ was the z-displacement for the new mesh in mm, and $\delta_{z,i-1}$ was the z-displacement for the previous mesh in mm. Seventh, the fourth through sixth steps were repeated until the percentage difference between the new, and the previous mesh was very small.

$$\Delta_{\%,\mathrm{x}} = 100\left(\frac{\delta_{x,i} - \delta_{x,i-1}}{\delta_{x,i-1}}\right) \quad \textbf{(2-19)}$$

$$\Delta_{\%,\mathrm{y}} = 100\left(\frac{\delta_{y,i} - \delta_{y,i-1}}{\delta_{y,i-1}}\right) \quad \textbf{(2-20)}$$

$$\Delta_{\%,z} = 100\left(\frac{\delta_{z,i} - \delta_{z,i-1}}{\delta_{z,i-1}}\right) \quad \textbf{(2-21)}$$

The results of the grid convergence study are shown in Table 8 and Table 9 for the first test build, Table 10 and Table 11 for the second test build, and Table 12 and Table 13 for the X0Y0 "Bracket" Orientation Build. In the Tables below, the number of elements was given by the software after each simulation. For each mesh refinement, the "Layers per element" mesh setting was dressed by two as shown in the Tables below. Note that the mesh refinements used do not cause a linear increase in the number elements nor a

consistent rate of increase for every build. In addition, the study in this work used the z-displacement residual for the mesh comparisons, and the criterion for convergence was that the percentage difference had to be less than ±2 percent. The coordinates chosen for each build were where the z-displacement was maximum on the first mesh.

Table 8: Mesh settings used for the grid convergence study of Test Build #1

Mesh #	# Elements	Meshing Approach	Padding Tolerance (mm)
1	422192	Layer Based	0.05
2	576301	Layer Based	0.05
3	780274	Layer Based	0.05
Mesh #	**Max Adaptivity Levels**	**Coasrsing Generations**	**Layers per Element**
1	5	1	16
2	5	1	14
3	5	1	12

Table 9: Displacement comparison results for the grid convergence study of Test Build #1

Mesh #	X Coordinate (mm)	Y Coordinate (mm)	Z Coordinate (mm)	Z Displacement (mm)	% Difference
1	43	54	11	0.2433017	
2	43	54	11	0.2349301	-3.44083087
3	43	54	11	0.2396272	1.999360661

Table 10: Mesh settings used for the grid convergence study of Test Build #2

Mesh #	# Elements	Meshing Approach	Padding Tolerance (mm)
1	1011789	Layer Based	0.05
2	1426307	Layer Based	0.05
3	2362945	Layer Based	0.05
Mesh #	**Max Adaptivity Levels**	**Coasrsing Generations**	**Layers per Element**
1	5	1	15
2	5	1	13
3	5	1	11

Table 11: Displacement comparison results for the grid convergence study of Test Build #2

Mesh #	X Coordinate (mm)	Y Coordinate (mm)	Z Coordinate (mm)	Z Displacement (mm)	% Difference
1	114	224	21	3.129578	
2	114	224	21	2.92543	-6.523179803
3	114	224	21	2.897714	-0.947416277

Table 12: Mesh settings used for the grid convergence study of X0Y0 "Bracket" orientation build

Mesh #	# Elements	Meshing Approach	Padding Tolerance (mm)
1	301594	Layer Based	0.05
2	350253	Layer Based	0.05
3	456477	Layer Based	0.05
Mesh #	**Max Adaptivity Levels**	**Coasrsing Generations**	**Layers per Element**
1	5	1	20
2	5	1	18
3	5	1	16

Table 13: Displacement comparison results for the grid convergence study of X0Y0 "Bracket" orientation build

Mesh #	X Coordinate (mm)	Y Coordinate (mm)	Z Coordinate (mm)	Z Displacement (mm)	% Difference
1	37	105	56	1.789338	
2	37	105	56	1.857504	3.809565325
3	37	105	56	1.872701	0.818140903

2.2.10: The POIs for Each Simulation

After the grid convergence study, the rest of the "Bracket" orientations were simulated using the same mesh settings as Mesh #3 for the X0Y0 "Bracket" Orientation Build (see Table 12). In addition, the Mesh #3 simulations (see Table 8 through Table 13) of Test Build #1, Test Build #2, and the X0Y0 "Bracket" Orientation Build were used for all simulation data collection. On each build, the data for this work was collected at specified points that were called POIs. The POIs for Test Build #1, Test Build #2, and the X0Y0 "Bracket" Orientation part are shown in Figure 30, Figure 31, and Figure 32 respectively. Figure 30, Figure 31, and Figure 32 are 2D SoildWorks Drawings that were generated from their respective builds, and the units for the measurements in those figures are in mm. The POIs are represented as red circles the drawings, and the blue dotted line shown in the drawings for the two test builds (Figure 30, Figure 31) separates the POIs for those builds in to two categories: "base side" and "cantilever side". The "base side" POIs are located where the cantilever is still touching the build plate. The "cantilever side" POIs are located near the edge of the overhanging portion of the cantilever. The information shown in the drawings was recreated in Netfabb Ultimate using the built-in measurement tools of Distance Point-to-Point, and Position Point in order to find the coordinates of each POI. Additionally, for the "Bracket" orientations other than X0Y0, the required coordinate transformations from those found in the X0Y0 "Bracket" Orientation were handled by Netfabb Ultimate.

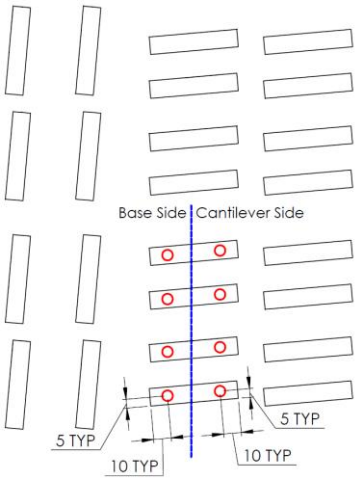

Figure 30: POI SolidWorks drawing for Test Build #1 (units: mm)

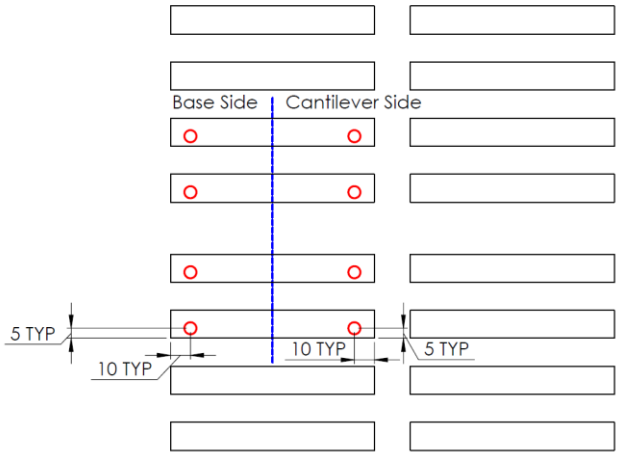

Figure 31: POI SolidWorks drawing for Test Build #2 (units: mm)

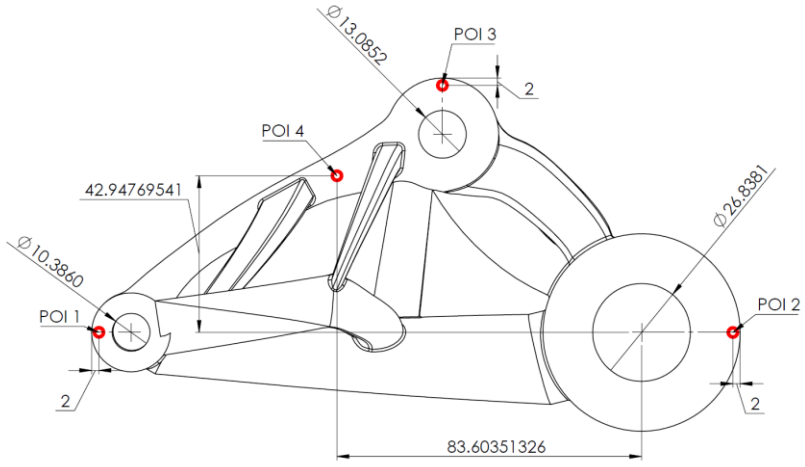

Figure 32: POI SolidWorks drawing for X0Y0 "Bracket" orientation part (units: mm)

For the first test build, the coordinates for the eight POIs that were selected which are summarized in Table 14 below. As shown in Table 14, the POIs selected for the first test build cover all four different support structures. The second test build also had eight POIs which coordinates are summarized in Table 15 below. The I and II in Table 15 represent the fact that two of 22 mm height cantilevers and two of the 24 mm height cantilevers from the second test build were analyzed. The POIs labeled with an "I" represent the lower of the two 22 mm and 24 mm height cantilevers, and the POIs label with an "II" represent the upper of the two 22 mm and 24 mm height cantilevers (see Figure 31). Each orientation of the "Bracket" part had four POIs, one each for each of the three major lugs, and one placed on a flat area of one of the arms (see Figure 32). In addition, the POIs for the "Bracket" parts are labeled as one through four, and the summary of coordinates for each POI are shown in Table 16, Table 17, Table 18, and Table 19 below.

Table 14: POI summary for Test Build #1

POI #	POI Description	POI (X,Y,Z) (mm)
1	Support Style 1 (Base)	(130.057169, 23.69253, 12)
2	Support Style 2 (Base)	(130.057169, 48.69253, 12)
3	Support Style 3 (Base)	(130.057169, 78.69253, 12)
4	Support Style 4 (Base)	(130.057169, 103.69253, 12)
5	Support Style 1 (Cantilever)	(159.943275, 26.307417, 12)
6	Support Style 2 (Cantilever)	(159.943275, 51.307417, 12)
7	Support Style 3 (Cantilever)	(159.942375, 81.307417, 12)
8	Support Style 4 (Cantilever)	(159.943275, 106.307417, 12)

Table 15: POI summary for Test Build #2

POI #	POI Description	POI (X,Y,Z) (mm)
1	4 mm Thickness (Base) I	(24, 75, 24)
2	4 mm Thickness (Base) II	(24, 103, 24)
3	2 mm Thickness (Base) I	(24, 143, 22)
4	2 mm Thickness (Base) II	(24, 171, 22)
5	4 mm Thickness (Cantilever) I	(106, 75, 24)
6	4 mm Thickness (Cantilever) II	(106, 103, 24)
7	2 mm Thickness (Cantilever) I	(106, 143, 22)
8	2 mm Thickness (Cantilever) II	(106, 171, 22)

Table 16: Coordinate summary for "Bracket" part (POI 1)

X Rotation Angle (deg)	Y Rotation Angle (deg)	POI 1 (X,Y,Z) (mm)
0	0	(38.023, 103.676, 60.956)
30	0	(38.023, 85.895, 67.139)
60	0	(38.023, 86.642, 57.038)
90	0	(38.023, 97.706, 33.352)
120	0	(38.023, 99.911, 15.763)
150	0	(38.023, 122.819, 11.747)
180	0	(38.023, 146.324, 6.368)
210	0	(38.023, 164.105, 16.961)
240	0	(38.023, 163.358, 52.676)
270	0	(38.023, 152.294, 76.000)
300	0	(38.023, 150.089, 93.972)
330	0	(38.023, 127.181, 88.464)
0	30	(65.138, 103.676, 141.619)
0	60	(108.403, 103.676, 186.040)
0	90	(152.294, 103.676, 182.311)
0	120	(192.136, 103.676, 144.765)
0	150	(213.977, 103.676, 70.129)
0	180	(211.977, 103.676, 6.368)
0	210	(184.862, 103.676, 7.348)
0	240	(141.567, 103.676, 8.086)
0	270	(97.706, 103.676, 8.356)
0	300	(57.864, 103.676, 25.041)
0	330	(36.023, 103.676, 36.934)

Table 17: Coordinate summary for "Bracket" part (POI 2)

X Rotation Angle (deg)	Y Rotation Angle (deg)	POI 2 (X,Y,Z) (mm)
0	0	(211.993, 103.635, 33.016)
30	0	(211.993, 99.830, 42.922)
60	0	(211.993, 110.818, 43.032)
90	0	(211.993, 125.646, 33.310)
120	0	(211.993, 124.128, 29.697)
150	0	(211.993, 136.825, 35.924)
180	0	(211.993, 146.365, 34.308)
210	0	(211.993, 150.170, 41.178)
240	0	(211.993, 139.182, 66.682)
270	0	(211.993, 124.354, 76.041)
300	0	(211.993, 125.872, 80.038)
330	0	(211.993, 113.175, 64.287)
0	30	(201.831, 103.635, 30.437)
0	60	(171.191, 103.635, 21.407)
0	90	(124.354, 103.635, 8.340)
0	120	(80.954, 103.635, 8.072)
0	150	(49.344, 103.635, 7.340)
0	180	(38.007, 103.635, 34.308)
0	210	(48.169, 103.635, 118.530)
0	240	(78.809, 103.635, 172.718)
0	270	(125.646, 103.635, 182.326)
0	300	(169.046, 103.635, 161.734)
0	330	(200.656, 103.635, 99.723)

Table 18: Coordinate summary for "Bracket" part (POI 3)

X Rotation Angle (deg)	Y Rotation Angle (deg)	POI 3 (X,Y,Z) (mm)
0	0	(132.273, 171.303, 33.016)
30	0	(132.273, 158.432, 76.756)
60	0	(132.273, 144.652, 101.635)
90	0	(132.273, 125.646, 100.979)
120	0	(132.273, 90.294, 88.300)
150	0	(132.273, 78.222, 69.758)
180	0	(132.273, 78.697, 34.308)
210	0	(132.273, 91.568, 7.344)
240	0	(132.273, 105.348, 8.079)
270	0	(132.273, 124.354, 8.373)
300	0	(132.273, 159.706, 21.436)
330	0	(132.273, 171.778, 30.453)
0	30	(132.792, 171.303, 70.297)
0	60	(131.332, 171.303, 90.446)
0	90	(124.354, 171.303, 88.060)
0	120	(120.813, 171.303, 77.111)
0	150	(118.384, 171.303, 47.200)
0	180	(117.727, 171.303, 34.308)
0	210	(117.308, 171.303, 78.670)
0	240	(118.668, 171.303, 103.679)
0	270	(125.646, 171.303, 102.607)
0	300	(129.187, 171.303, 92.695)
0	330	(131.616, 171.303, 59.863)

Table 19: Coordinate summary for "Bracket" part (POI 4)

X Rotation Angle (deg)	Y Rotation Angle (deg)	POI 4 (X,Y,Z) (mm)
0	0	(103.325, 146.583, 33.016)
30	0	(103.325, 137.024, 64.397)
60	0	(103.325, 132.292, 80.227)
90	0	(103.325, 125.646, 76.259)
120	0	(103.325, 102.654, 66.892)
150	0	(103.325, 99.630, 57.398)
180	0	(103.325, 103.417, 34.308)
210	0	(103.325, 112.976, 19.704)
240	0	(103.325, 117.708, 29.487)
270	0	(103.325, 124.354, 33.092)
300	0	(103.325, 147.346, 42.843)
330	0	(103.325, 150.370, 42.813)
0	30	(107.722, 146.583, 84.711)
0	60	(116.858, 146.583, 115.516)
0	90	(124.354, 146.583, 117.008)
0	120	(135.287, 146.583, 102.181)
0	150	(143.453, 146.583, 61.674)
0	180	(146.675, 146.583, 34.308)
0	210	(142.278, 146.583, 64.196)
0	240	(133.142, 146.583, 78.609)
0	270	(125.646, 146.583, 73.658)
0	300	(114.713, 146.583, 67.625)
0	330	(106.547, 146.583, 45.389)

2.2.11: Data Collection: Overview

Netfabb's Simulation Utility outputs several residuals for each simulation, and these residuals are shown in Figure 33 below. One thing to note is that the existence for some of these residuals can be controlled by the solver settings shown in Figure 25. For this work, the simulation data that were collected for each simulation is as follows: x-displacement, y-displacement, z-displacement, displacement magnitude, XX stress, YY stress, ZZ stress, XY stress, the Von Mises stress, and the build's minimum recoater clearance (BMRC). This data was to be collected at two different time steps: PTS, and the substrate removal time step (SRTS). The SRTS is a time step that models the effect on the part after the build plate was removed.

2.2.12: Data Collection: Displacement

The displacement data for both time steps (PTS and SRTS) were collected using the post-processing tool called “timex”. The tool “timex” is a command prompt command that outputs a text file that has the following information for every time step: the x-displacement, y-displacement, z-displacement, and displacement magnitude. In order to use the “timex” command, the following criteria must be met. First, a script in the form of a text file must be written using the format shown in Figure 34 below. Second, the script file must be placed in the same directory as the input file. Third, the command prompt directory must be set to the same folder that the input file is located. Fourth, once a script file is created the following command must be entered into command prompt: timex <timex script filename.txt>. Fifth, the coordinates entered into the script file must exist on the generated mesh. Because of differences between the generated mesh and the original 3MF file, the mapped POI coordinates that were are shown in Table 14 though Table 19 may be absent from the mesh or the coordinates might be associated with the support structure instead of the part. In these cases, the coordinates imported into the script file were slightly modified from their respective mapped POI. The coordinates that were used in the “timex” scripts were called: “timex” POI, and these coordinates and their respective mapped POIs coordinates are shown in Table 20 through Table 25 below.

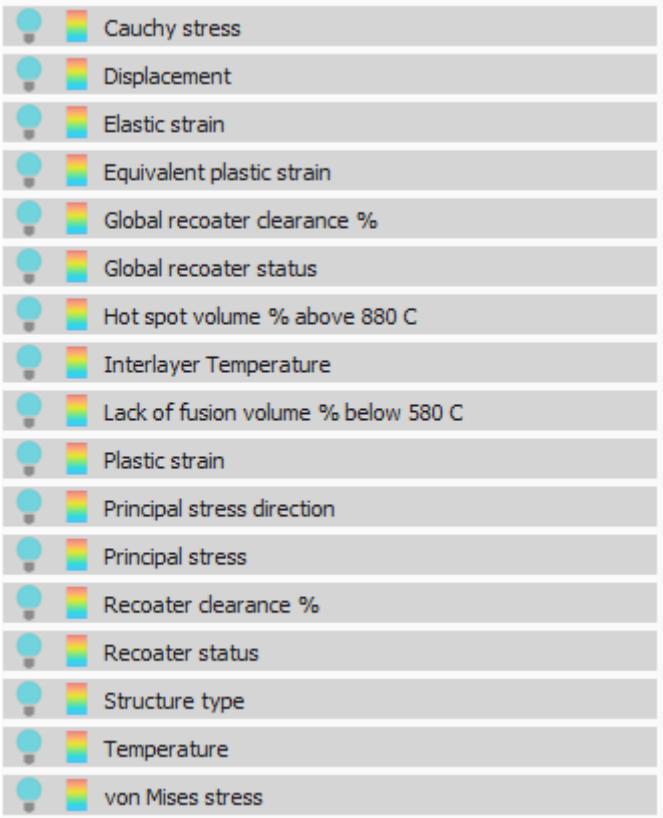

Figure 33: List of outputted residuals for each simulation

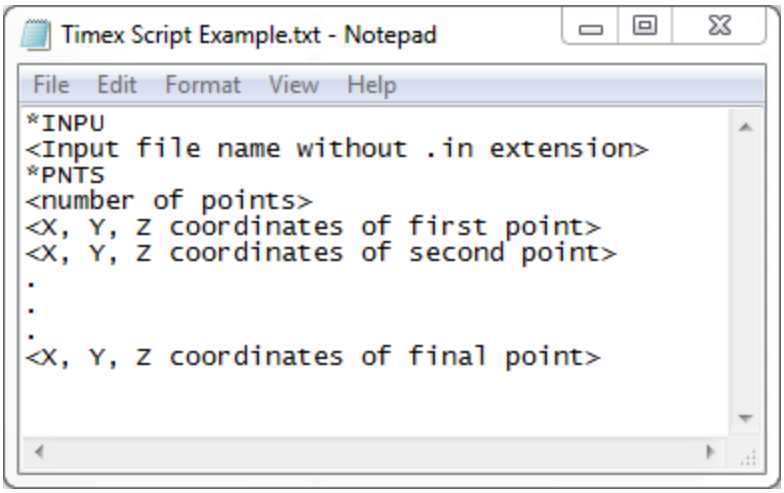

Figure 34: Example of "timex" command script

Table 20: "Timex" POIs vs. mapped POIs for Test Build #1

POI #	Mapped POI (X,Y,Z) (mm)	"timex" POI (X,Y,Z) (mm)
1	(130.057169, 23.69253, 12)	(130.057169, 23.69253, 11.88)
2	(130.057169, 48.69253, 12)	(130.057169, 48.69253, 11.88)
3	(130.057169, 78.69253, 12)	(130.057169, 78.69253, 11.88)
4	(130.057169, 103.69253, 12)	(130.057169, 103.69253, 11.88)
5	(159.943275, 26.307417, 12)	(159.943275, 26.307417, 11.88)
6	(159.943275, 51.307417, 12)	(159.943275, 51.307417, 11.88)
7	(159.942375, 81.307417, 12)	(159.942375, 81.307417, 11.88)
8	(159.943275, 106.307417, 12)	(159.943275, 106.307417, 11.88)

Table 21: "Timex" POIs vs. mapped POIs for Test Build #2

POI #	Mapped POI (X,Y,Z) (mm)	"timex" POI (X,Y,Z) (mm)
1	(24, 75, 24)	(24, 75, 24.09)
2	(24, 103, 24)	(24, 103, 24.09)
3	(24, 143, 22)	(24, 143, 22.11)
4	(24, 171, 22)	(24, 171, 22.11)
5	(106, 75, 24)	(106, 75, 24.09)
6	(106, 103, 24)	(106, 103, 24.09)
7	(106, 143, 22)	(106, 143, 22.11)
8	(106, 171, 22)	(106, 171, 22.11)

Table 22: "Timex" coordinates vs. mapped coordinates for "Bracket" part (POI 1)

X Rotation Angle (deg)	Y Rotation Angle (deg)	POI 1 Mapped (X,Y,Z) (mm)	POI 1 "timex" (X,Y,Z) (mm)
0	0	(38.023, 103.676, 60.956)	(38.023, 103.676, 60.956)
30	0	(38.023, 85.895, 67.139)	(38.023, 85.895, 67.139)
60	0	(38.023, 86.642, 57.038)	(38.023, 86.705, 57.038)
90	0	(38.023, 97.706, 33.352)	(38.023, 97.706, 33.352)
120	0	(38.023, 99.911, 15.763)	(38.023, 100.003, 15.763)
150	0	(38.023, 122.819, 11.747)	(38.023, 122.834, 11.747)
180	0	(38.023, 146.324, 6.368)	(38.023, 146.324, 6.368)
210	0	(38.023, 164.105, 16.961)	(38.023, 164.105, 16.961)
240	0	(38.023, 163.358, 52.676)	(38.023, 163.290, 52.676)
270	0	(38.023, 152.294, 76.000)	(38.023, 152.294, 76.000)
300	0	(38.023, 150.089, 93.972)	(38.023, 150.089, 93.972)
330	0	(38.023, 127.181, 88.464)	(38.023, 127.166, 88.464)
0	30	(65.138, 103.676, 141.619)	(65.138, 103.676, 141.600)
0	60	(108.403, 103.676, 186.040)	(108.403, 103.676, 186.040)
0	90	(152.294, 103.676, 182.311)	(152.294, 103.676, 182.311)
0	120	(192.136, 103.676, 144.765)	(192.136, 103.676, 144.765)
0	150	(213.977, 103.676, 70.129)	(213.977, 103.676, 70.129)
0	180	(211.977, 103.676, 6.368)	(211.977, 103.676, 6.368)
0	210	(184.862, 103.676, 7.348)	(184.862, 103.676, 7.348)
0	240	(141.567, 103.676, 8.086)	(141.567, 103.676, 8.086)
0	270	(97.706, 103.676, 8.356)	(97.706, 103.676, 8.356)
0	300	(57.864, 103.676, 25.041)	(57.864, 103.676, 25.041)
0	330	(36.023, 103.676, 36.934)	(36.023, 103.676, 36.934)

Table 23: "Timex" coordinates vs. mapped coordinates for "Bracket" part (POI 2)

X Rotation Angle (deg)	Y Rotation Angle (deg)	POI 2 Mapped (X,Y,Z) (mm)	POI 2 "timex" (X,Y,Z) (mm)
0	0	(211.993, 103.635, 33.016)	(211.993, 103.635, 33.016)
30	0	(211.993, 99.830, 42.922)	(211.993, 99.870, 42.922)
60	0	(211.993, 110.818, 43.032)	(211.993, 110.870, 43.200)
90	0	(211.993, 125.646, 33.310)	(211.993, 125.646, 33.310)
120	0	(211.993, 124.128, 29.697)	(211.993, 124.128, 29.697)
150	0	(211.993, 136.825, 35.924)	(211.993, 136.825, 36.000)
180	0	(211.993, 146.365, 34.308)	(211.993, 146.365, 34.308)
210	0	(211.993, 150.170, 41.178)	(211.993, 150.170, 41.280)
240	0	(211.993, 139.182, 66.682)	(211.993, 139.182, 66.720)
270	0	(211.993, 124.354, 76.041)	(211.993, 124.354, 76.041)
300	0	(211.993, 125.872, 80.038)	(211.993, 125.872, 80.038)
330	0	(211.993, 113.175, 64.287)	(211.993, 113.175, 64.287)
0	30	(201.831, 103.635, 30.437)	(201.831, 103.635, 30.240)
0	60	(171.191, 103.635, 21.407)	(171.191, 103.635, 21.407)
0	90	(124.354, 103.635, 8.340)	(124.354, 103.635, 8.340)
0	120	(80.954, 103.635, 8.072)	(80.954, 103.635, 8.072)
0	150	(49.344, 103.635, 7.340)	(49.344, 103.635, 7.340)
0	180	(38.007, 103.635, 34.308)	(38.007, 103.635, 34.308)
0	210	(48.169, 103.635, 118.530)	(48.169, 103.635, 118.560)
0	240	(78.809, 103.635, 172.718)	(78.809, 103.635, 172.800)
0	270	(125.646, 103.635, 182.326)	(125.646, 103.635, 182.326)
0	300	(169.046, 103.635, 161.734)	(169.046, 103.635, 161.734)
0	330	(200.656, 103.635, 99.723)	(200.656, 103.635, 99.723)

Table 24: "Timex" coordinates vs. mapped coordinates for "Bracket" part (POI 3)

X Rotation Angle (deg)	Y Rotation Angle (deg)	POI 3 Mapped (X,Y,Z) (mm)	POI 3 "timex" (X,Y,Z) (mm)
0	0	(132.273, 171.303, 33.016)	(132.273, 171.303, 33.016)
30	0	(132.273, 158.432, 76.756)	(132.273, 158.432, 76.756)
60	0	(132.273, 144.652, 101.635)	(132.273, 144.652, 101.635)
90	0	(132.273, 125.646, 100.979)	(132.273, 125.646, 100.979)
120	0	(132.273, 90.294, 88.300)	(132.273, 90.294, 88.320)
150	0	(132.273, 78.222, 69.758)	(132.273, 78.222, 69.758)
180	0	(132.273, 78.697, 34.308)	(132.273, 78.697, 34.308)
210	0	(132.273, 91.568, 7.344)	(132.273, 91.568, 7.344)
240	0	(132.273, 105.348, 8.079)	(132.273, 105.348, 8.079)
270	0	(132.273, 124.354, 8.373)	(132.273, 124.354, 8.373)
300	0	(132.273, 159.706, 21.436)	(132.273, 159.706, 21.436)
330	0	(132.273, 171.778, 30.453)	(132.273, 171.778, 30.453)
0	30	(132.792, 171.303, 70.297)	(132.792, 171.303, 70.297)
0	60	(131.332, 171.303, 90.446)	(131.332, 171.303, 90.240)
0	90	(124.354, 171.303, 88.060)	(124.354, 171.303, 88.060)
0	120	(120.813, 171.303, 77.111)	(120.740, 171.303, 77.111)
0	150	(118.384, 171.303, 47.200)	(118.384, 171.303, 47.200)
0	180	(117.727, 171.303, 34.308)	(117.727, 171.303, 34.308)
0	210	(117.308, 171.303, 78.670)	(117.308, 171.303, 78.720)
0	240	(118.668, 171.303, 103.679)	(118.680, 171.303, 103.679)
0	270	(125.646, 171.303, 102.607)	(125.646, 171.303, 102.607)
0	300	(129.187, 171.303, 92.695)	(129.260, 171.303, 92.695)
0	330	(131.616, 171.303, 59.863)	(131.616, 171.303, 59.863)

Table 25: "Timex" coordinates vs. Mapped coordinates for "Bracket" part (POI 4)

X Rotation Angle (deg)	Y Rotation Angle (deg)	POI 4 Mapped (X,Y,Z) (mm)	POI 4 "timex" (X,Y,Z) (mm)
0	0	(103.325, 146.583, 33.016)	(103.325, 146.583, 33.016)
30	0	(103.325, 137.024, 64.397)	(103.325, 137.132, 64.397)
60	0	(103.325, 132.292, 80.227)	(103.325, 132.292, 80.160)
90	0	(103.325, 125.646, 76.259)	(103.325, 125.646, 76.259)
120	0	(103.325, 102.654, 66.892)	(103.325, 102.681, 66.892)
150	0	(103.325, 99.630, 57.398)	(103.325, 99.630, 57.398)
180	0	(103.325, 103.417, 34.308)	(103.325, 103.417, 34.308)
210	0	(103.325, 112.976, 19.704)	(103.325, 112.976, 19.704)
240	0	(103.325, 117.708, 29.487)	(103.325, 117.708, 29.760)
270	0	(103.325, 124.354, 33.092)	(103.325, 124.354, 33.092)
300	0	(103.325, 147.346, 42.843)	(103.325, 147.319, 42.843)
330	0	(103.325, 150.370, 42.813)	(103.325, 150.370, 42.720)
0	30	(107.722, 146.583, 84.711)	(107.722, 146.583, 84.711)
0	60	(116.858, 146.583, 115.516)	(116.858, 146.583, 115.516)
0	90	(124.354, 146.583, 117.008)	(124.354, 146.583, 117.008)
0	120	(135.287, 146.583, 102.181)	(135.287, 146.583, 102.181)
0	150	(143.453, 146.583, 61.674)	(143.428, 146.583, 61.674)
0	180	(146.675, 146.583, 34.308)	(146.675, 146.583, 34.308)
0	210	(142.278, 146.583, 64.196)	(142.278, 146.583, 64.320)
0	240	(133.142, 146.583, 78.609)	(133.142, 146.583, 78.609)
0	270	(125.646, 146.583, 73.658)	(125.646, 146.583, 73.658)
0	300	(114.713, 146.583, 67.625)	(114.713, 146.583, 67.625)
0	330	(106.547, 146.583, 45.389)	(106.572, 146.583, 45.389)

2.2.13: Data Collection: Stress

For Cauchy and Von Mises stress results at the PTS, the models used for the displacement data collection were rerun with the FHT described in Section 2.2.6 and Figure 22. The reason behind using the FHT is that when plasticity is turned on without a heat treatment the Cauchy stress data is limited only to steps after the PTS and when a heat treatment of any kind is used in a simulation model with plasticity enabled the Cauchy stress results become available for the PTS. However, the Von Mises stress data at the PTS is available without a heat treatment and the only reason that data was collected from the FHT models was to ensure that all the stress data at the PTS was consistent. For the SRTS the Cauchy and Von Mises stress data was collected from the same model as the ones used for the displacement data collection. For both time the stress data was collected using the probe tool within the simulation software (command prompt not needed). The probe tool allows the user to view simulation results at any node and at any time step on the mesh for that simulation. The simulation results shown in the tool can be for just the selected residual, from the list shown in Figure 33, or all the residuals. Some residuals show multiple values in the probe tool when selected. For example, for the Cauchy stress residual contains the values of the XX, YY, ZZ, XY, XZ, YZ stresses. There are two main methods in selecting a node. The first method is to click on the desired node on the actual mesh; the

second method is to type in the coordinates and have the software find the closest node on that mesh to the inputted coordinates. The XX, YY, ZZ, and XY stress data was collected from Cauchy stress residual, and the Von Mises stress data was collected form Von Mises stress residual. For all simulations in this work, the nodes the corresponded with each mapped POI had different coordinates, which is shown in Table 26 through Table 31 below.

Table 26: Nodal POIs vs. mapped POIs for Test Build #1

POI #	Mapped POI (X,Y,Z) (mm)	Nodal POI (X,Y,Z) (mm)
1	(130.057169, 23.69253, 12)	(130.08, 23.642, 11.88)
2	(130.057169, 48.69253, 12)	(130.08, 48.713, 11.88)
3	(130.057169, 78.69253, 12)	(130.08, 78.798, 11.88)
4	(130.057169, 103.69253, 12)	(130.08, 103.87, 11.88)
5	(159.943275, 26.307417, 12)	(159.91, 26.149, 11.88)
6	(159.943275, 51.307417, 12)	(159.91, 51.22, 11.88)
7	(159.942375, 81.307417, 12)	(159.91, 81.305, 11.88)
8	(159.943275, 106.307417, 12)	(159.91, 106.38, 11.88)

Table 27: Nodal POIs vs. mapped POIs for Test Build #2

POI #	Mapped POI (X,Y,Z) (mm)	Nodal POI (X,Y,Z) (mm)
1	(24, 75, 24)	(24.091, 74.861, 24.09)
2	(24, 103, 24)	(24.091, 102.93, 24.09)
3	(24, 143, 22)	(24.091, 142.97, 22.11)
4	(24, 171, 22)	(24.091, 171.04, 22.11)
5	(106, 75, 24)	(106.08, 74.861, 24.09)
6	(106, 103, 24)	(106.08, 102.93, 24.09)
7	(106, 143, 22)	(106.08, 142.97, 22.11)
8	(106, 171, 22)	(106.08, 171.04, 22.11)

Table 28: Nodal coordinates vs. mapped coordinates for "Bracket" part (POI 1)

X Rotation Angle (deg)	Y Rotation Angle (deg)	POI 1 Mapped (X,Y,Z) (mm)	POI 1 Nodal (X,Y,Z) (mm)
0	0	(38.023, 103.676, 60.956)	(37.861, 103.85, 60.960)
30	0	(38.023, 85.895, 67.139)	(37.861, 86.005, 67.200)
60	0	(38.023, 86.642, 57.038)	(37.861, 86.705, 56.640)
90	0	(38.023, 97.706, 33.352)	(37.861, 97.678, 32.640)
120	0	(38.023, 99.911, 15.763)	(37.861, 100.00, 15.840)
150	0	(38.023, 122.819, 11.747)	(37.861, 122.83, 11.520)
180	0	(38.023, 146.324, 6.368)	(37.861, 146.15, 6.2400)
210	0	(38.023, 164.105, 16.961)	(37.861, 164.00, 16.800)
240	0	(38.023, 163.358, 52.676)	(37.861, 163.29, 52.800)
270	0	(38.023, 152.294, 76.000)	(37.861, 152.32, 76.800)
300	0	(38.023, 150.089, 93.972)	(37.861, 150.00, 94.080)
330	0	(38.023, 127.181, 88.464)	(37.861, 127.17, 88.320)
0	30	(65.138, 103.676, 141.619)	(65.185, 103.85, 141.60)
0	60	(108.403, 103.676, 186.040)	(108.57, 103.85, 186.24)
0	90	(152.294, 103.676, 182.311)	(152.32, 103.42, 182.40)
0	120	(192.136, 103.676, 144.765)	(192.20, 103.58, 144.96)
0	150	(213.977, 103.676, 70.129)	(213.83, 103.85, 70.080)
0	180	(211.977, 103.676, 6.368)	(212.14, 103.85, 6.2400)
0	210	(184.862, 103.676, 7.348)	(184.82, 103.85, 7.2000)
0	240	(141.567, 103.676, 8.086)	(141.43, 103.85, 8.1600)
0	270	(97.706, 103.676, 8.356)	(97.678, 103.42, 7.6800)
0	300	(57.864, 103.676, 25.041)	(57.803, 103.85, 24.960)
0	330	(36.023, 103.676, 36.934)	(36.167, 103.85, 36.960)

Table 29: Nodal coordinates vs. mapped coordinates for "Bracket" part (POI 2)

X Rotation Angle (deg)	Y Rotation Angle (deg)	POI 2 Mapped (X,Y,Z) (mm)	POI 2 Nodal (X,Y,Z) (mm)
0	0	(211.993, 103.635, 33.016)	(212.14, 103.42, 33.120)
30	0	(211.993, 99.830, 42.922)	(212.14, 99.870, 42.720)
60	0	(211.993, 110.818, 43.032)	(212.14, 110.87, 43.200)
90	0	(211.993, 125.646, 33.310)	(212.14, 125.85, 33.120)
120	0	(211.993, 124.128, 29.697)	(212.14, 124.11, 29.760)
150	0	(211.993, 136.825, 35.924)	(212.14, 136.70, 36.000)
180	0	(211.993, 146.365, 34.308)	(212.14, 146.58, 34.080)
210	0	(211.993, 150.170, 41.178)	(212.14, 150.13, 41.280)
240	0	(211.993, 139.182, 66.682)	(212.14, 139.13, 66.720)
270	0	(211.993, 124.354, 76.041)	(212.14, 124.15, 75.840)
300	0	(211.993, 125.872, 80.038)	(212.14, 125.89, 79.680)
330	0	(211.993, 113.175, 64.287)	(212.14, 112.87, 64.320)
0	30	(201.831, 103.635, 30.437)	(201.78, 103.42, 30.240)
0	60	(171.191, 103.635, 21.407)	(171.35, 103.42, 21.600)
0	90	(124.354, 103.635, 8.340)	(124.15, 103.42, 8.1600)
0	120	(80.954, 103.635, 8.072)	(80.991, 103.42, 8.1600)
0	150	(49.344, 103.635, 7.340)	(49.398, 103.42, 7.2000)
0	180	(38.007, 103.635, 34.308)	(37.861, 103.42, 34.080)
0	210	(48.169, 103.635, 118.530)	(48.223, 103.42, 118.56)
0	240	(78.809, 103.635, 172.718)	(78.651, 103.42, 172.80)
0	270	(125.646, 103.635, 182.326)	(125.85, 103.42, 182.40)
0	300	(169.046, 103.635, 161.734)	(169.01, 103.42, 161.76)
0	330	(200.656, 103.635, 99.723)	(200.60, 103.42, 99.840)

Table 30: Nodal coordinates vs. mapped coordinates for "Bracket" part (POI 3)

X Rotation Angle (deg)	Y Rotation Angle (deg)	POI 3 Mapped (X,Y,Z) (mm)	POI 3 Nodal (X,Y,Z) (mm)
0	0	(132.273, 171.303, 33.016)	(132.42, 171.18, 33.120)
30	0	(132.273, 158.432, 76.756)	(132.42, 158.80, 76.800)
60	0	(132.273, 144.652, 101.635)	(132.42, 144.60, 101.76)
90	0	(132.273, 125.646, 100.979)	(132.42, 125.85, 100.80)
120	0	(132.273, 90.294, 88.300)	(132.42, 90.182, 88.320)
150	0	(132.273, 78.222, 69.758)	(132.42, 78.216, 69.600)
180	0	(132.273, 78.697, 34.308)	(132.42, 78.822, 34.080)
210	0	(132.273, 91.568, 7.344)	(132.42, 91.637, 7.2000)
240	0	(132.273, 105.348, 8.079)	(132.42, 105.40, 8.1600)
270	0	(132.273, 124.354, 8.373)	(132.42, 124.15, 8.1600)
300	0	(132.273, 159.706, 21.436)	(132.42, 159.82, 21.600)
330	0	(132.273, 171.778, 30.453)	(132.42, 171.78, 30.240)
0	30	(132.792, 171.303, 70.297)	(132.59, 171.18, 70.080)
0	60	(131.332, 171.303, 90.446)	(131.32, 171.18, 90.240)
0	90	(124.354, 171.303, 88.060)	(124.15, 171.18, 87.840)
0	120	(120.813, 171.303, 77.111)	(120.74, 171.18, 77.280)
0	150	(118.384, 171.303, 47.200)	(118.38, 171.18, 47.040)
0	180	(117.727, 171.303, 34.308)	(117.58, 171.18, 34.080)
0	210	(117.308, 171.303, 78.670)	(117.41, 171.18, 78.720)
0	240	(118.668, 171.303, 103.679)	(118.68, 171.18, 103.68)
0	270	(125.646, 171.303, 102.607)	(125.85, 171.18, 102.72)
0	300	(129.187, 171.303, 92.695)	(129.26, 171.18, 92.640)
0	330	(131.616, 171.303, 59.863)	(131.62, 171.18, 60.000)

Table 31: Nodal coordinates vs Mapped coordinates for "Bracket" part (POI 4)

X Rotation Angle (deg)	Y Rotation Angle (deg)	POI 4 Mapped (X,Y,Z) (mm)	POI 4 Nodal (X,Y,Z) (mm)
0	0	(103.325, 146.583, 33.016)	(103.22, 146.58, 33.120)
30	0	(103.325, 137.024, 64.397)	(103.22, 137.13, 64.320)
60	0	(103.325, 132.292, 80.227)	(103.22, 132.29, 80.160)
90	0	(103.325, 125.646, 76.259)	(103.22, 125.85, 76.320)
120	0	(103.325, 102.654, 66.892)	(103.22, 102.68, 67.200)
150	0	(103.325, 99.630, 57.398)	(103.22, 99.442, 57.600)
180	0	(103.325, 103.417, 34.308)	(103.22, 103.42, 34.080)
210	0	(103.325, 112.976, 19.704)	(103.22, 112.87, 19.680)
240	0	(103.325, 117.708, 29.487)	(103.22, 117.71, 29.760)
270	0	(103.325, 124.354, 33.092)	(103.22, 124.15, 33.120)
300	0	(103.325, 147.346, 42.843)	(103.22, 147.32, 42.720)
330	0	(103.325, 150.370, 42.813)	(103.22, 150.56, 42.720)
0	30	(107.722, 146.583, 84.711)	(107.59, 146.58, 84.480)
0	60	(116.858, 146.583, 115.516)	(116.99, 146.58, 115.68)
0	90	(124.354, 146.583, 117.008)	(124.15, 146.58, 117.12)
0	120	(135.287, 146.583, 102.181)	(135.41, 146.58, 101.76)
0	150	(143.453, 146.583, 61.674)	(143.43, 146.58, 61.440)
0	180	(146.675, 146.583, 34.308)	(146.78, 146.58, 34.080)
0	210	(142.278, 146.583, 64.196)	(142.41, 146.58, 64.320)
0	240	(133.142, 146.583, 78.609)	(133.01, 146.58, 78.720)
0	270	(125.646, 146.583, 73.658)	(125.85, 146.58, 73.440)
0	300	(114.713, 146.583, 67.625)	(114.59, 146.58, 67.680)
0	330	(106.547, 146.583, 45.389)	(106.57, 146.58, 45.600)

2.2.14: Data Collection: Recoater Clearance

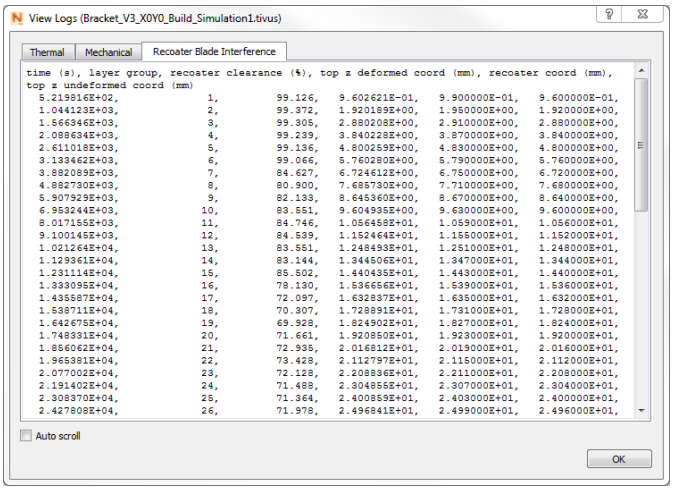

Figure 35: Example of the recoater log in Netfabb Simulation Utility

For every simulation, Netfabb Simulation Utility writes three log files that can be accessed within the software: thermal log, mechanical log, “recoater blade interference” log. The BMRC data was collected from the “recoater blade interference” log. An example

of the recoater log in shown in Figure 35 above. The recoater log records the minimum recoater clearance for each layer of the simulation, and the lowest recoater clearance value in the log was recorded as the BMRC. The BMRC were converted to maximum previous layer protrusion distance (MPLPD), and the reason for this conversion was that MPLPD can be compared to a builds layer thickness, unlike the BMRC which just a percentage. The printability of a given build was based on the MPLPD data. For example, if the MPLPD is equal or higher than a build's layer thickness than contact between the part and the recoater will occur, and thus the build was considered to have no printability. The relation between the layer thickness, BMRC, and the MPLPD is shown in Equation (2-22) where $B_{p,max}$ was the MPLPD in μm was, $C_{r,min}$ was the BMRC, and t_l was the layer thickness in μm. Note that the recoater clearance data was taken from the models without a heat treatment.

$$B_{p,max} = \left(\frac{100 - C_{r,min}}{100}\right) * t_l \quad \textbf{(2-22)}$$

2.3: Measurement Methodology

The goal of the measurements done in this work is to verify all the simulations not just the ones related to the printed builds. As mentioned previously in the beginning of Section 2.2, measurements were taken of the printed builds before and after substrate removal. The following procedure was used for the measurements of the printed builds before substrate removal. First, the printed parts were 3D scanned in order to create STL files of them. Second, these STL files were compared against their respective original CAD models using Geomagic Control X software package in order to collect distortion magnitude measurements. Third, the distortion magnitude measurements collected from Geomagic Control X software package was compared against the distortion magnitude simulation results, and then the error between the simulation and experiments is calculated.

For the off the build plate measurements, two different procedures were used depending on the build. For the printed "Bracket" builds, the procedure is the same as the one used on the builds before substrate removal. For Test Build #2, vertical distortion (z-displacement) measurements were taken using a Vernier height gauge on a ceramic table at locations close to the POIs described in Section 2.2.10. In addition, Test Build #1 was not measured in either the before or after substrate removal case due to the fact that the simulation distortion data for both cases yielded insignificant results. Detailed descriptions of each of the measurement procedures are discussed below.

2.3.1: 3D Scanning

The 3D scanning was performed using Creaform Ametek HandyScan 700 shown in Figure 36. The HandyScan 700 uses lasers, software package called VXelements, and special small white and black stickers called positioning targets to recreate a real-world object into a 3D mesh of that objects. The HandyScan 700 also has a scanning resolution of 200 microns.

Figure 36: The HandyScan 700

The following procedure to use the HandyScan 700. First, the scanner was calibrated using the white plate shown in Figure 37. Second, due to the reflective nature of the metal parts and the fact that reflective surfaces creates a lot noise during scanning, SKD-S2 Aerosol powder (see Figure 38) was sprayed on the parts which gives the parts a white non-reflective coat. Third, each build was placed one-at-a-time on the brown plate shown in Figure 39 and scanned using the HandiScan. Fourth, the mesh created form each build were cleaned up in VXelements and saved as an STL file.

Figure 37: The calibration plate to be use with the HandyScan

Figure 38: A can of SKD-S2 aerosol

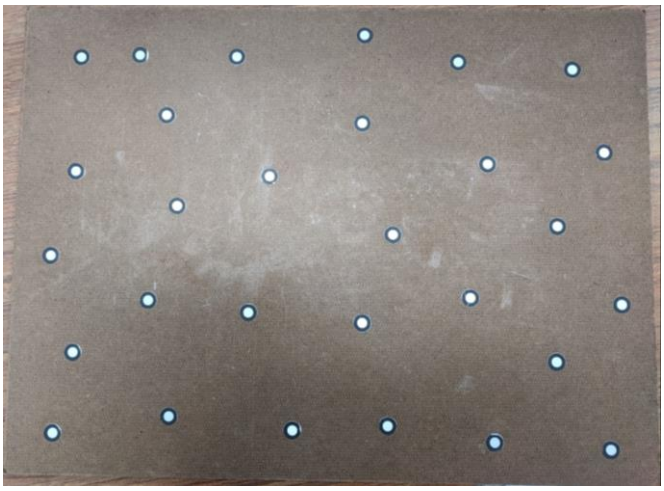

Figure 39: The brown plate that is placed under the parts that will be scanned

2.3.2: Geomagic Control X

As mentioned previously the Geomagic Control X (GCX) software package was used to gain distortion measurements form the printed builds, however, to do this it needs the copy of the undistorted part for comparison. The file format used for the undistorted models of the printed build for this work is a Drawing eXchange Format (DXF) file, and since all the undistorted files used in the simulations were in the STL file format, a conversion was necessary. This conversion was done by opening the undistorted STL files in a software called MeshLab and the saving the model as a DXF. For each of the "Bracket" builds, both the undistorted model and the scanned STL were loaded into the software, then they were aligned to each other using the "initial alignment" and "best fit alignment" tools, after that the distortion magnitude data was acquired by comparing both models of each build to each other using the "comparison" tool at location near the

defined POIs, and finally, a report was generated from the software showing the results. For Test Build #2, the following procedure was used. First, the undistorted DXF file was loaded into GCX, and then each cantilever was split into its own file. Second, the same splitting was also done to the distorted STL files. Third, four of the twelve cantilevers were selected for comparison based on the POIs for Test Build #2. Fourth, each of the distorted STL files for the chosen cantilevers was aligned to the XY plane, and this was done to help with part alignment. Fifth, distorted, and undistorted models for each cantilever was aligned to each other using the "initial alignment" and "best fit alignment" tools. Sixth, at the distortion magnitude data was acquired by comparing both models of each of the selected cantilever to each other using the "comparison" tool at location near the defined POIs. Seventh, a report was generated from the software showing the results.

2.3.3: Error Analysis Calculations

To compare the Netfabb and GCX distortion data, two values were used: gap distance error, and the gap distance percentage error. Gap distance is the distance between a point on the undeformed model (reference point) and a point on the deformed model (measured point) were those two points aligned along an axis normal to the undeformed surface at the reference point as shown in Figure 40. In addition, the gap distance can positive or negative based on the direction the gap distortion vector, where the direction of the positive normal vector is positive as shown in Figure 40.

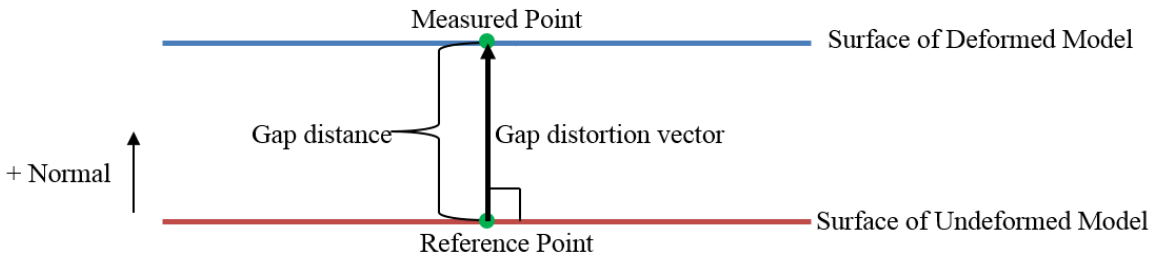

Figure 40: A visual example of gap distance, and gap direction vector

In GCX, the gap distance and gap distortion vector for each POI was given by the generated reports discussed in the previous section, but for the case of Netfabb this information was not given. Netfabb tracks how an individual node moves as the model distorts regardless of the normal vector of the surface that node (see Figure 41). So, in order to get the gap distance and the gap distortion vector for Netfabb, the following procedure was used. First, for each POI on the printed build the distortion vectors were calculated for the Netfabb data. Second, the Netfabb distortion vector was projected on the GCX gap distortion vector using Equation (2-23) where $\boldsymbol{G}_{GCX}$ is the GCX gap distortion vector, $\boldsymbol{\delta}_N$ is the Netfabb distortion vector, $\|\boldsymbol{G}_{GCX}\|$ is the magnitude of the GCX gap distortion vector, and $\boldsymbol{G}_N$ is the

Netfabb gap distortion vector. A visual representation of the projection performed here is shown in Figure 41.

$$\boldsymbol{G_N} = \left(\frac{\boldsymbol{\delta_N} \cdot \boldsymbol{G_{GCX}}}{\|\boldsymbol{G_{GCX}}\|}\right)\frac{\boldsymbol{G_{GCX}}}{\|\boldsymbol{G_{GCX}}\|} \quad (2\text{-}23)$$

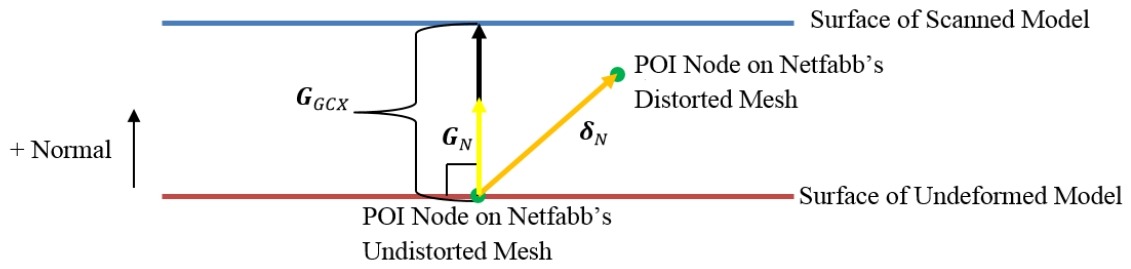

Figure 41: Netfabb's distortion measuring method, and the vector projection preformed in the work

Third, the gap distance for Netfabb was calculated using Equation (2-24) where $(GD)_N$ is the Netfabb gap distance.

$$(GD)_N = \pm\|\boldsymbol{G_N}\| \quad (2\text{-}24)$$

The gap distance error (E_{GD}) is calculated by Equation (2-25) where $(GD)_{GCX}$ is the GCX gap distance, the gap distance percentage error ($(PE)_{GD}$) is calculated in Equation (2-26).

$$E_{GD} = (GD)_{GCX} - (GD)_N \quad (2\text{-}25)$$

$$(PE)_{GD} = \frac{E_{GD}}{(GD)_N} * 100 \quad (2\text{-}26)$$

For the comparison between Netfabb the Vernier height gauge distortion measurements, the z-displacement percentage error ($(PE)_Z$) was used. This percentage error was calculated using Equation (2-27) where Z_v is the measurement made by the Vernier height gauge.

$$(PE)_Z = \frac{Z_v - (\boldsymbol{\delta_N} \cdot \boldsymbol{k})}{\boldsymbol{\delta_N} \cdot \boldsymbol{k}} * 100 \quad (2\text{-}27)$$

CHAPTER 3 :
RESULTS AND DISCUSSION

3.1: Simulation Results

Using the methods described in Section 2.2.11 through Section 2.2.14, the results of this work's simulations along with a discussion of those results are presented in Sections 3.1.1 through 3.1.7

3.1.1: Displacement Results: PTS

The PTS results from the simulations were placed on plots as shown in Figure 42 through Figure 68. The directional displacement results (x-displacement, y-displacement, and z-displacement) were placed on a separate plot from the displacement magnitude. The legend for the directional displacement plots reads as follows δ_x is the x-displacement, δ_y is the y-displacement, and δ_z is the z-displacement. The value of zero for the y-axis is marked with a dotted line. For the test builds, the resolution for the y-axis between the two displacement plots were kept the same; while for the "Bracket" builds, the y-axis resolution was kept the same for all the POIs as well as across the directional and magnitude displacement plots for each POI. The plots for the "Bracket" builds are split once more into X Orientation Builds and Y Orientation Builds making a total for four plots for each POI on the "Bracket" part. The X Orientations Builds were defined as the "Bracket" builds that just had only rotation about the x-axis, and the Y Orientation Builds were defined as the "Bracket" builds that just had only rotation about the y-axis.

The PTS results for the first test build are shown in Figure 42, and Figure 43. Figure 42 is the plot for the directional displacement data, and Figure 43 is the plot for the displacement magnitude. The following observations were made from the data. First, Test Build #1 at the PTS has very small distortions compared to part dimensions with a max value of 17.5 μm. This is due to the fact that the parts for Test Build #1 were supported by supports with relatively large volumes, and the fact that the build plate and supports together are restricting deformation. Second, for any given POI the distortion was highest along the x-axis. However it was difficult to determine the cause of the trend due to the magnitude of the directional distortions being so small. Third, the cantilever and base sides of support style 4 have identical distortion magnitudes. This is caused by the fact that the support style is a solid piece, and thus the distortion resistance would be that same on both sides. Fourth, the distortion magnitude on the base side of the parts are shown to be relatively higher that the cantilever side of the parts. The higher base side distortions can be attributed to the increased to the print volume underneath the POI which restricts the x and y axis displacements more.

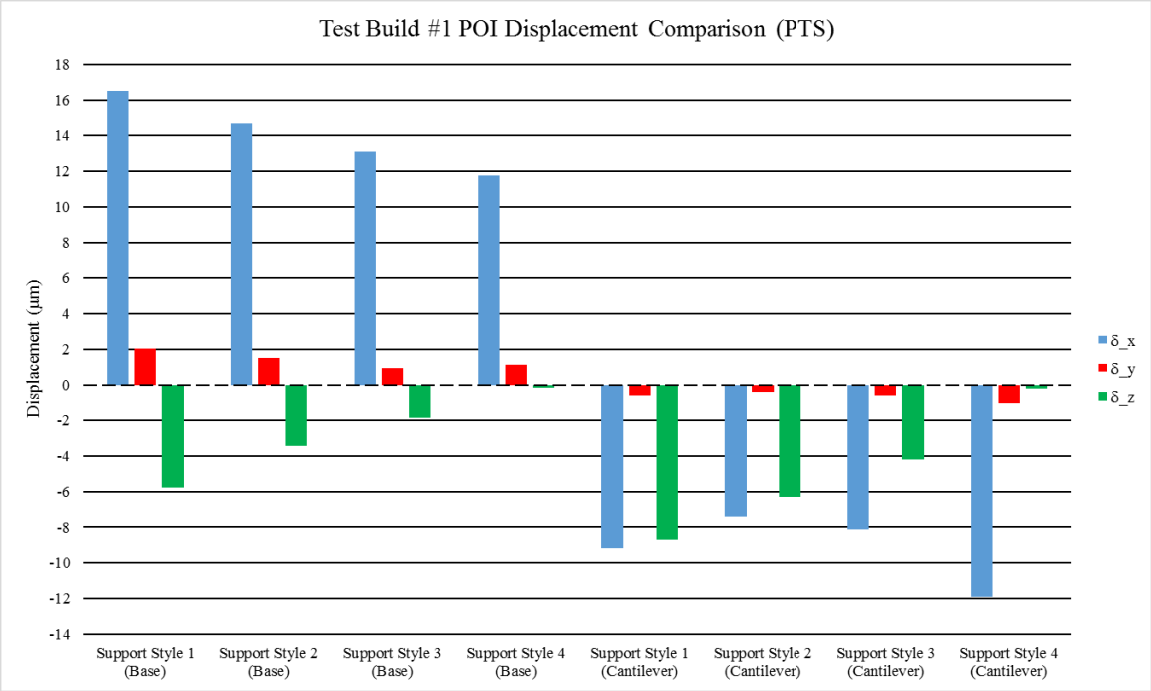

Figure 42: Directional displacement (PTS) plot for Test Build #1

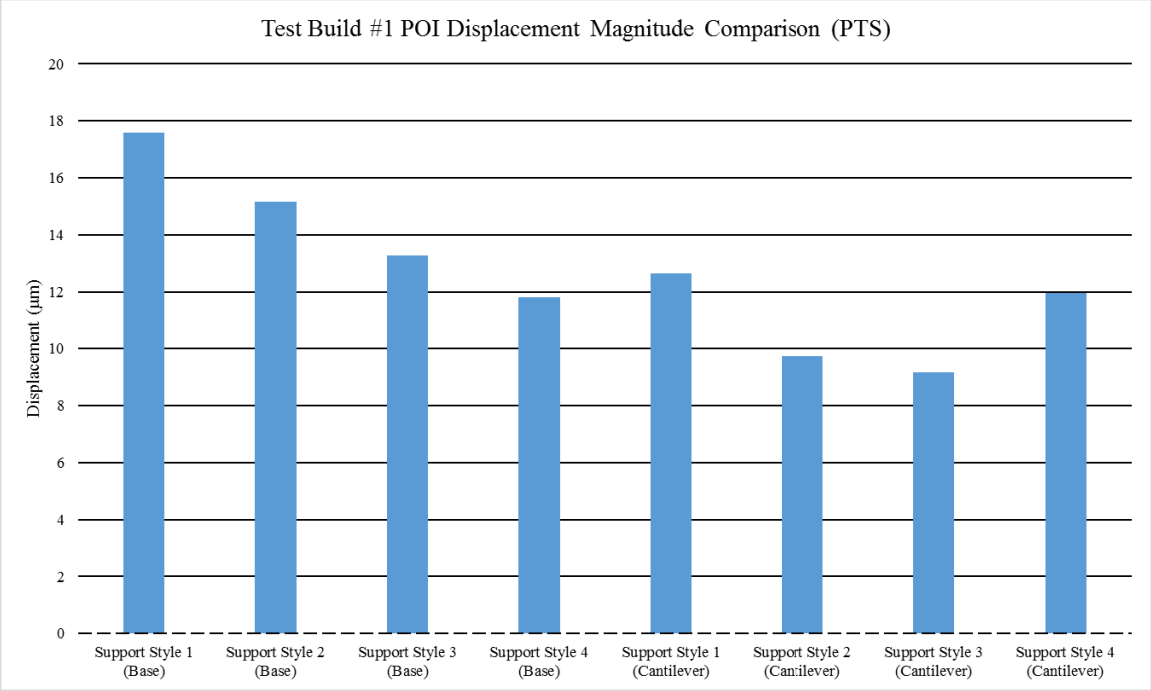

Figure 43: Displacement magnitude (PTS) plot for Test Build #1

The PTS results for the second test build are shown in Figure 44, and Figure 45. Figure 44 is the plot for the directional displacement data, and Figure 45 is the plot for the displacement magnitude data. The following observations were made based on those plots. First, Similar the Test Build #1 each POI distorts along the x-axis the most. Second, in both test builds the distortion along the x-axis is positive on base side of the part and negative on the cantilever side of the parts, and this indicates that that parts are shrunk inwards from the sides. This is caused by as the part bend toward the toward the heat source, the sides will pull toward the center as the part bends upward due to conservation of mass. Third, the displacement magnitudes from this test build are significantly larger than the Test Build #1 (see Figure 43), and the reason for this is that Test Build #1 had significantly more material volume underneath the POIs, and the Test Build #2 were longer which mean more bending stress can occur. Fourth, the displacement on the cantilever side for each part is higher than the base side; this was expected because the cantilever side has less material volume underneath the POI than the base side. Fifth, in Test Build #2, going toward the center of plate increases the displacement magnitude on the base side, but decreases the displacement magnitude on the cantilever side. By observing the POI values in Table 15 and the relative positions of the cantilevers on the build plate shown in Figure 4, it is shown that the two cantilevers closet to the center of the build plate are the 4 mm part style replicate II and the 2 mm part style replicate I. This reason for this observation was not found in this work.

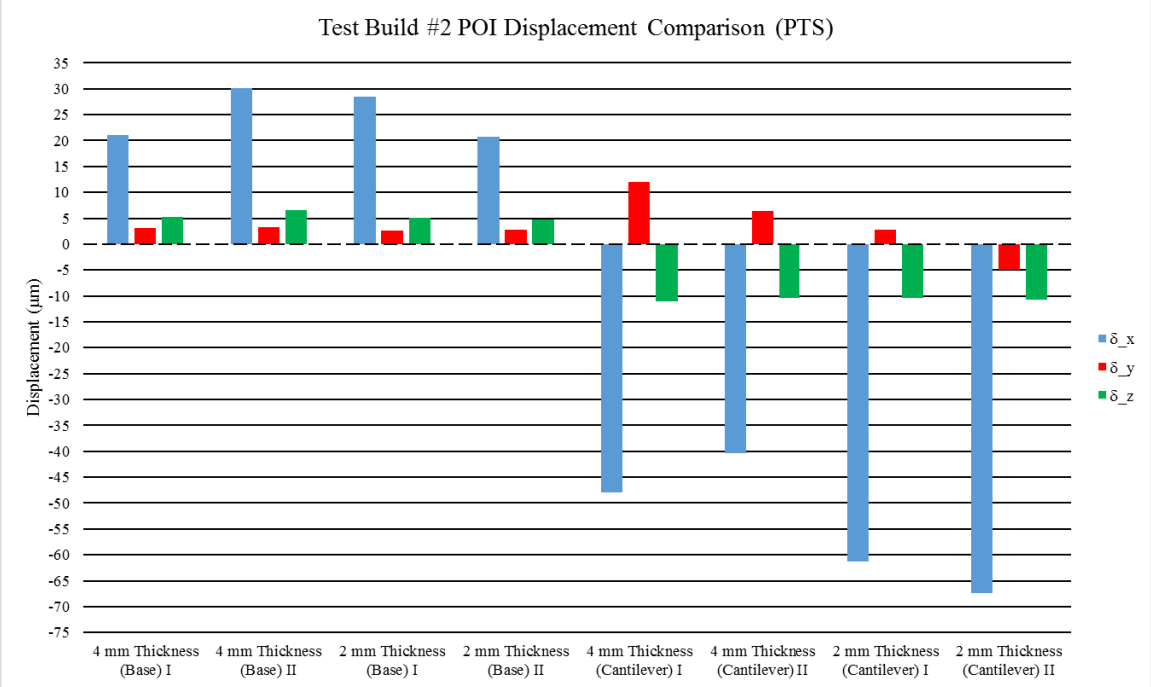

Figure 44: Directional displacement (PTS) plot for Test Build #2

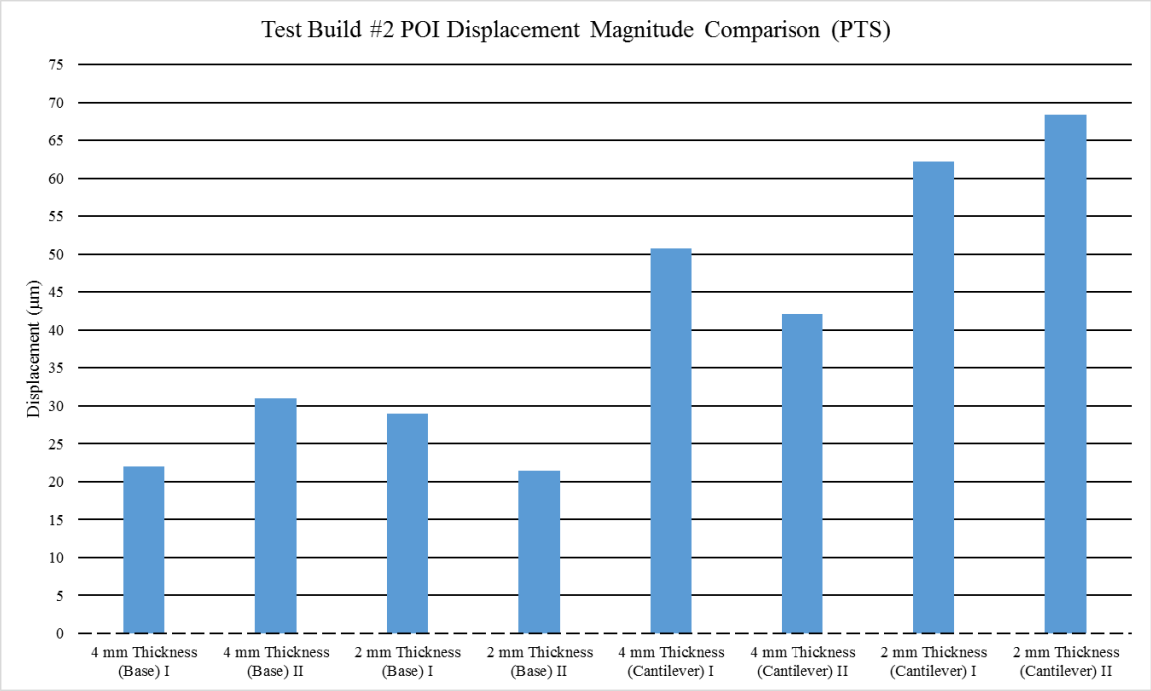

Figure 45: Displacement magnitude (PTS) plot for Test Build #2

The PTS data at POI 1 for all the orientations of the "Bracket" part build are shown in Figure 48 through Figure 51: Figure 48 is the plot for the directional displacement data of the X orientation builds, Figure 49 is the plot for the displacement magnitude data of the X orientation builds, Figure 50 is the plot for the direction displacement data of the Y, and Figure 51 is the plot for the displacement magnitude data of the Y orientation builds. Based on the aforementioned plots, the following observations were made. First, the worst orientation of the "Bracket" part orientation at POI 1 was X60Y0 with a displacement magnitude of 1.022 mm. The main contributor of the large displacement magnitude at this orientation was the y-displacement with had a value of 1.007 mm. A possible explanation for the high y-displacement comes from two major factors: the part at that orientation had very little material volume behind POI 1 in the y-direction at X60Y0, and the support structure that Netfabb generated was also very thin behind POI 1 (see Figure 46). Both factors reduce the distortion resistance at that point. Second, the best orientation of the "Bracket" part orientation at POI 1 was X0Y270 with a displacement magnitude of 0.0117 mm. In that orientation POI 1 was near the bottom of the build, and was supported with a high volume from underneath (see Figure 47). The fact the point is low on the part in that orientation means the layers that were printed after it restrict movement of that point, and the high volume underneath also restricts deformation. Third, the Y orientation "Bracket" builds had less distortion overall the X orientation "Bracket" builds at POI 1.

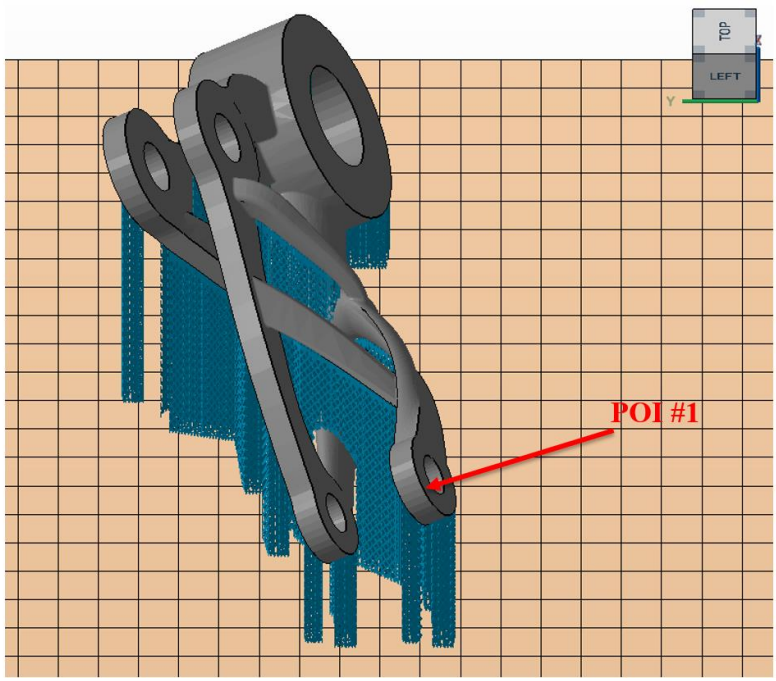

Figure 46: "Bracket" X60Y0 orientation showing the geometry and support structure around POI 1

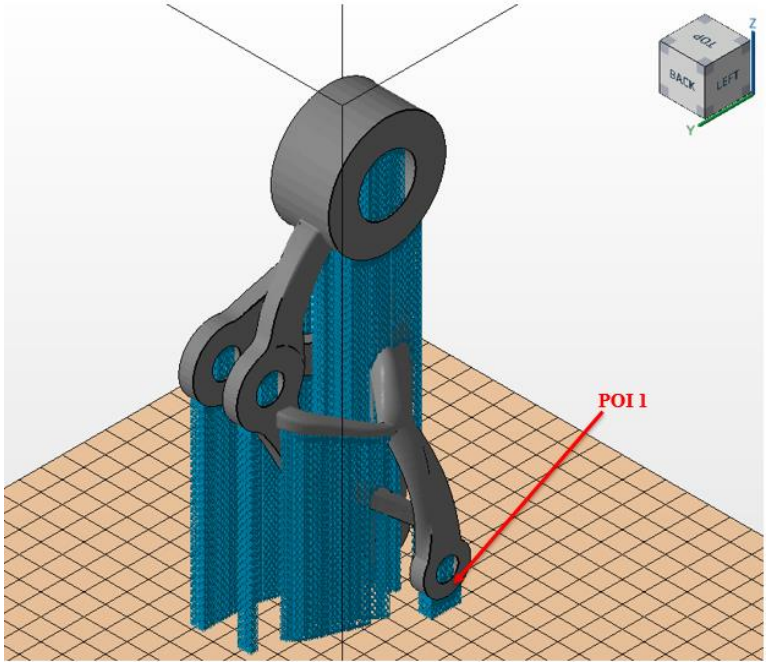

Figure 47: "Bracket" X0Y270 orientation showing the geometry and support structure around POI 1

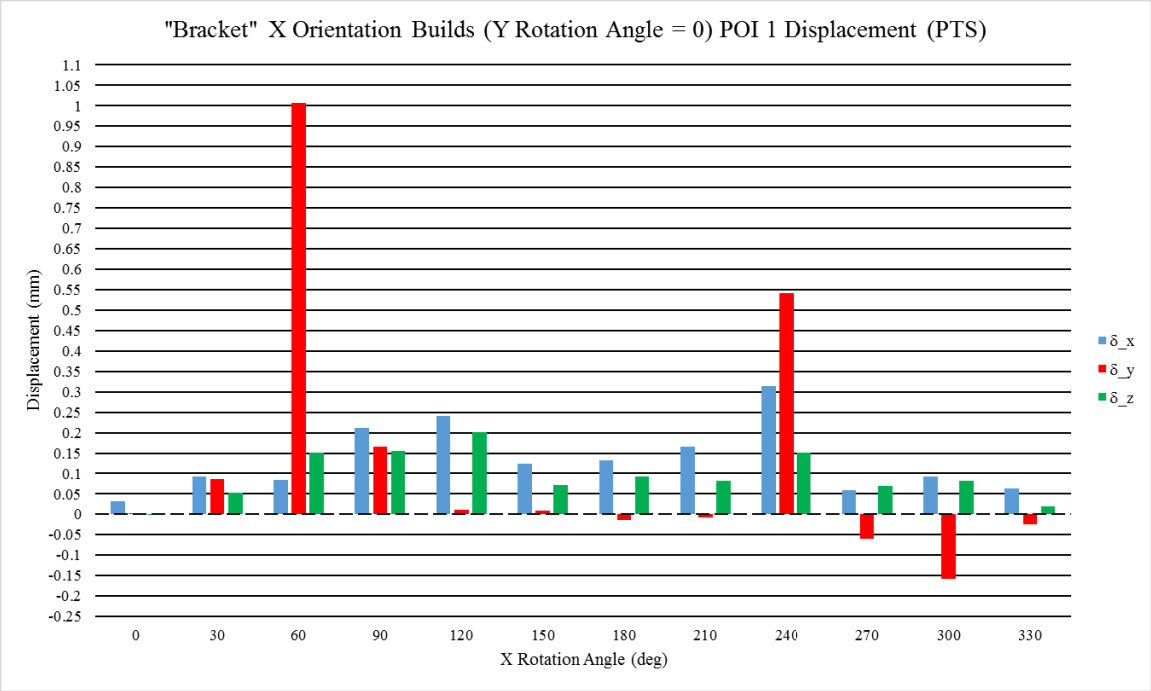

Figure 48: Directional displacement (PTS) plot for "Bracket" X Orientation Builds (POI 1)

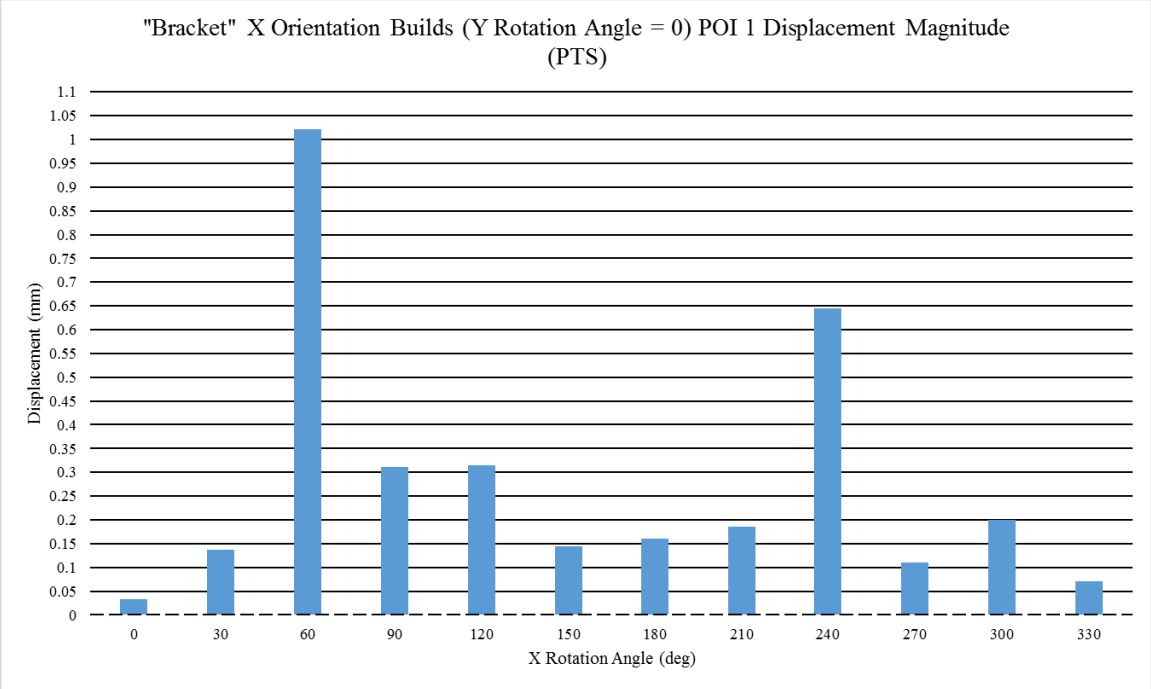

Figure 49: Displacement magnitude (PTS) plot for "Bracket" X Orientation Builds (POI 1)

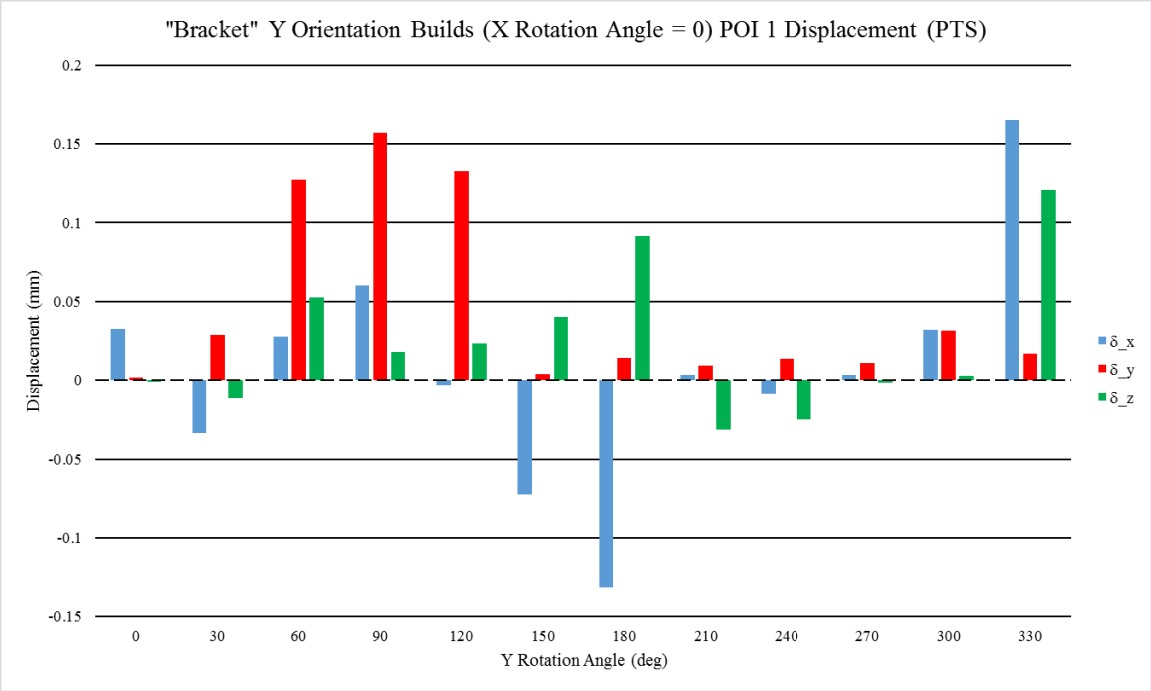

Figure 50: Directional displacement (PTS) plot for "Bracket" Y Orientation Builds (POI 1)

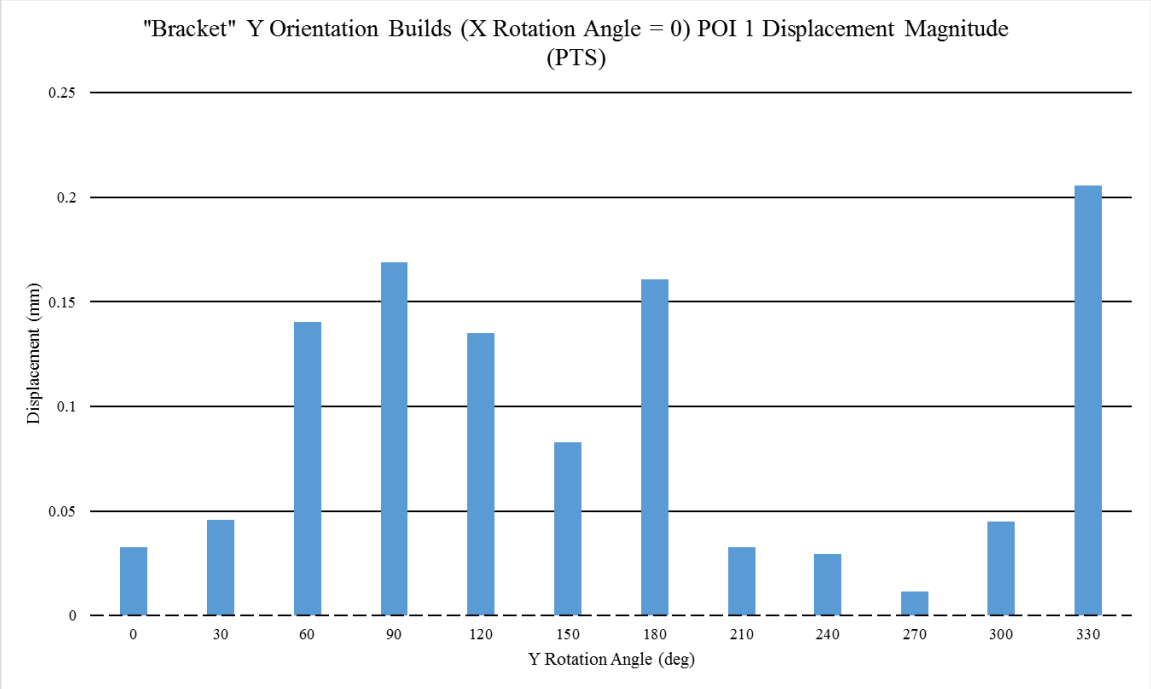

Figure 51: Displacement magnitude (PTS) plot for "Bracket" Y Orientation Builds (POI 1)

The PTS data at POI 2 for all the orientations of the "Bracket" part build are shown in Figure 54 through Figure 57: Figure 54 is the plot for the directional displacement data of the X orientation builds, Figure 55 is the plot for the displacement magnitude data of the

X orientation builds, Figure 56 is the plot for the direction displacement data of the Y, and Figure 57 is the plot for the displacement magnitude data of the Y orientation builds. Based on the aforementioned plots, the following observations were made. First, POI 2 had lower distortions overall than POI 1. This comes most likely because POI 2 on a larger and more dense part of the part than POI 1 (see Figure 32). Second, the worst orientation of the "Bracket" part orientation at POI 2 was X240Y0 with a displacement magnitude of 0.7733 mm. The distortion value at this orientation can be attributed to both the x-displacement and the z-displacement with values of -0.4426 mm and 0.5792 mm respectively. As can be seen in Figure 52, POI 2 is placed in a location were Netfabb had placed no supports, and the points location is high on the model. As mentioned previously a low support volume or lack thereof reduces the distortion resistance of a part. Third, the best orientation of the "Bracket" part at POI 2 was X0Y330 with a displacement magnitude of 0.0367 mm. There are lack of distortion at this orientation was for the fact the point has high support volume underneath it (see Figure 53), and unlike the X0Y0 orientation which has nearly the same distortion magnitude (see Figure 8) POI 2 this orientation is not at the top layer which reduces distortion.

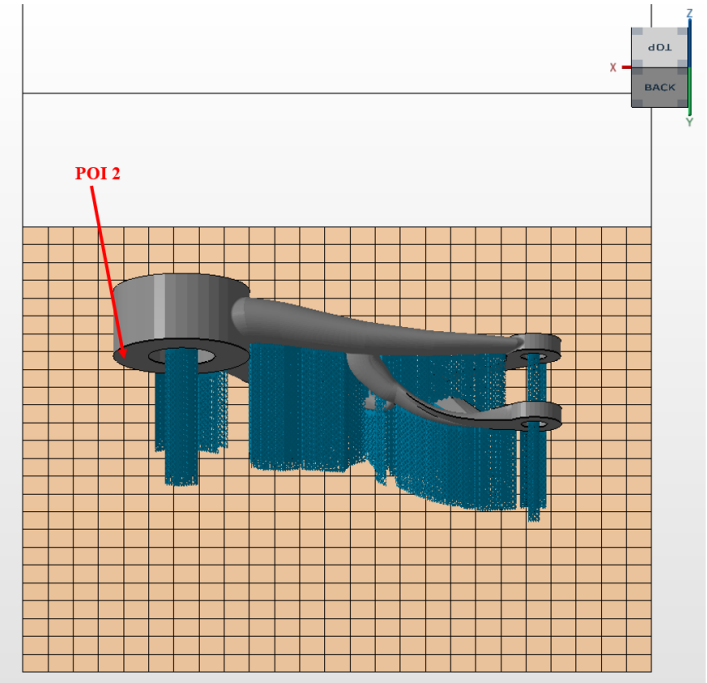

Figure 52: "Bracket" X240Y0 orientation showing the geometry and support structure around POI 2

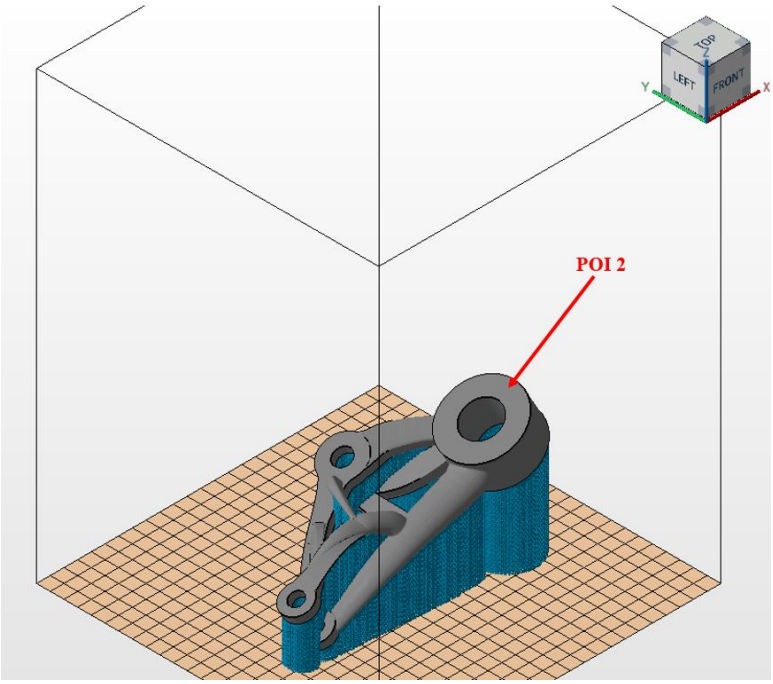

Figure 53: "Bracket" X0Y330 orientation showing the geometry and support structure around POI 2

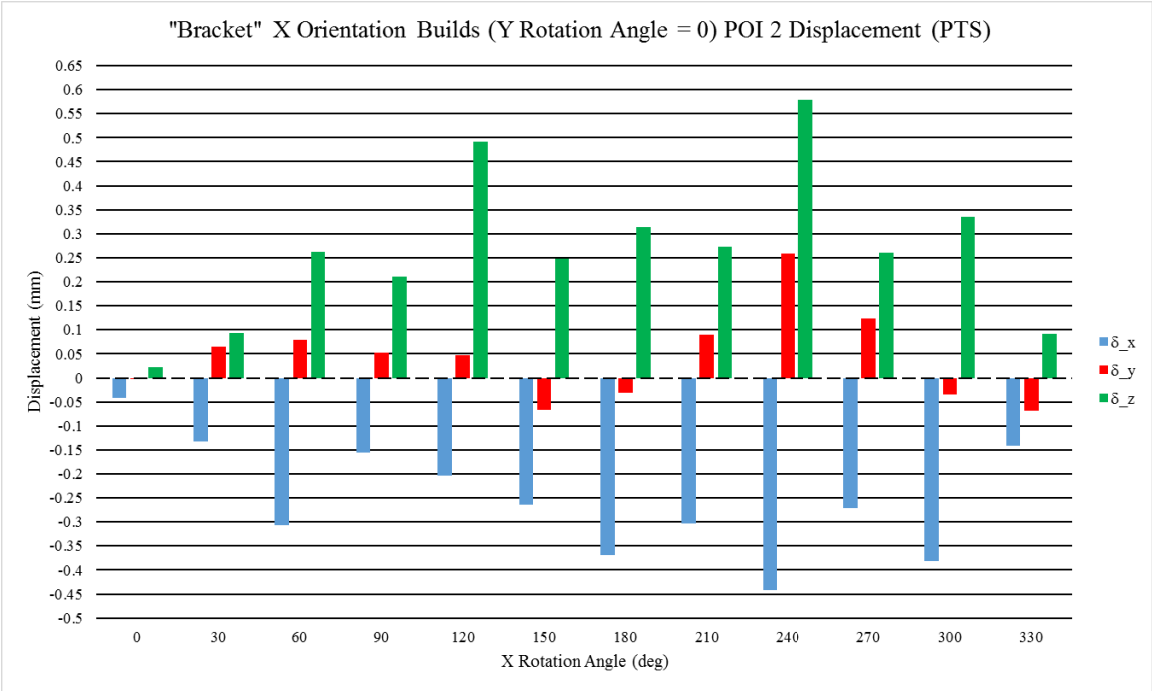

Figure 54: Directional displacement (PTS) plot for "Bracket" X Orientation Builds (POI 2)

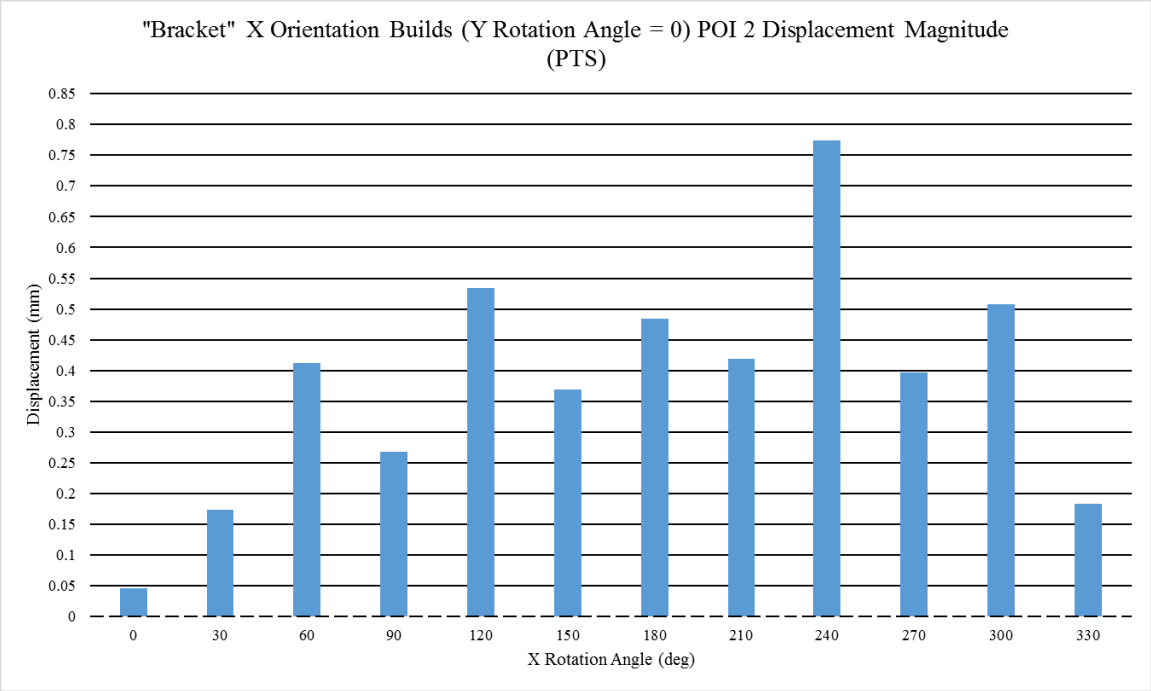

Figure 55: Displacement magnitude (PTS) plot for "Bracket" X Orientation Builds (POI 2)

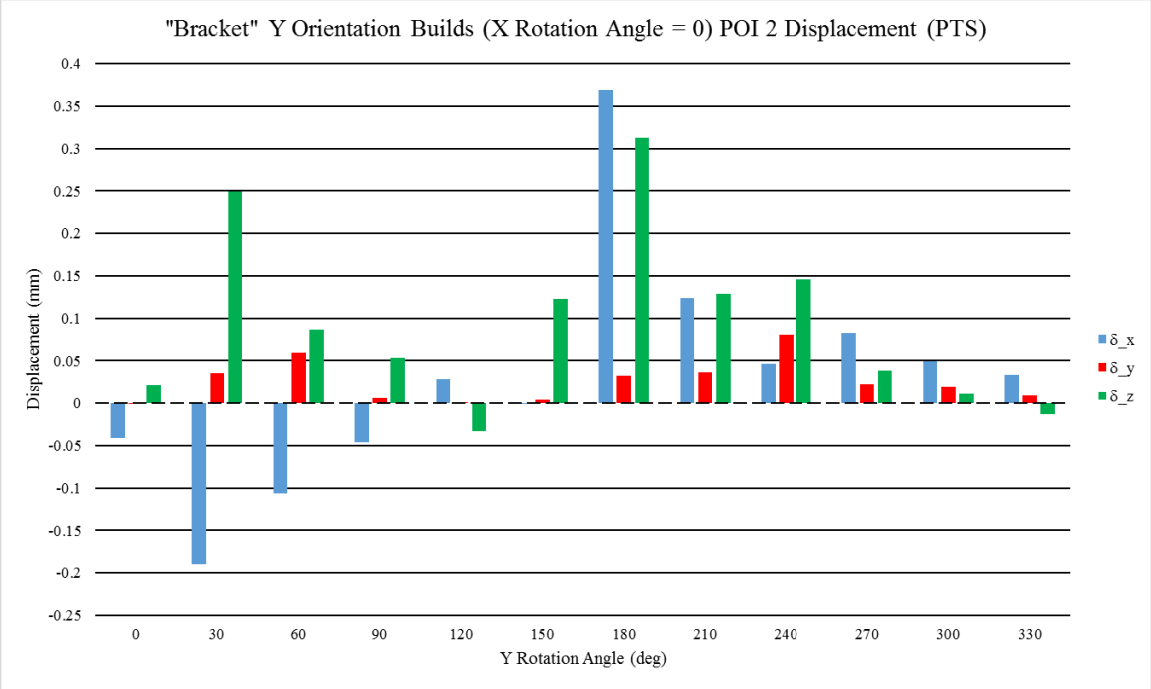

Figure 56: Directional displacement (PTS) plot for "Bracket" Y Orientation Builds (POI 2)

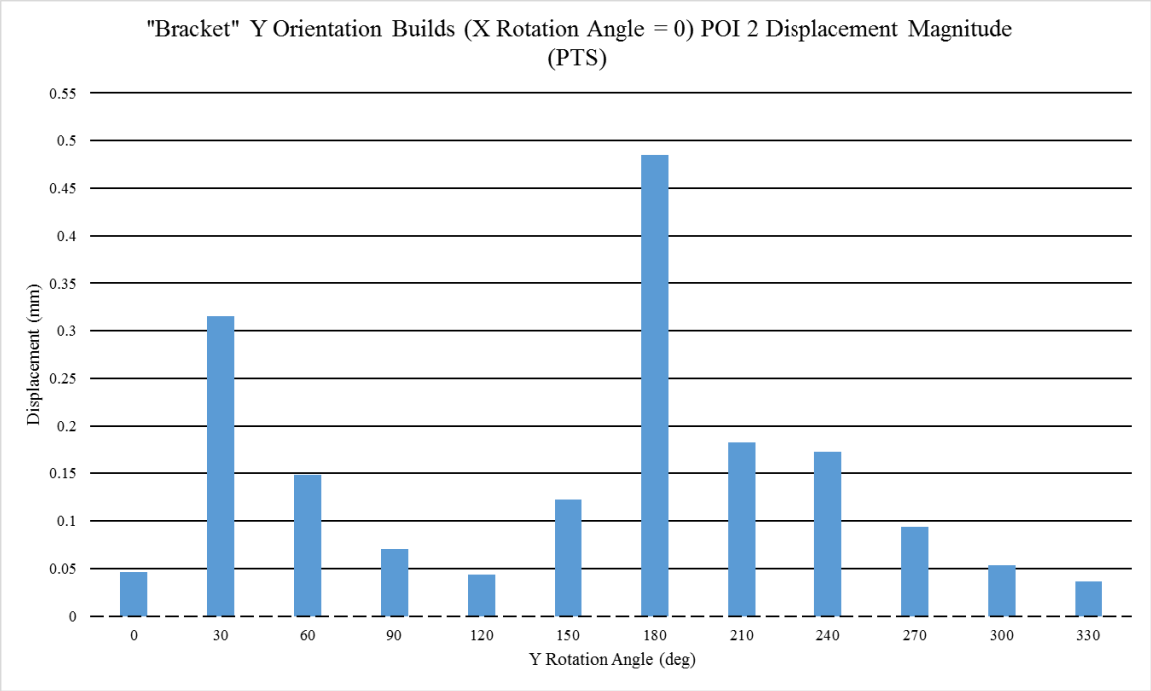

Figure 57: Displacement magnitude (PTS) plot for "Bracket" Y Orientation Builds (POI 2)

The PTS data at POI 3 for all the orientations of the "Bracket" part build are shown in Figure 60 through Figure 63: Figure 60 is the plot for the directional displacement data of the X orientation builds, Figure 61 is the plot for the displacement magnitude data of the X orientation builds, Figure 62 is the plot for the direction displacement data of the Y, and Figure 63 is the plot for the displacement magnitude data of the Y orientation builds. Based on the aforementioned plots, the following observations were made. First, the displacements at POI 3 were lower than POI 2 overall. Unlike POI 2, POI 3 is placed on the center lug which is thinner than the lug with POI 2. This result was unexpected, because the hypothesis was that the POIs on the thicker areas of the part would distort less, and so this observation indicates that as POI are placed closer to the center of the build the distortion decreases. Second, the worst orientation of the "Bracket" part orientation at POI 3 was X0Y300 with a displacement magnitude of 0.6370 mm. Unlike, the pervious 2 POIs distortions in all three primary axis contributed significantly. Similar to the max distortion orientations for POI 1 and 2, the relatively large distortion comes from the lack of support material underneath the point and unfavorable geometry (see Figure 58). Third, the best orientation of the "Bracket" part orientation at POI 3 was X30Y0 with a displacement magnitude of 0.01 mm. Similar to the other POIs, the minimum distortion can be attributed to the POI being well supported and the point being in an ideal location (see Figure 59). Fourth, the X rotations had less effect on the distortions at POI 3 than Y rotations did which is the exact opposite effect that was seen at POI 1 and 2. This could be from due to POI 3 being placed 2 mm away from the lug edge in the y-direction while the 2 mm offset from the lug edge was done in the x-direction for POI 1 and 2 (see Figure 32).

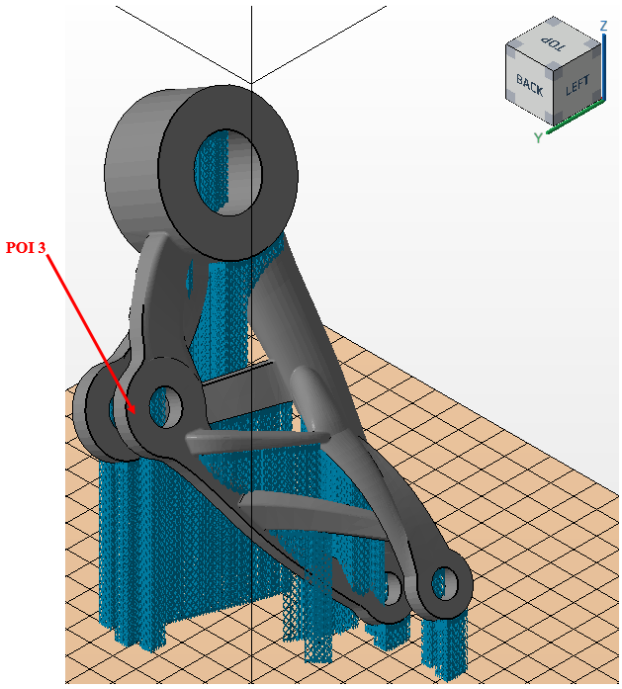

Figure 58: "Bracket" X0Y300 orientation showing the geometry and support structure around POI 3

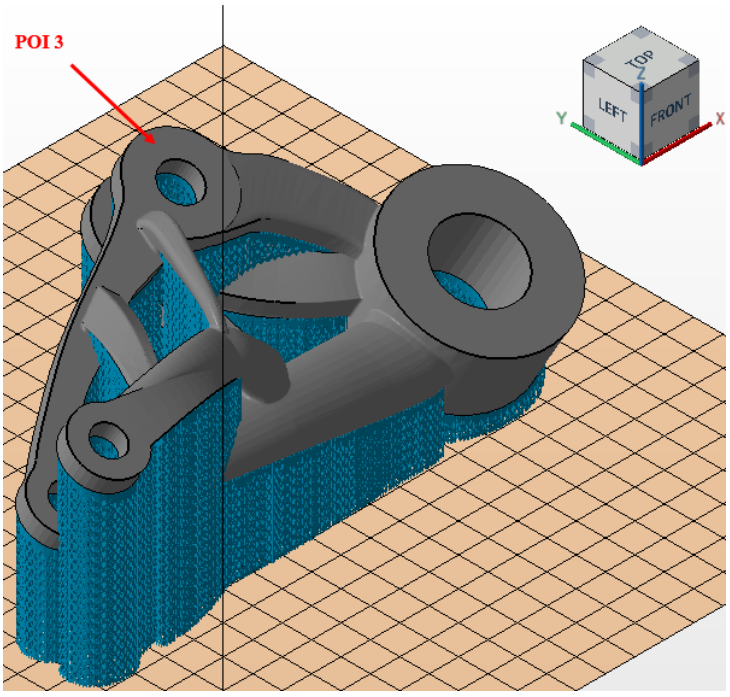

Figure 59: "Bracket" X30Y0 orientation showing the geometry and support structure around POI 3

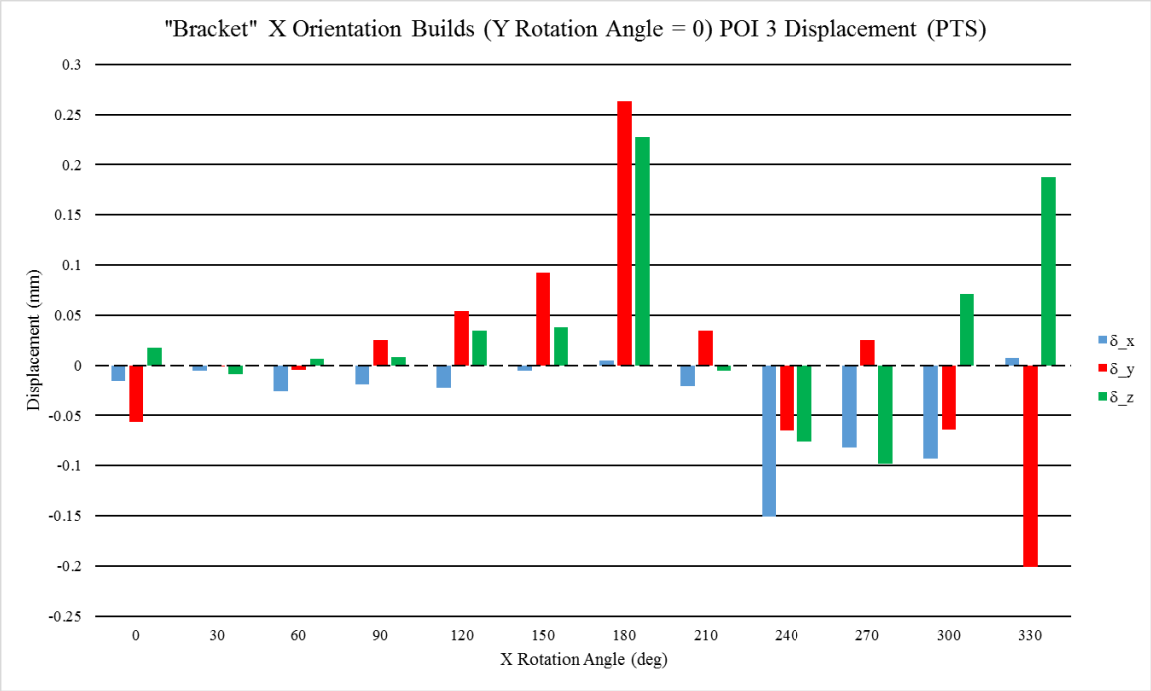

Figure 60: Directional displacement (PTS) plot for "Bracket" X Orientation Builds (POI 3)

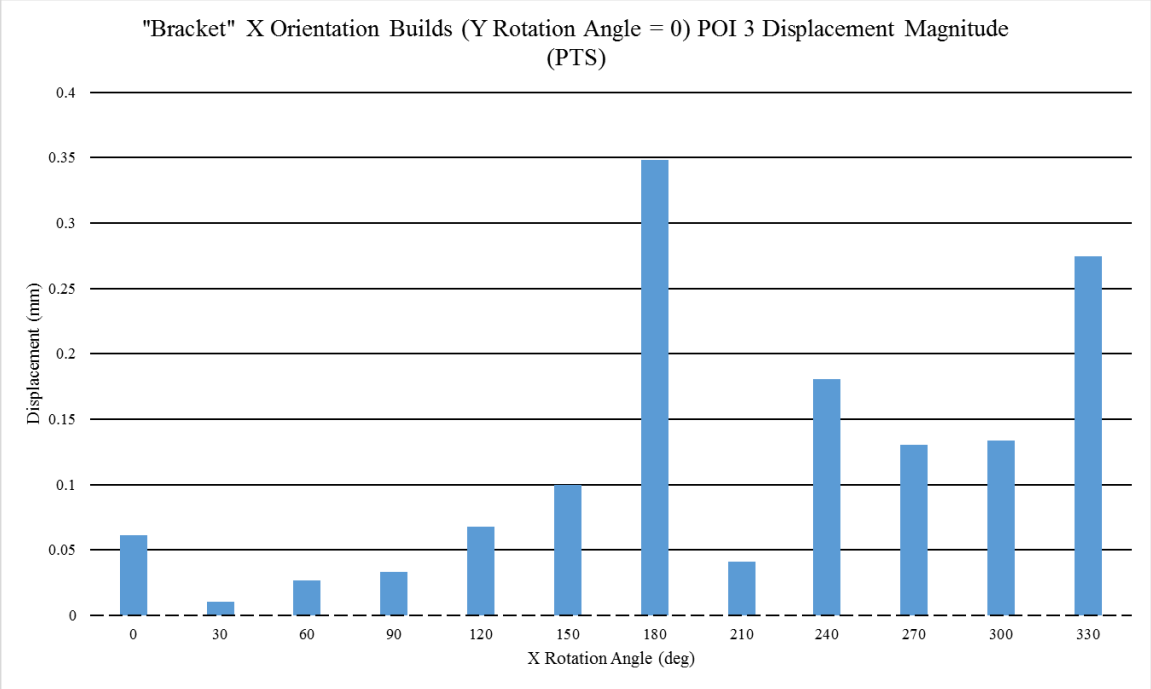

Figure 61: Displacement magnitude (PTS) plot for "Bracket" X Orientation Builds (POI 3)

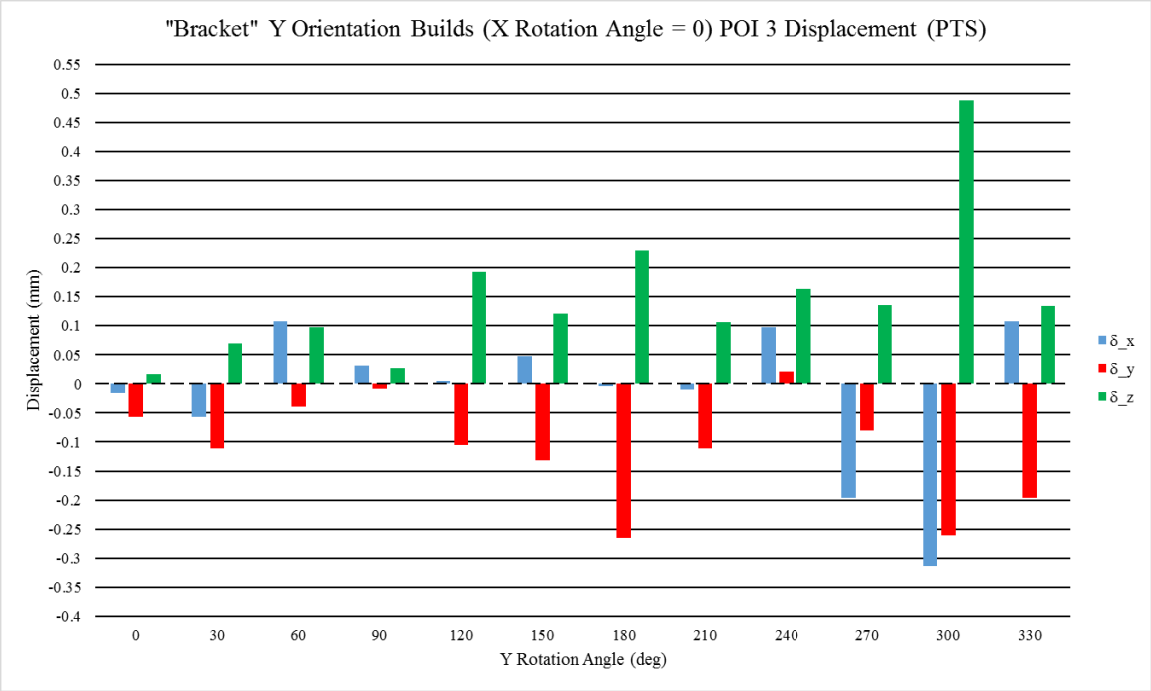

Figure 62: Directional displacement (PTS) plot for "Bracket" Y Orientation Builds (POI 3)

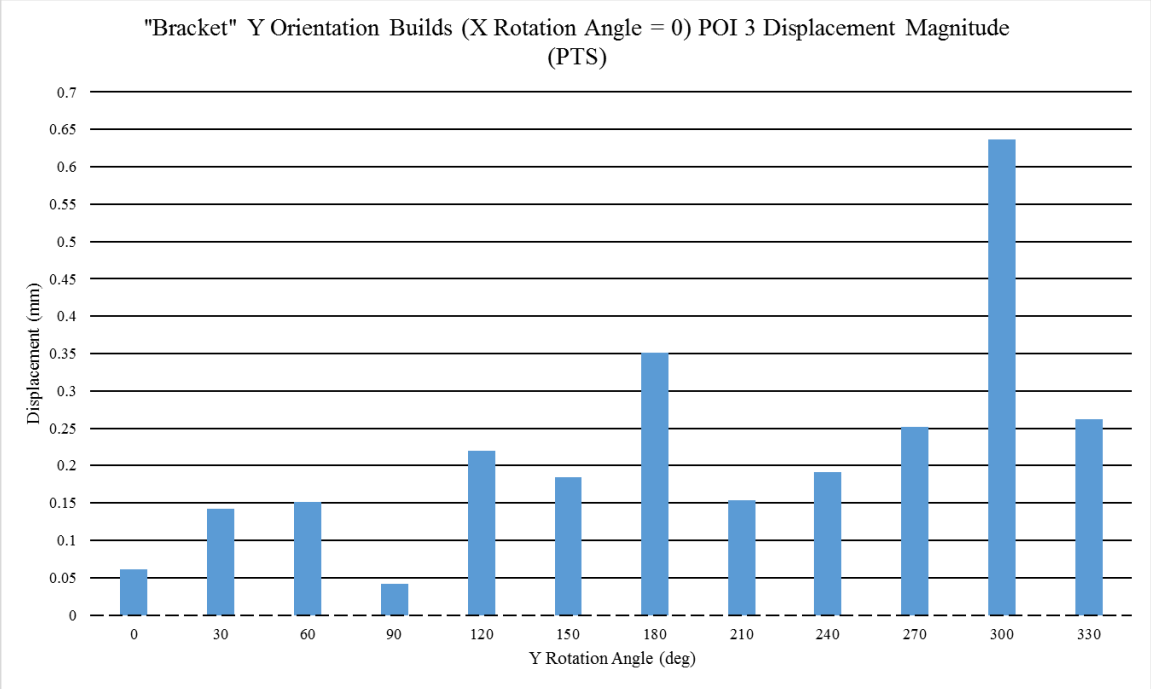

Figure 63: Displacement magnitude (PTS) plot for "Bracket" Y Orientation Builds (POI 3)

The PTS data at POI 4 for all the orientations of the “Bracket” part build are shown in Figure 65 through Figure 68: Figure 65 is the plot for the directional displacement data of the X orientation builds, Figure 66 is the plot for the displacement magnitude data of the

X orientation builds, Figure 67 is the plot for the direction displacement data of the Y, and Figure 68 is the plot for the displacement magnitude data of the Y orientation builds. Based on the aforementioned plots, the following observations were made. First, POI 4 the smallest range of displacements and had lest least amount of distortions across the orientations of all the POIs. POI 4 was toward the center of the build which was similar to POI 3 meaning that POI 4 validates the distortion phenomena discussed for POI 3 regarding the center of the part (see Figure 32). In addition, POI 4 was surrounded by to two branching columns which restricts the distortion in the area between the columns (see Figure 32). Second, the worst orientation of the "Bracket" part orientation at POI 4 was X0Y300 with a displacement magnitude of 0.3162 mm. In addition, the largest contributor to the displacement magnitude in the X0Y300 at POI 4 is the displacement in the y-direction with a value of 0.2530 mm. A cause for the high distortion at POI 4 at this orientation is that there is no support underneath the point as shown in Figure 64. Third, the best orientation of the "Bracket" part orientation at POI 4 was X240Y0 with a displacement magnitude of 0.0262 mm.

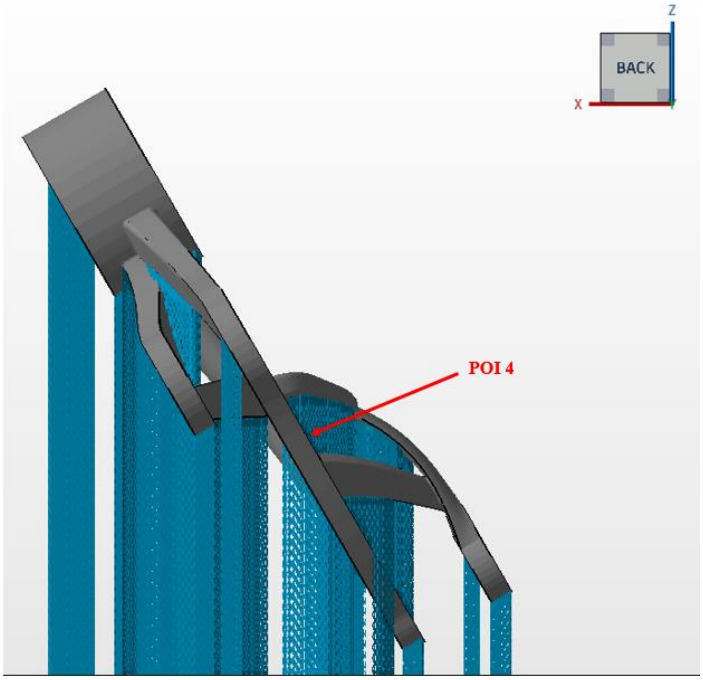

Figure 64: "Bracket" X0Y300 orientation showing the geometry and support structure around POI 4

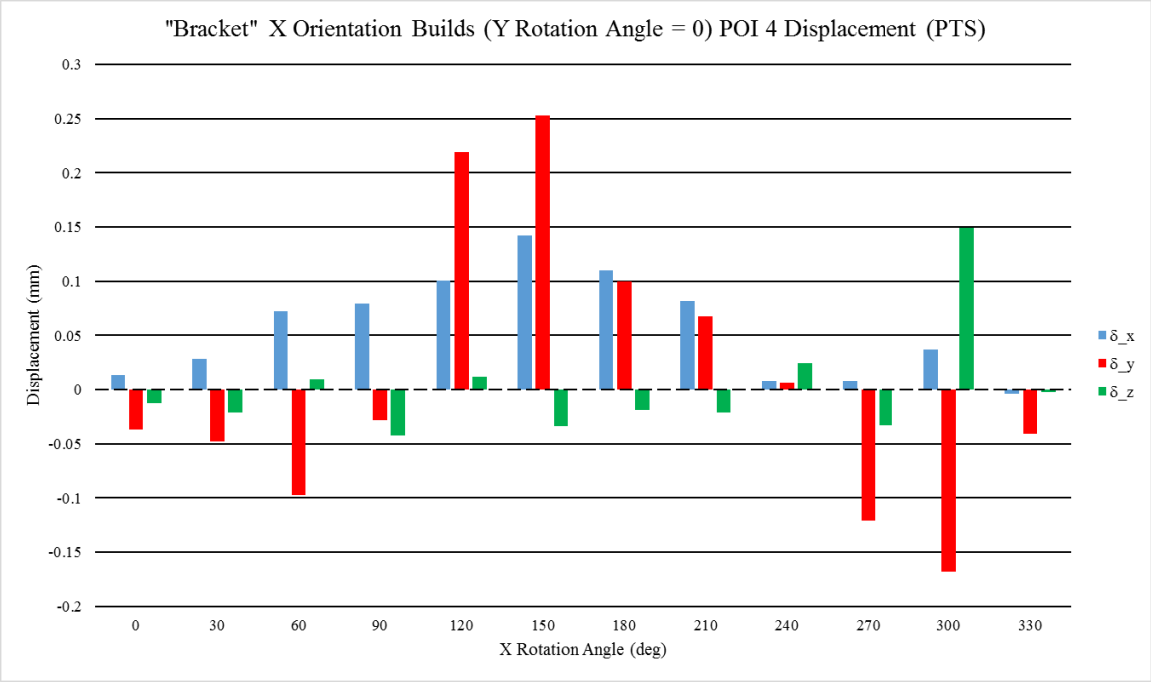

Figure 65: Directional displacement (PTS) plot for "Bracket" X Orientation Builds (POI 4)

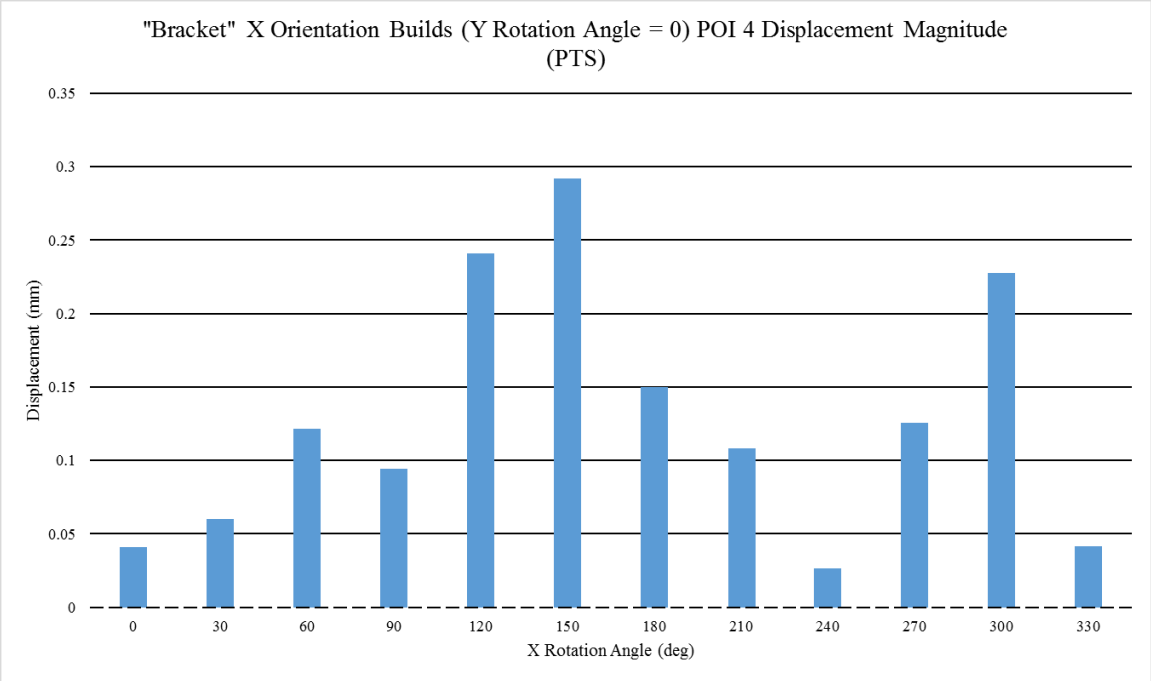

Figure 66: Displacement magnitude (PTS) plot for "Bracket" X Orientation Builds (POI 4)

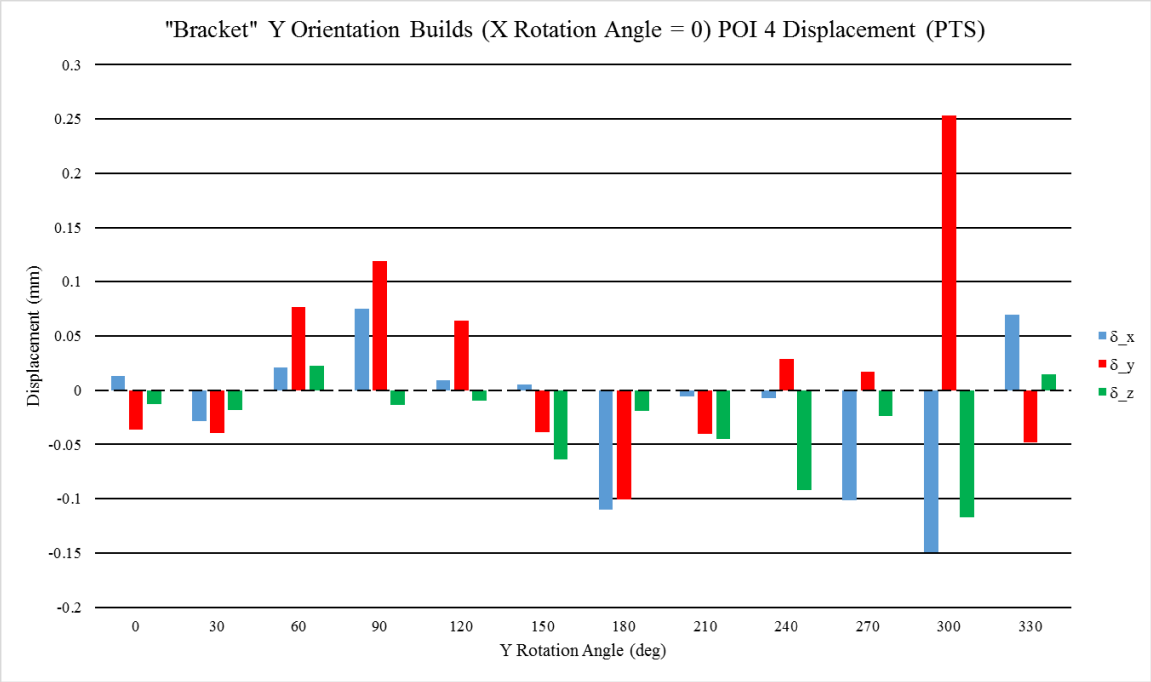

Figure 67: Directional displacement (PTS) plot for "Bracket" Y Orientation Builds (POI 4)

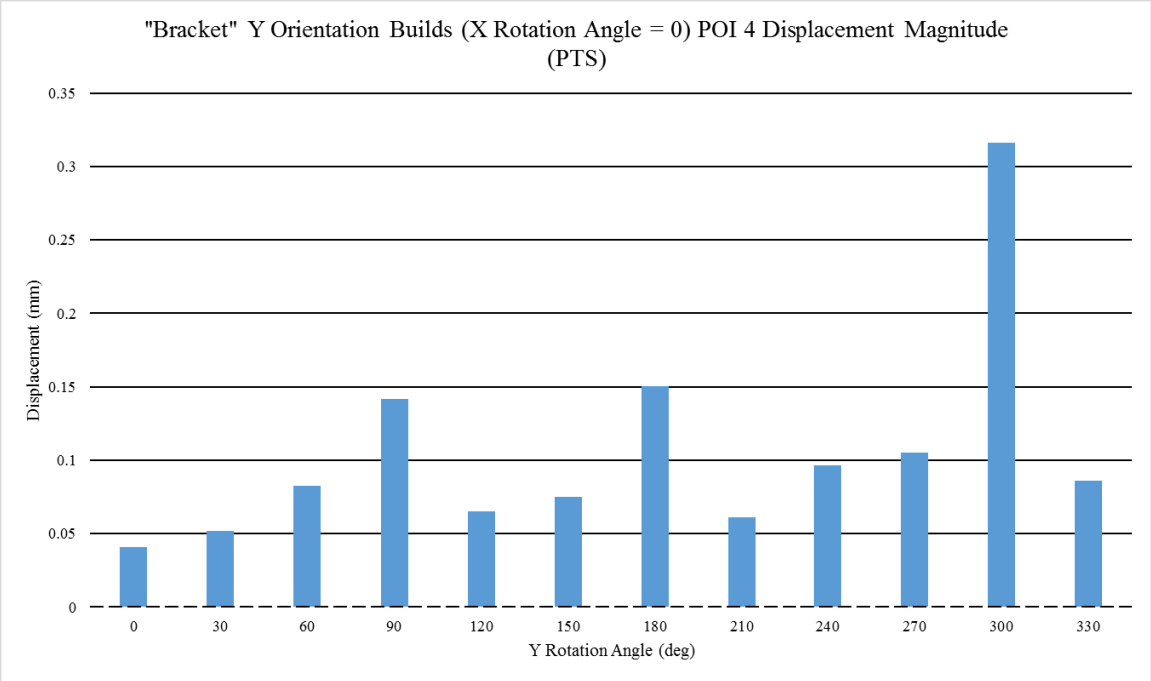

Figure 68: Displacement magnitude (PTS) plot for "Bracket" Y Orientation Builds (POI 4)

In order to determine the best orientation for the entire “Bracket” part in terms of displacement at the PTS, the following procedure was used. First, the best orientations for each POI on the “Bracket” part was found. A summary of the best orientations for each

POI on the “Bracket” part is found in Table 32. Second, for each orientation found in the previous step the displacement magnitudes of all 4 POIs were averaged, the result is shown in Table 33. Third, the minimum of the displacement magnitudes found in step two was taken as the best orientation of the entire “Bracket” part in terms of PTS displacement, and that orientation was X30Y0.

Table 32: Summary of best orientation form each "Bracket" part POI (PTS displacement)

POI #	Best Orientation	Disp Mag (mm)
1	X0Y270	0.0117
2	X0Y330	0.0367
3	X30Y0	0.0100
4	X240Y0	0.0262

Table 33: Displacement magnitudes averages at each best orientation (PTS displacement)

Best Orientation	Avg Disp Mag (mm)
X0Y270	0.1155
X0Y330	0.1475
X30Y0	0.0952
X240Y0	0.4061

3.1.2: Displacement Results: SRTS

The SRTS displacement results are shown in Figure 69 though Figure 88. The SRTS results for the first test build are shown in Figure 69, and Figure 70. Figure 69 is the plot for the directional displacement data, and Figure 70, is the plot for the displacement magnitude. The following observation were made from the data The distortion magnitudes were higher off the build plate than on, however the distortions were still very small compared to part size. This is due to the supports having a high enough volume that it still resists distortion even when removed from the plate. In addition, these small distortions were the reason they were omitted from being measured.

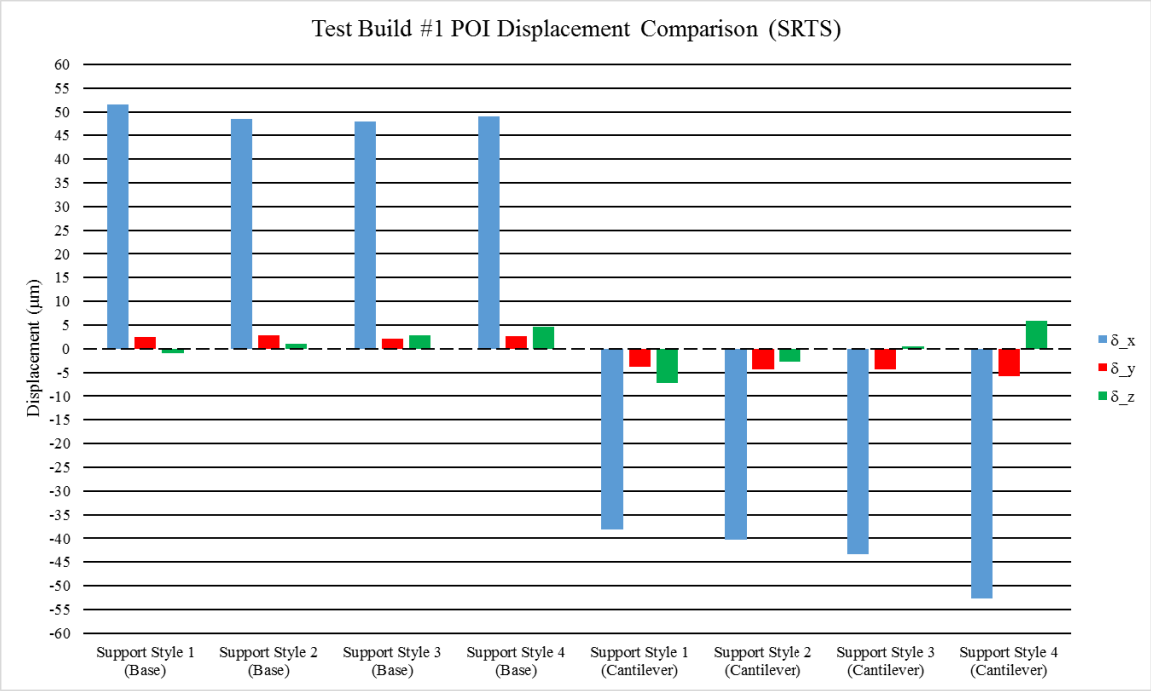

Figure 69: Directional displacement (SRTS) plot for Test Build #1

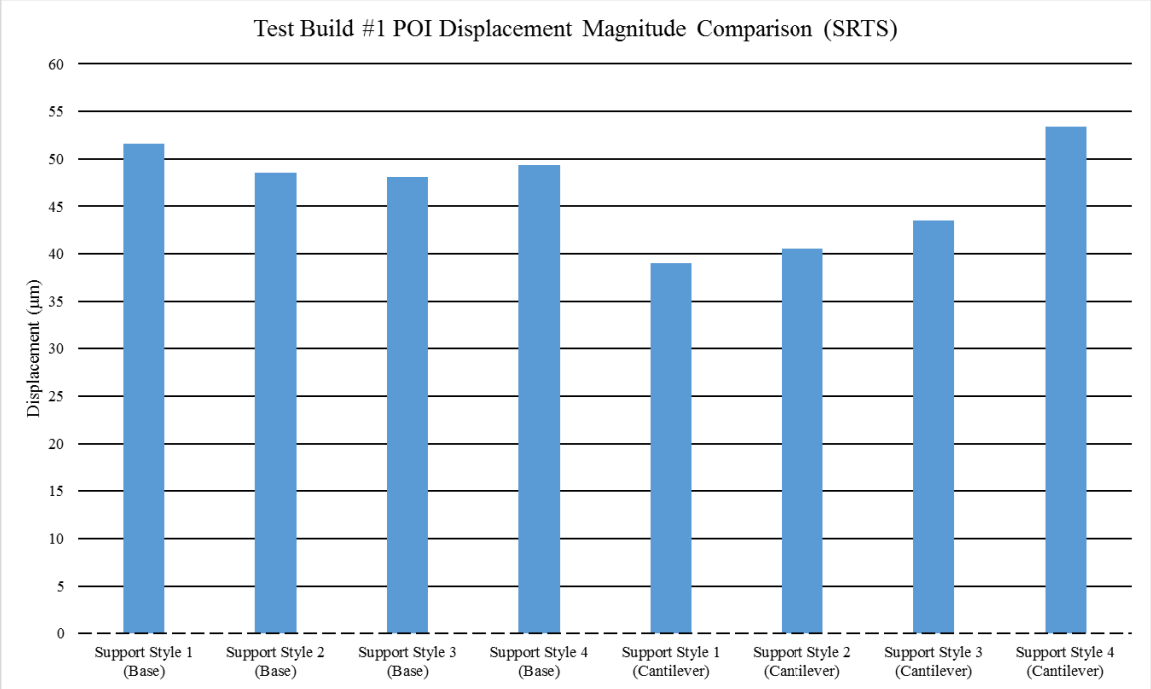

Figure 70: Displacement magnitude (SRTS) plot for Test Build #1

The SRTS results for the second test build are shown in Figure 71, and Figure 72. Figure 71 is the plot for the directional displacement data, and Figure 72, is the plot for the displacement magnitude. The following observations were made from the data. First, like

the first test build the distortion increased when the build plate was removed, however the increase was far more significant. This indicates that the supports restricted distortion at lot less in the second test build. Second, the POI's in Test Build #2 distorted more significantly in the z-direction, and this contrasts the behavior when the builds was on the plate. This caused by the plate holding the parts down to the plate during printing process.

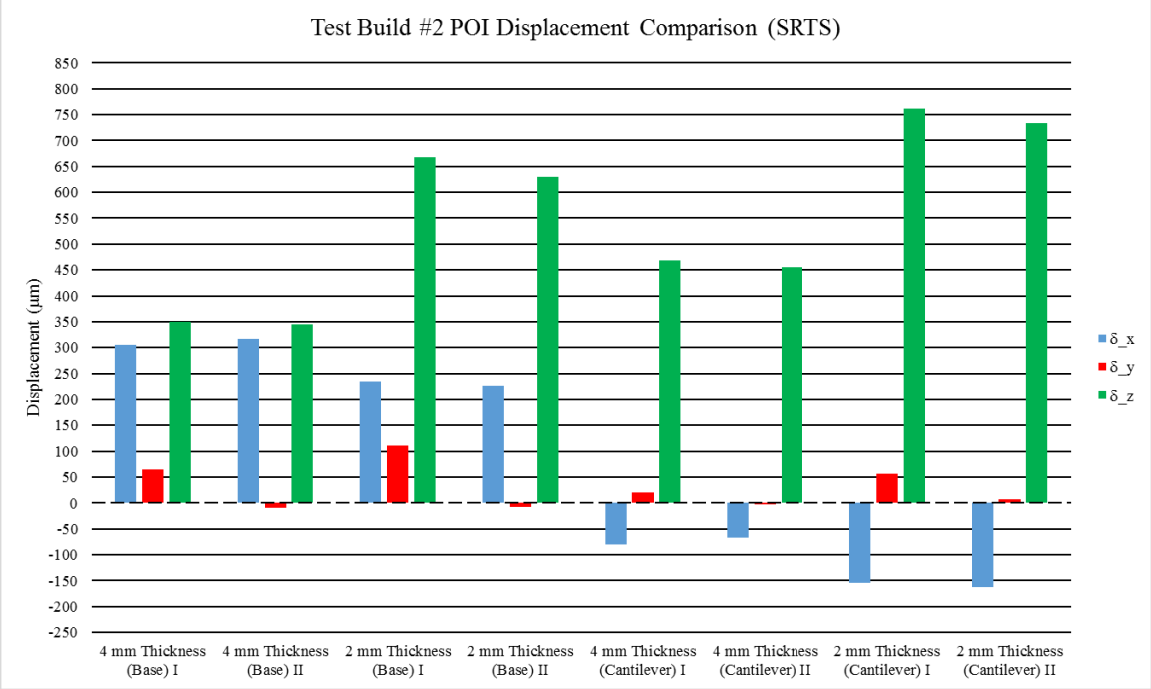

Figure 71: Directional displacement (SRTS) plot for Test Build #2

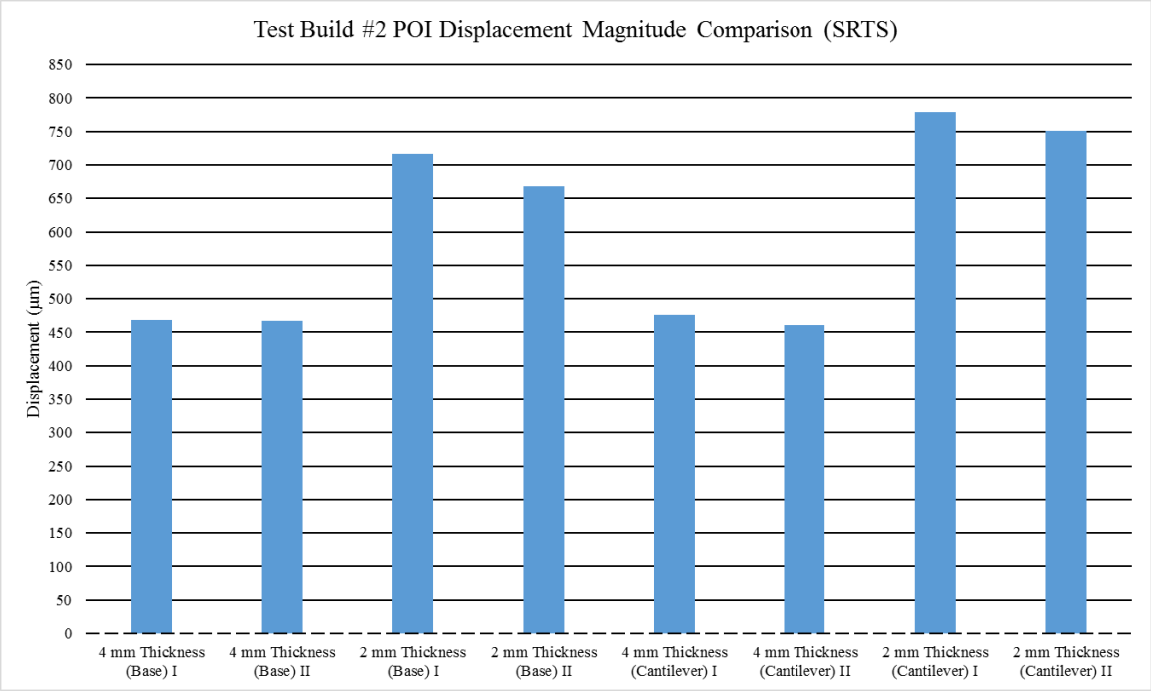

Figure 72: Displacement magnitude (SRTS) plot for Test Build #2

The SRTS data at POI 1 for all the orientations of the "Bracket" part build are shown in Figure 73 through Figure 76: Figure 73 is the plot for the directional displacement data of the X orientation builds, Figure 74 is the plot for the displacement magnitude data of the X orientation builds, Figure 75 is the plot for the direction displacement data of the Y, and Figure 76 is the plot for the displacement magnitude data of the Y orientation builds. Based on the aforementioned plots, the following observations were made. First, the worst orientation of the "Bracket" part at POI 1 was X0Y300 with a displacement magnitude of 1.529 mm. The majority of distortion at POI 1 in the X0Y300 orientation was in the x and z direction, while there was very little distortion in the y-direction. Second, the best orientation of the "Bracket" part at POI 1 was X0Y60 with a displacement magnitude of 0.0954 mm. Third, the displacement magnitudes have increased from the PTS to the SRTS.

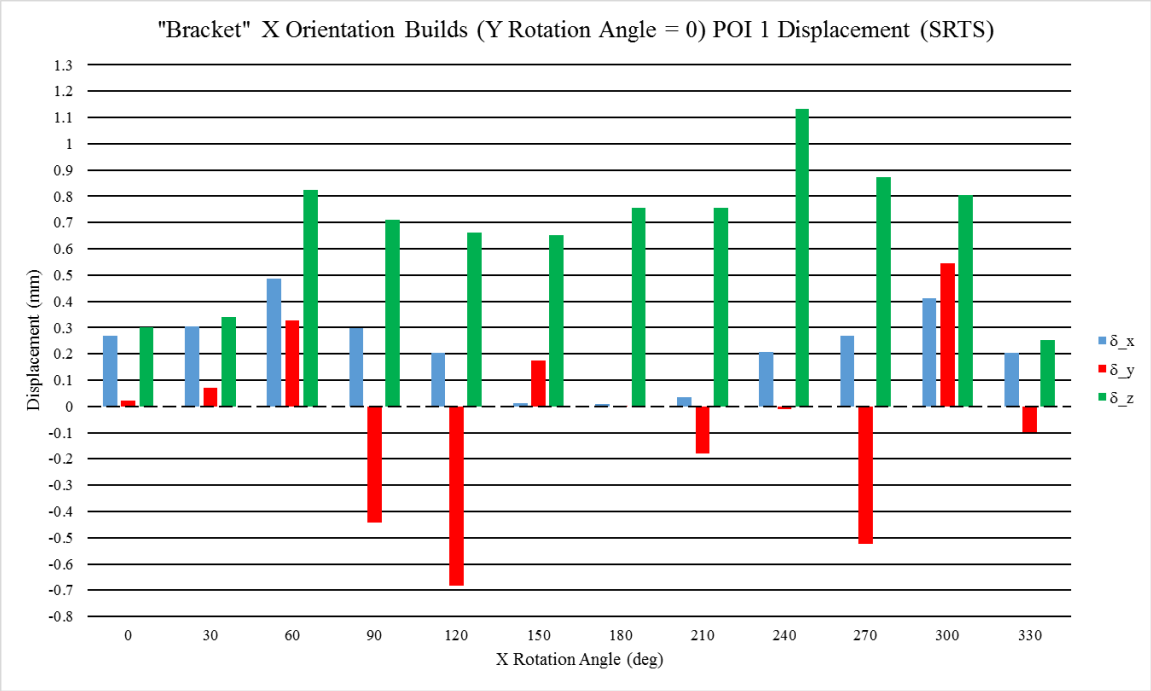

Figure 73: Directional displacement (SRTS) plot for "Bracket" X Orientation Builds (POI 1)

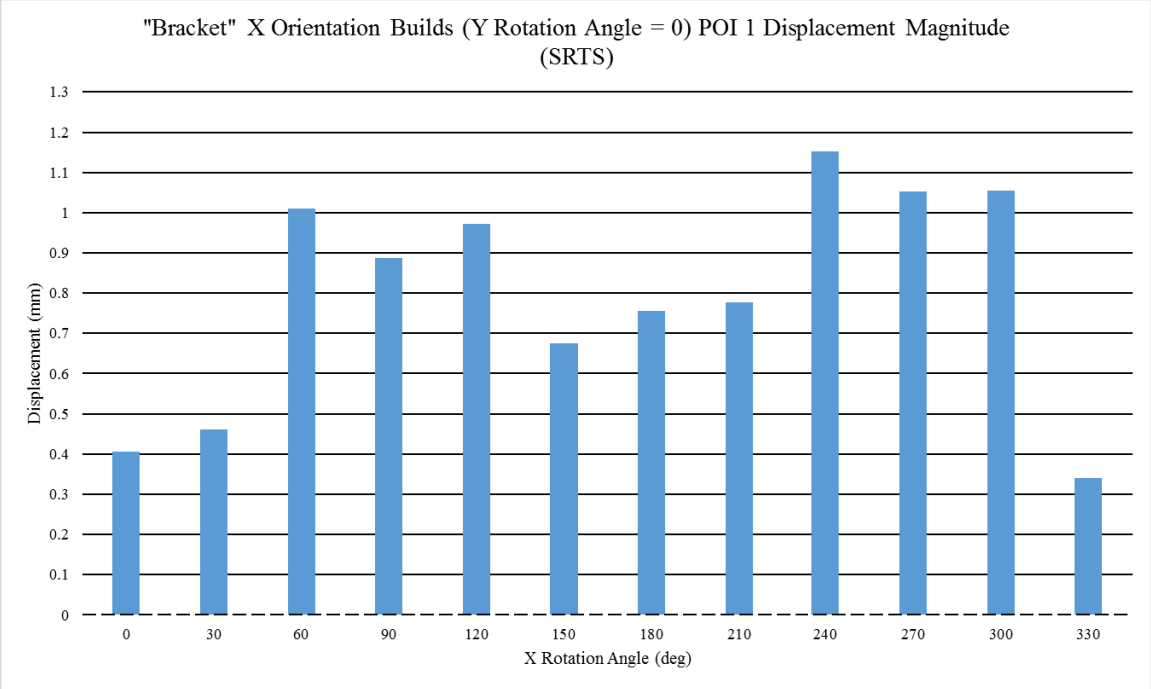

Figure 74: Displacement magnitude (SRTS) plot for "Bracket" X Orientation Builds (POI 1)

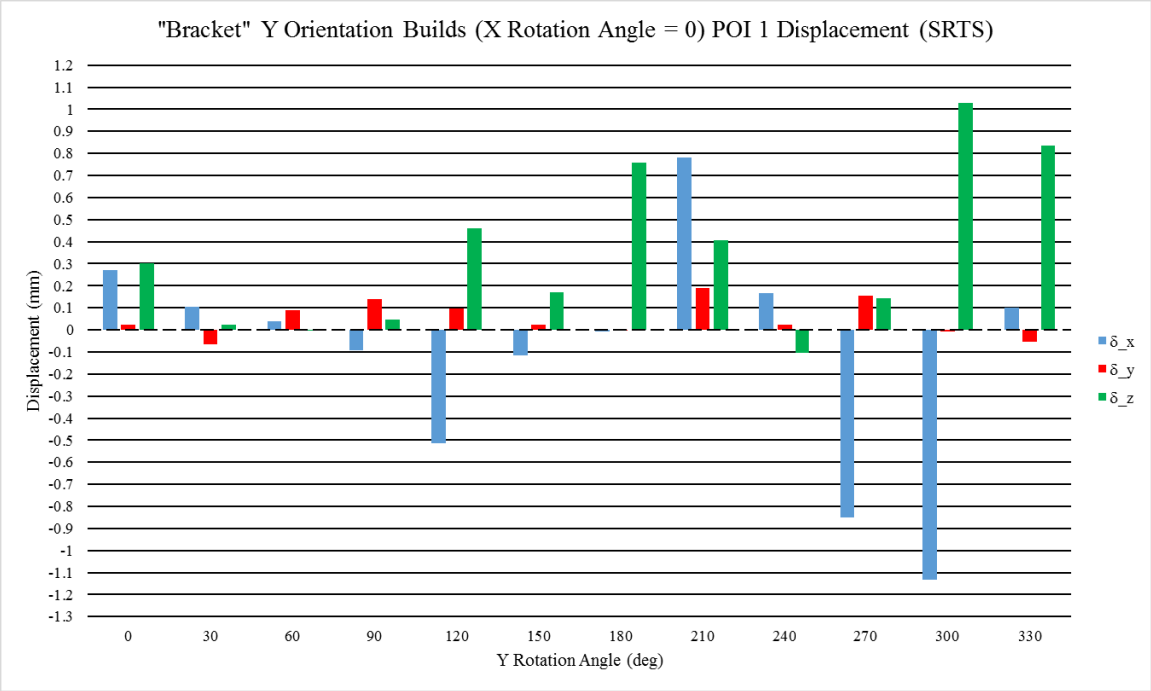

Figure 75: Directional displacement (SRTS) plot for "Bracket" Y Orientation Builds (POI 1)

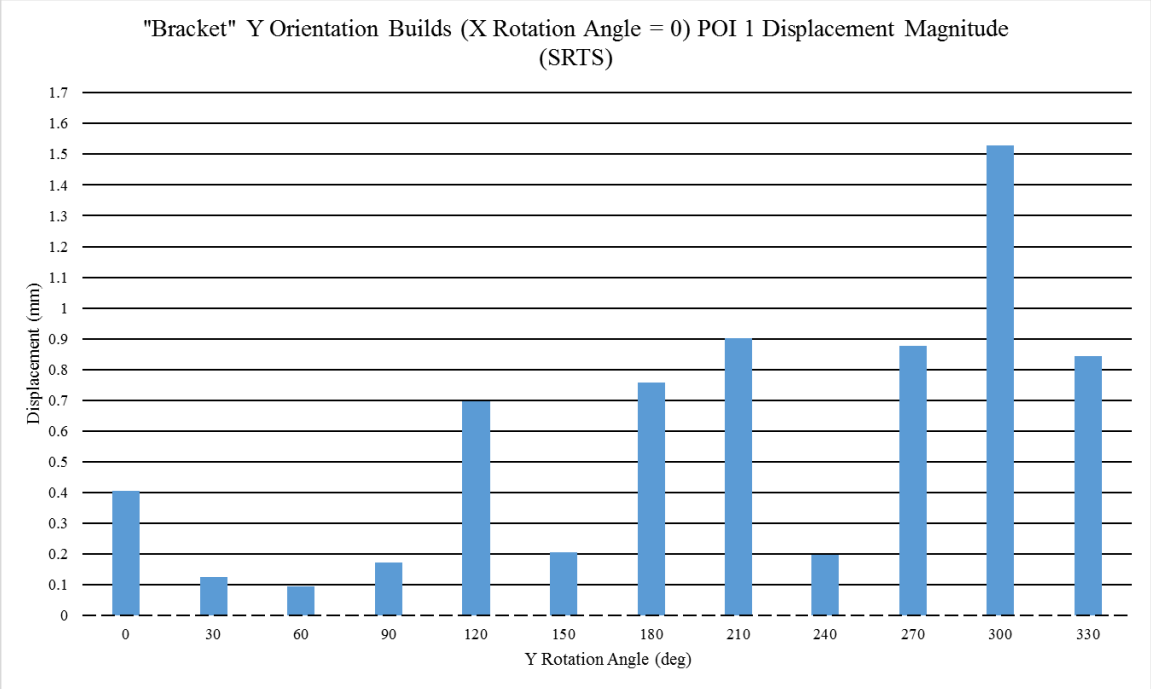

Figure 76: Displacement magnitude (SRTS) plot for "Bracket" Y Orientation Builds (POI 1)

The SRTS data at POI 2 for all the orientations of the "Bracket" part build are shown in Figure 77 through Figure 80: Figure 77 is the plot for the directional displacement data of the X orientation builds, Figure 78 is the plot for the displacement magnitude data

of the X orientation builds, Figure 79 is the plot for the direction displacement data of the Y, and Figure 80 is the plot for the displacement magnitude data of the Y orientation builds. Based on the aforementioned plots, the following observations were made. First, the worst orientation of the "Bracket" part orientation at POI 2 was X240Y0 with a displacement magnitude of 0.8635 mm. The majority of distortion at POI 2 in the X240Y0 orientation was in the z direction. Second, the best orientation of the "Bracket" part at POI 2 was X0Y270 with a displacement magnitude of 0.0412 mm.

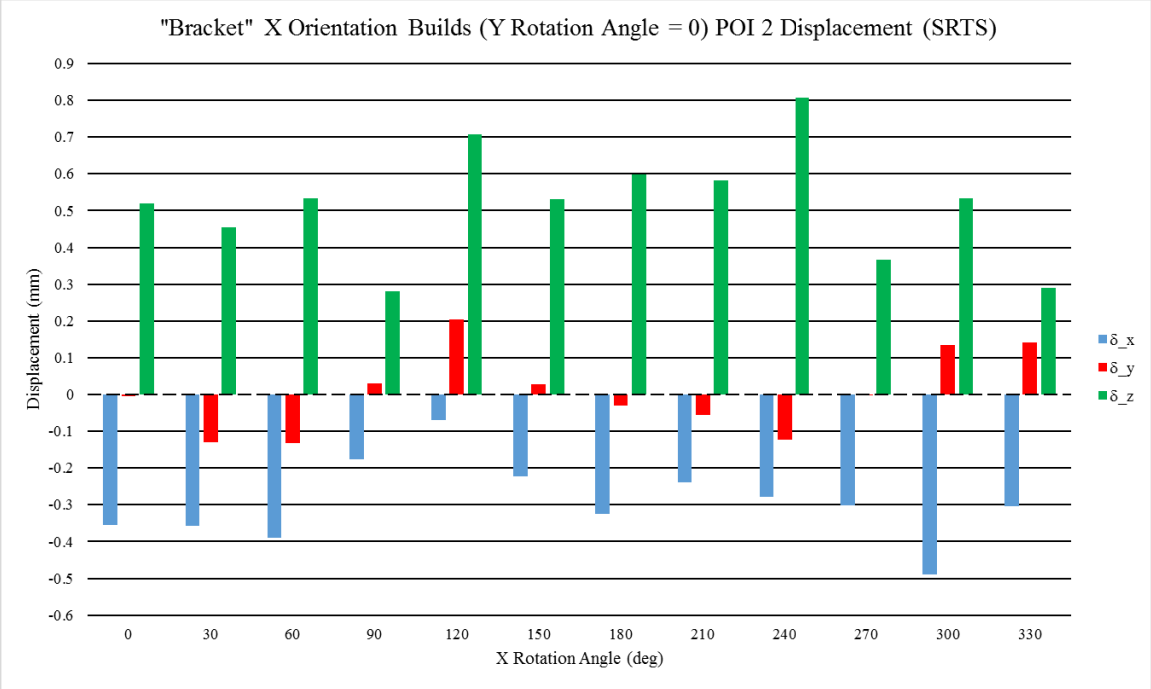

Figure 77: Directional displacement (SRTS) plot for "Bracket" X Orientation Builds (POI 2)

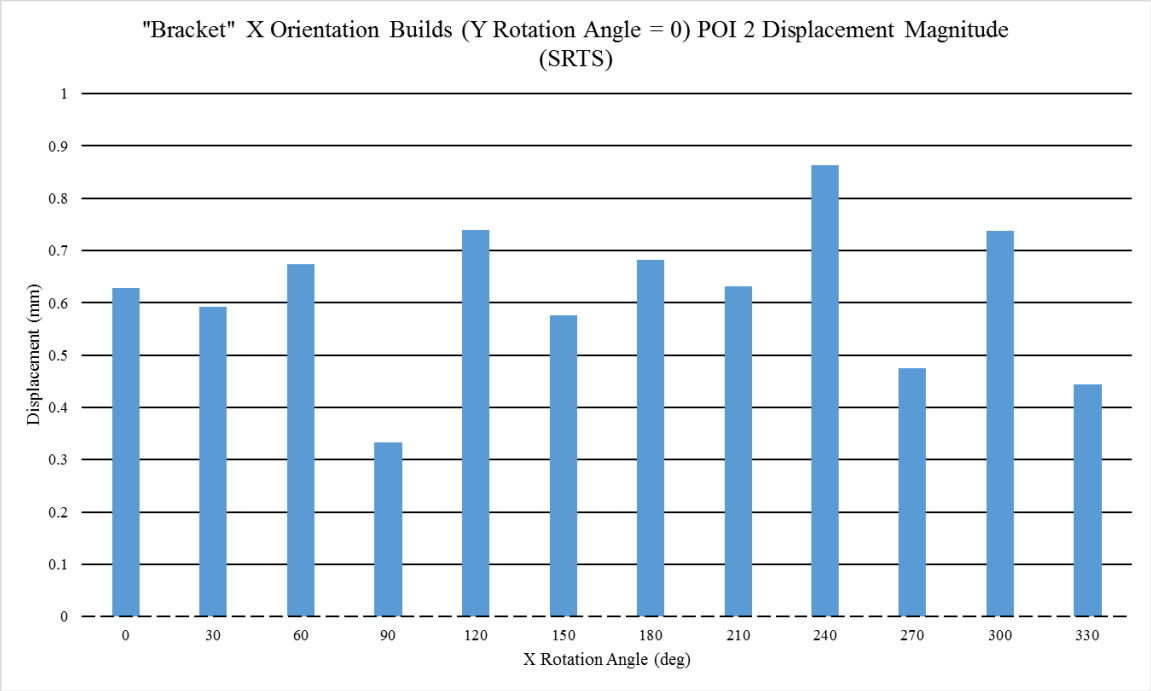

Figure 78: Displacement magnitude (SRTS) plot for "Bracket" X Orientation Builds (POI 2)

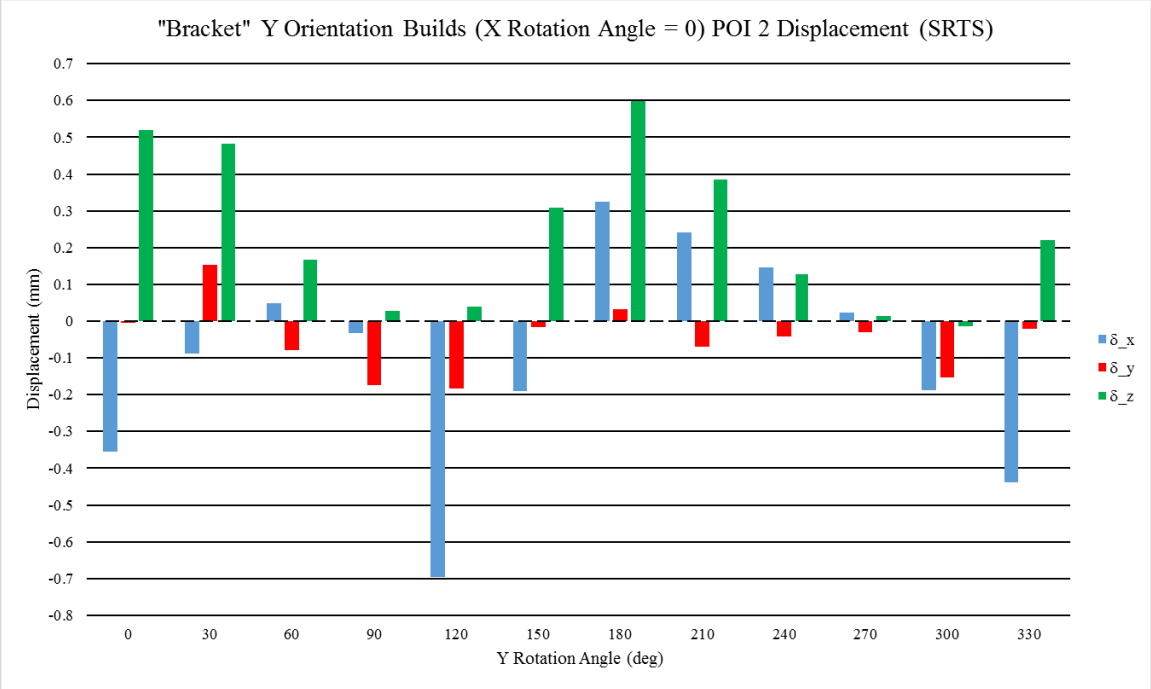

Figure 79: Directional displacement (SRTS) plot for "Bracket" Y Orientation Builds (POI 2)

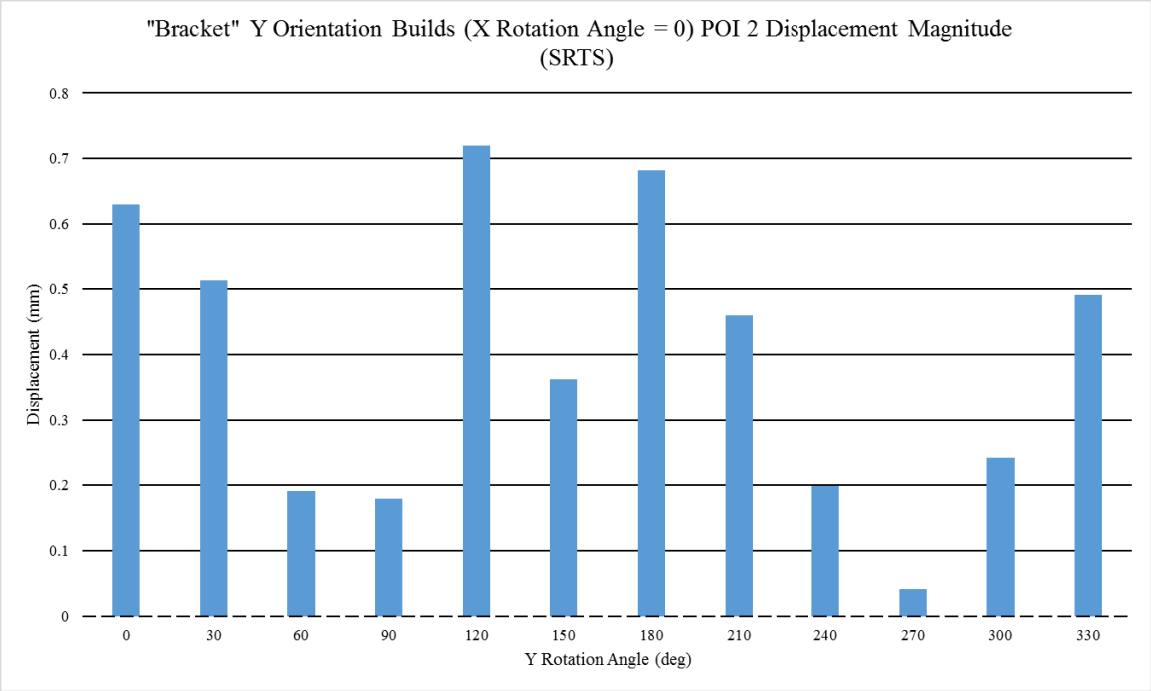

Figure 80: Displacement magnitude (SRTS) plot for "Bracket" Y Orientation Builds (POI 2)

The SRTS data at POI 3 for all the orientations of the "Bracket" part build are shown in Figure 81 through Figure 84: Figure 81 is the plot for the directional displacement data of the X orientation builds, Figure 82 is the plot for the displacement magnitude data of the X orientation builds, Figure 83 is the plot for the direction displacement data of the Y, and Figure 84 is the plot for the displacement magnitude data of the Y orientation builds. Based on the aforementioned plots, the following observations were made. First, the worst orientation of the "Bracket" part orientation at POI 3 was X0Y300 with a displacement magnitude of 0.6649 mm. The distortion at POI 3 in the X0Y300 orientation was nearly equal in all three Cartesian directions. Second, the best orientation of the "Bracket" part at POI 3 was X30Y0 with a displacement magnitude of 0.0359 mm.

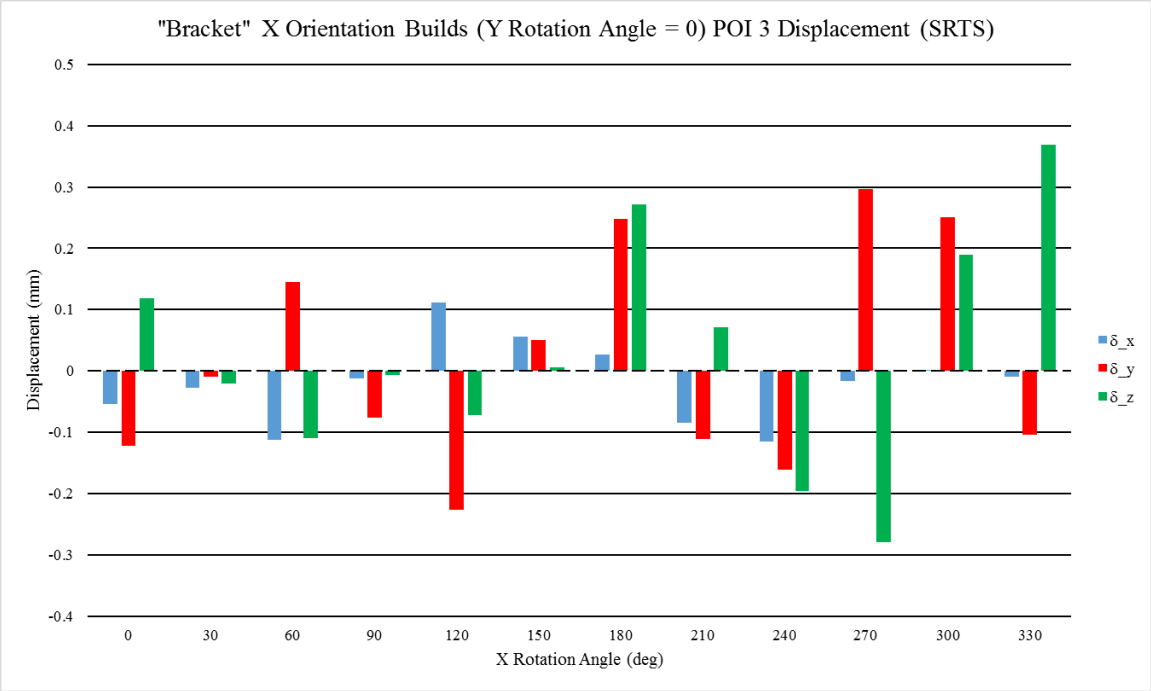

Figure 81: Directional displacement (SRTS) plot for "Bracket" X Orientation Builds (POI 3)

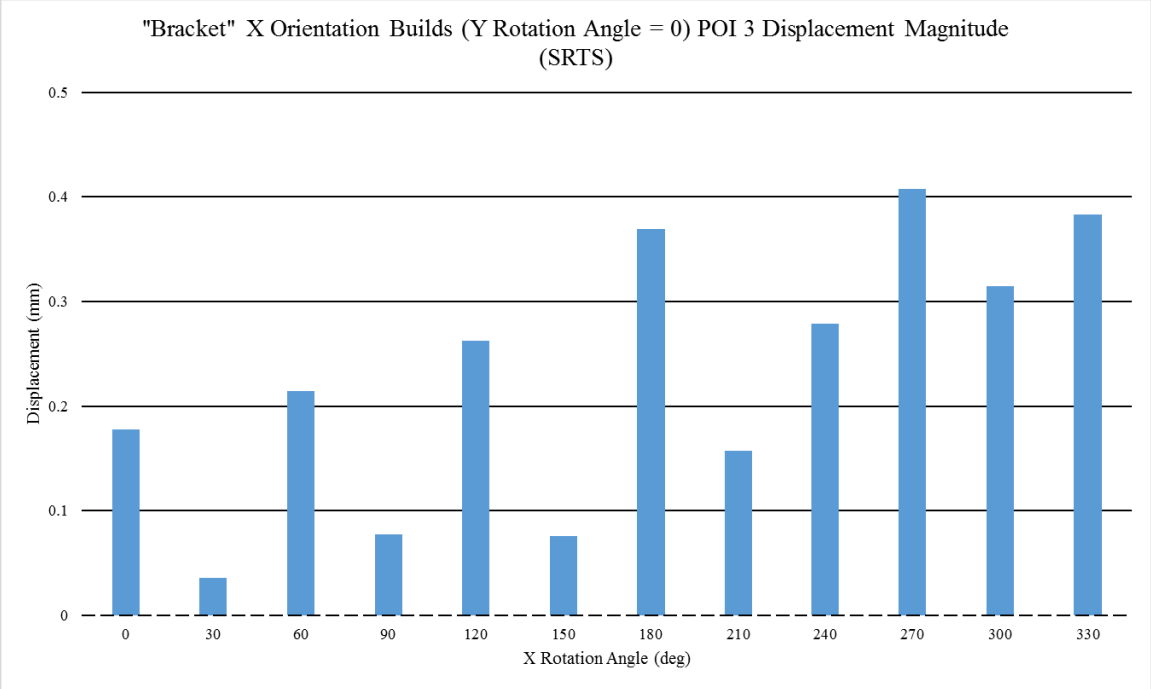

Figure 82: Displacement magnitude (SRTS) plot for "Bracket" X Orientation Builds (POI 3)

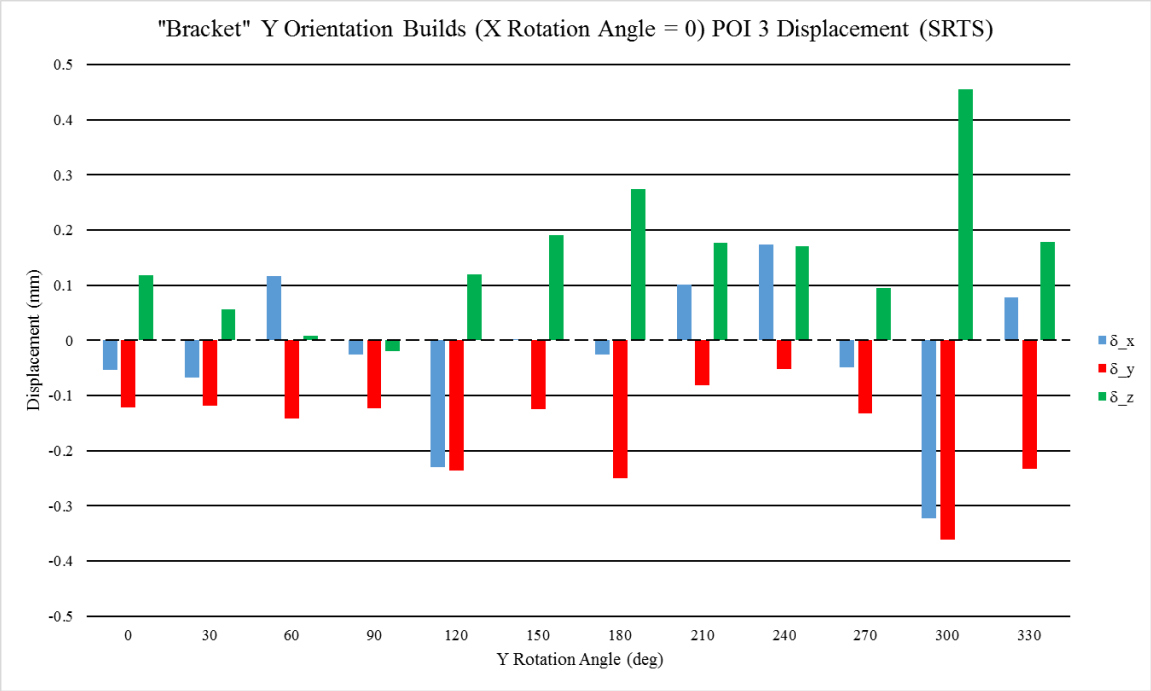

Figure 83: Directional displacement (SRTS) plot for "Bracket" Y Orientation Builds (POI 3)

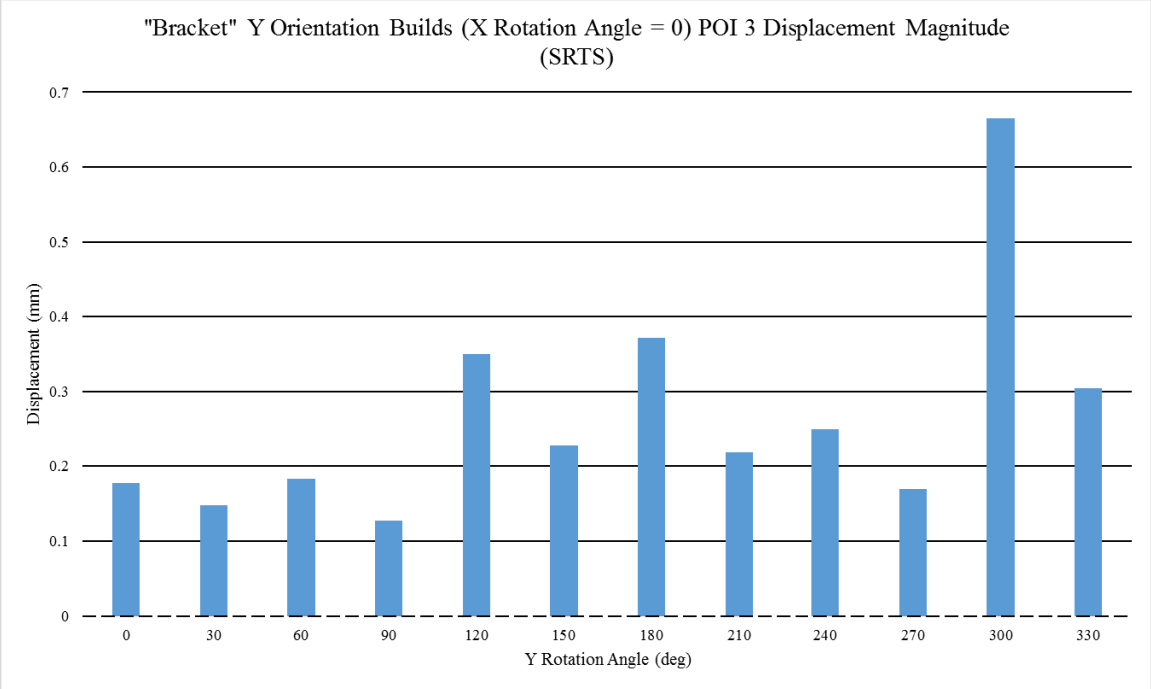

Figure 84: Displacement magnitude (SRTS) plot for "Bracket" Y Orientation Builds (POI 3)

The SRTS data at POI 4 for all the orientations of the "Bracket" part build are shown in Figure 85 through Figure 88: Figure 85 is the plot for the directional displacement data of the X orientation builds, Figure 86 is the plot for the displacement magnitude data

of the X orientation builds, Figure 87 is the plot for the direction displacement data of the Y, and Figure 88 is the plot for the displacement magnitude data of the Y orientation builds. Based on the aforementioned plots, the following observations were made. First, the worst orientation of the "Bracket" part orientation at POI 4 was X0Y300 with a displacement magnitude of 0.3392 mm. The majority of distortion at POI 4 in the X0Y300 orientation was in the x and y direction. Second, the best orientation of the "Bracket" part at POI 4 was X30Y0 with a displacement magnitude of 0.0673 mm.

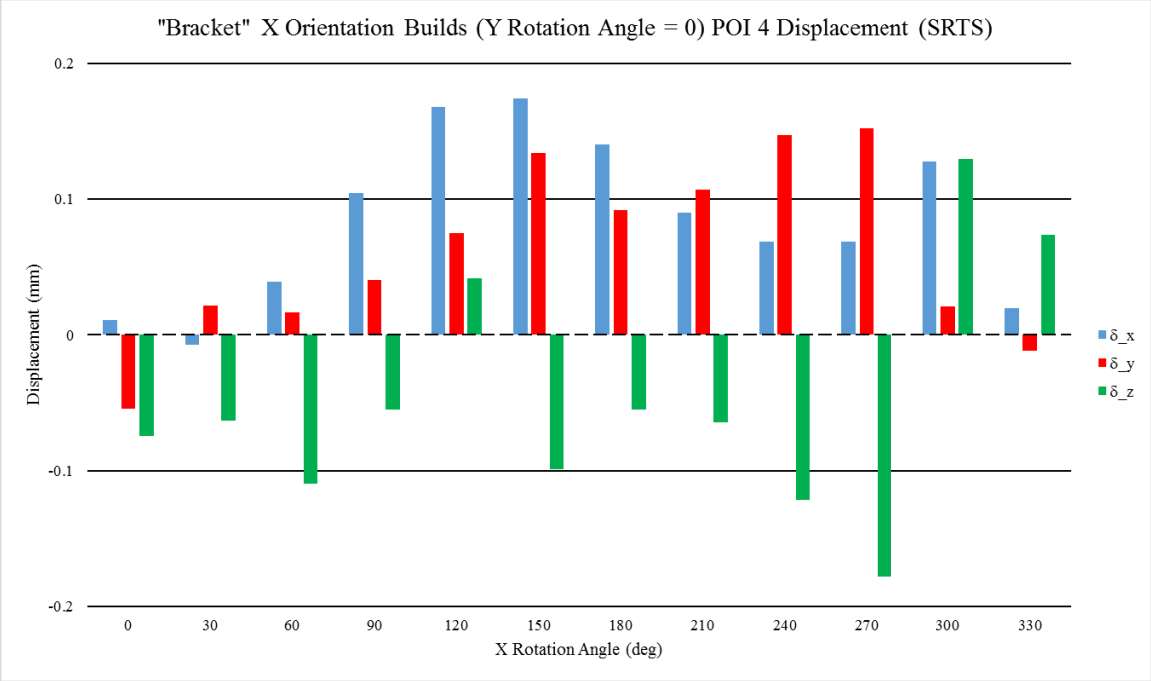

Figure 85: Directional displacement (SRTS) plot for "Bracket" X Orientation Builds (POI 4)

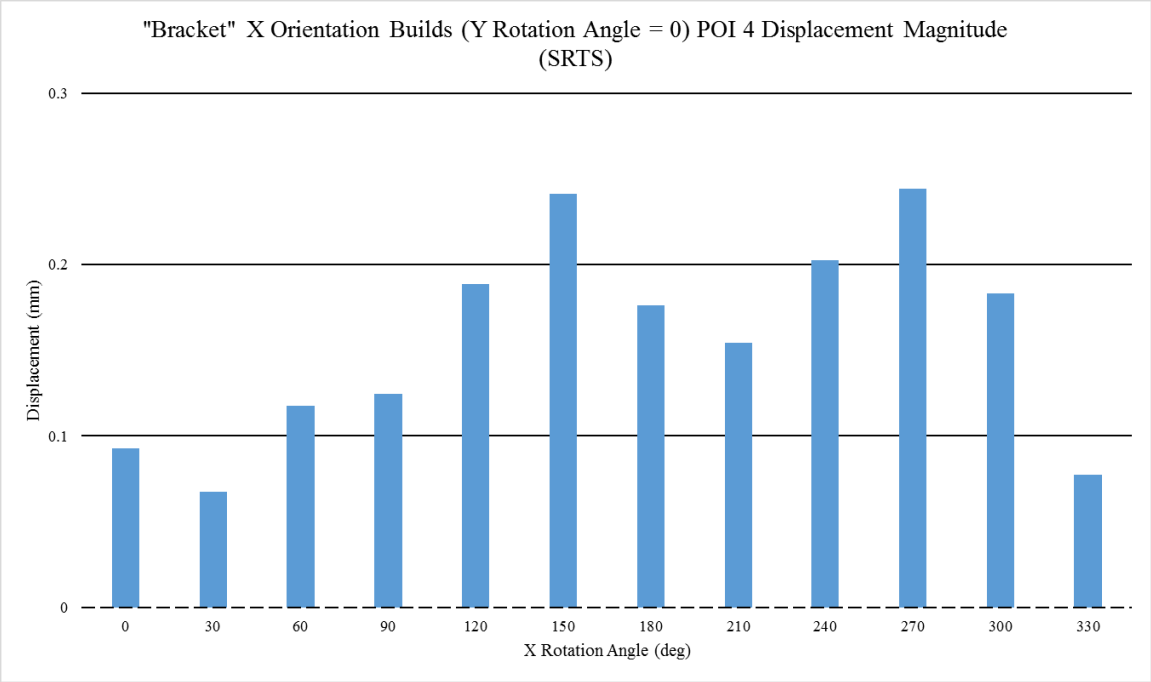

Figure 86: Displacement magnitude (SRTS) plot for "Bracket" X Orientation Builds (POI 4)

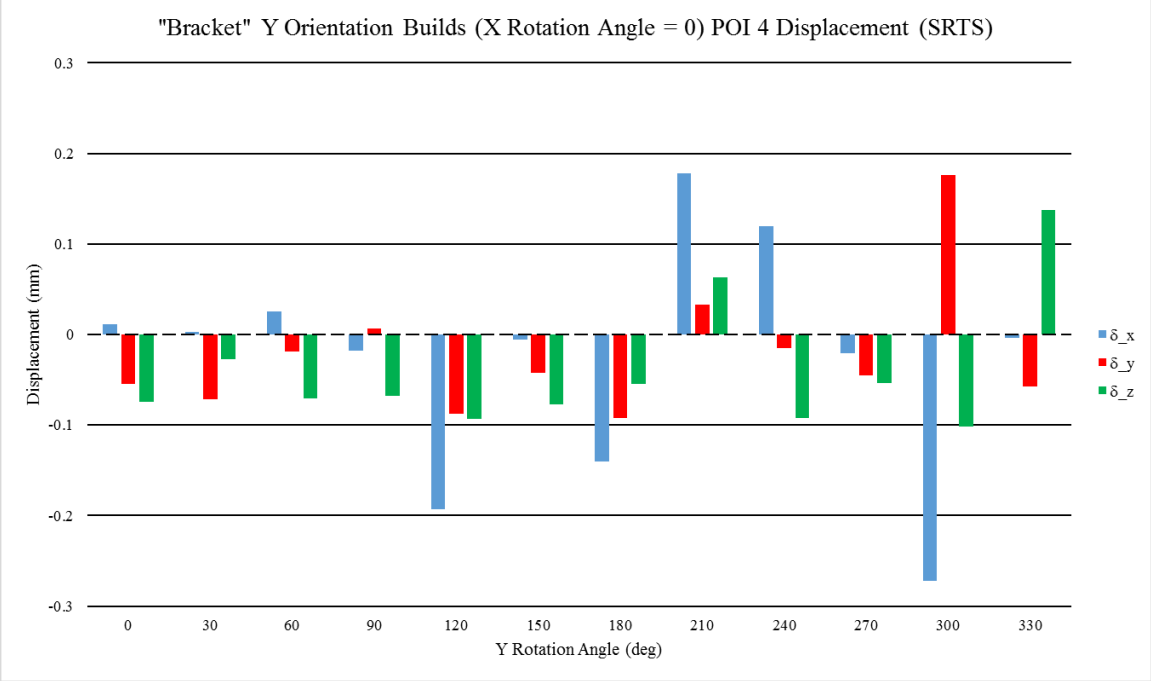

Figure 87: Directional displacement (SRTS) plot for "Bracket" Y Orientation Builds (POI 4)

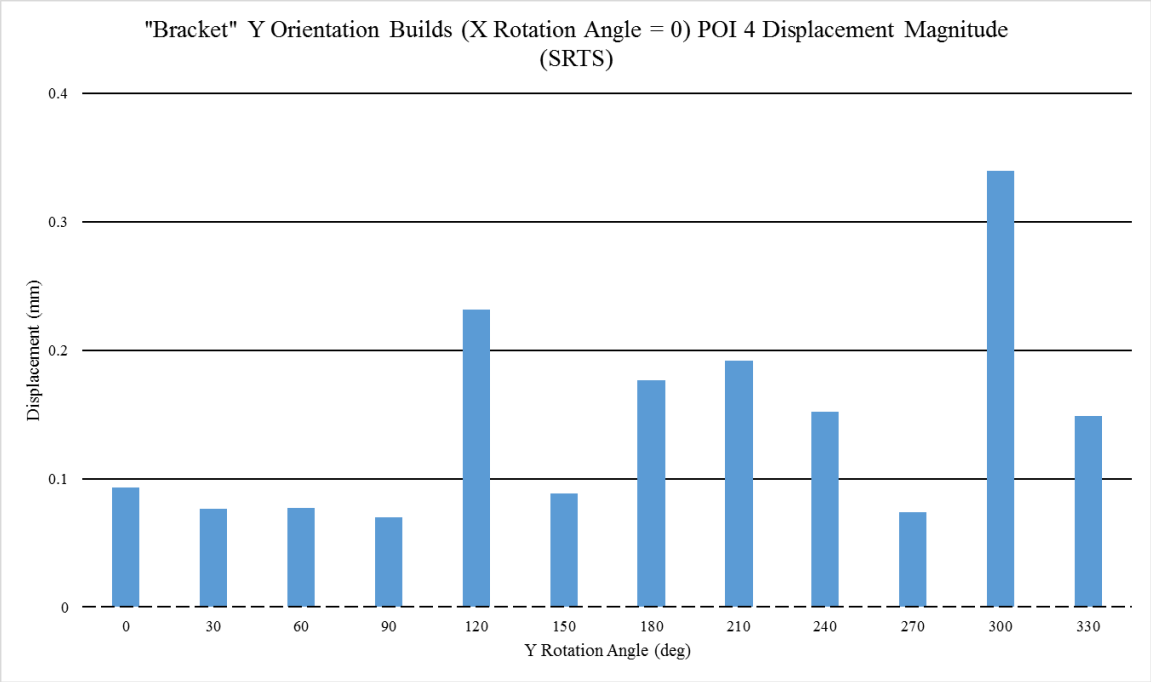

Figure 88: Displacement magnitude (SRTS) plot for "Bracket" Y Orientation Builds (POI 4)

In order to determine the best orientation for the entire "Bracket" part in terms of displacement at the SRTS, the following procedure was used. First, the best orientations for each POI on the "Bracket" part was found. A summary of the best orientations for each POI on the "Bracket" part is found in Table 34. Second, for each orientation found in the previous step the displacement magnitudes of all 4 POIs were averaged, the result is shown in Table 35. Third, the minimum of the displacement magnitudes found in step two was taken as the best orientation of the entire "Bracket" part in terms of SRTS displacement, and that orientation was X0Y60.

Table 34: Summary of best orientation form each "Bracket" part POI (SRTS displacement)

POI #	Best Orientation	Disp Mag (mm)
1	X0Y60	0.0954
2	X0Y270	0.0412
3	X30Y0	0.0359
4	X30Y0	0.0673

Table 35: Displacement magnitudes averages at each best orientation (SRTS displacement)

Best Orientation	Avg Disp Mag (mm)
X0Y60	0.1368
X0Y270	0.2902
X30Y0	0.2895
X30Y0	0.2895

3.1.3: Stress Results: PTS

The plots generated form the stress results at the PTS are shown in Figure 89 through Figure 108 below. For each POI, the Cauchy stresses were placed on one plot, and the Von Mises stress was placed on a second plot. In addition, the XY Cauchy stress data was not plotted at all. The legend for the Cauchy stress plots reads as follows σ_{xx} for the XX stress, σ_{yy} for the YY stress, and σ_{zz} is for the ZZ stress. The value of zero for the y-axis is marked with a dotted line. For the test builds, the resolution for the y-axis between the two stress plots were kept the same; while for the "Bracket" builds, the y-axis resolution was kept the same for all the POIs as well as across the Cauchy and Von Mises stress plots for each POI.

The PTS results for the first test build are shown in, Figure 89 and Figure 90. Figure 89 is the plot for the Cauchy stress data, and Figure 90 is the plot for the Von Mises stress data. The following observations were made from the data. First, there are no ZZ stresses even though there are z-displacements (see Figure 42). This is due to the fact the POIs were on the topmost surface on the parts where there was less restriction to displacement in the z-direction than the other layers. Second, the stresses for the fourth support style does not change very much form base to cantilever side. This reflects the behavior shown in the displacements at the PTS. Third, the stresses on the cantilever side are higher the base side for support styles 1 through 3.

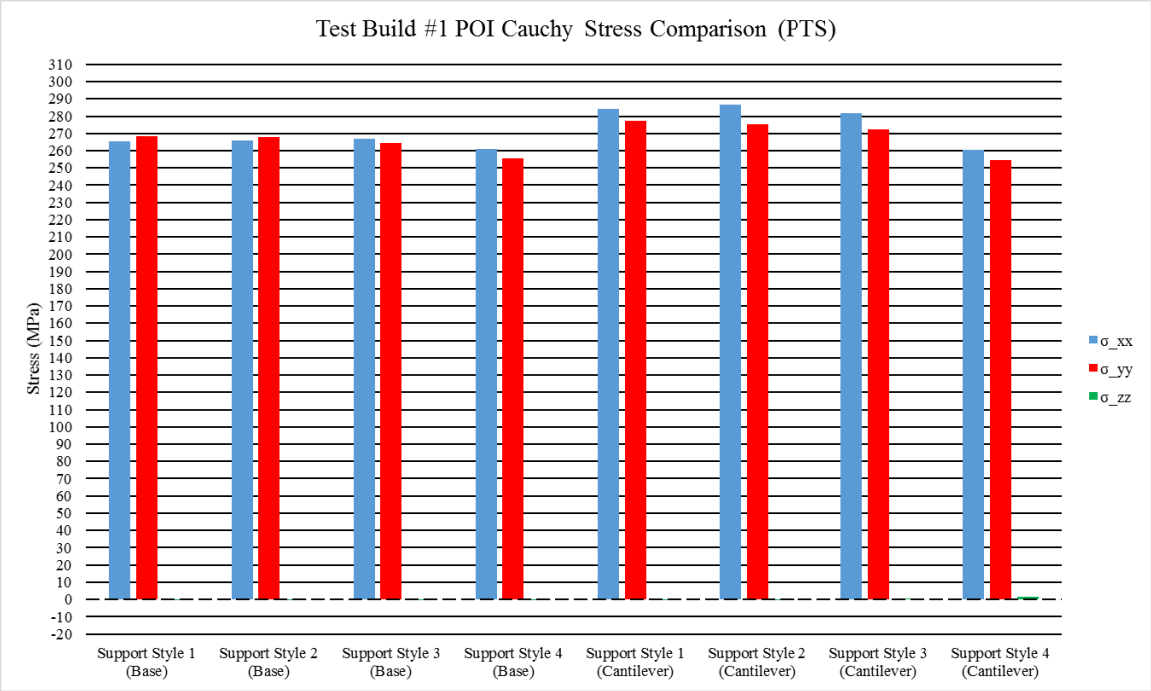

Figure 89: Cauchy stress (PTS) plot for Test Build #1

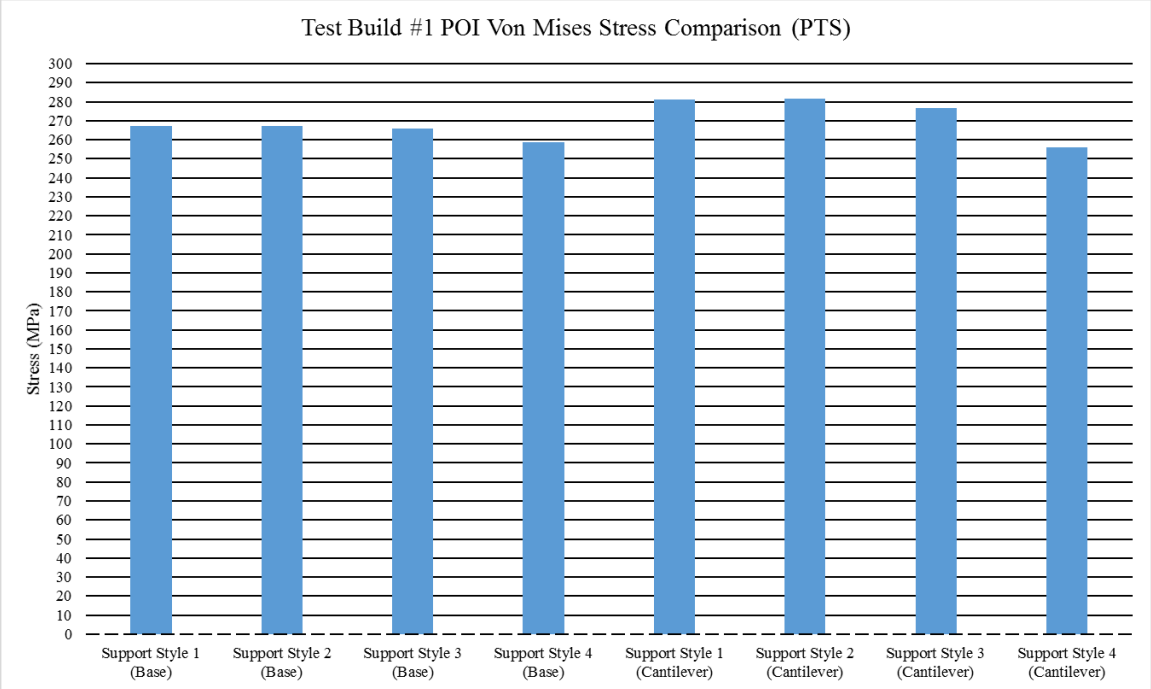

Figure 90: Von Mises stress (PTS) plot for Test Build #1

The PTS results for the second test build are shown in, Figure 91 and Figure 92. Figure 91 is the plot for the Cauchy stress data, and Figure 92 is the plot for the Von Mises stress data. The following observations were made from the data. First, the stresses from

the second test build were not much bigger than the stresses in the first test build. This indicated that the geometry and the size of the part had a greater impact on the displacement than the stresses did. Second, like the first test build, the ZZ stresses are almost nonexistent.

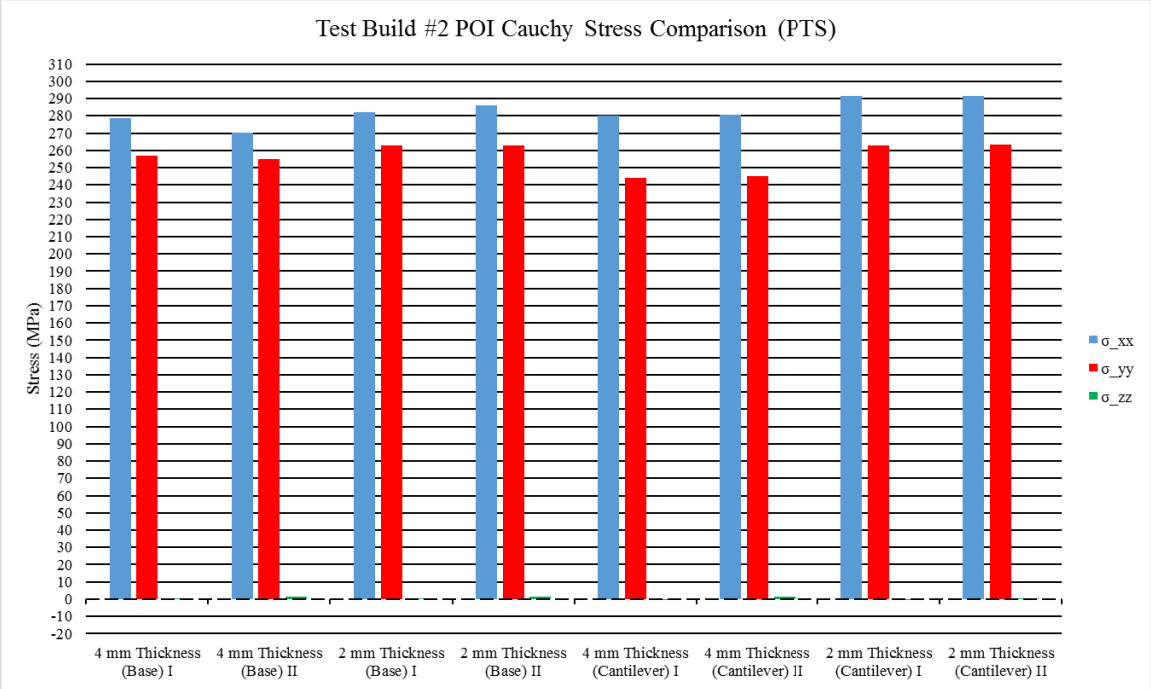

Figure 91: Cauchy stress (PTS) plot for Test Build #2

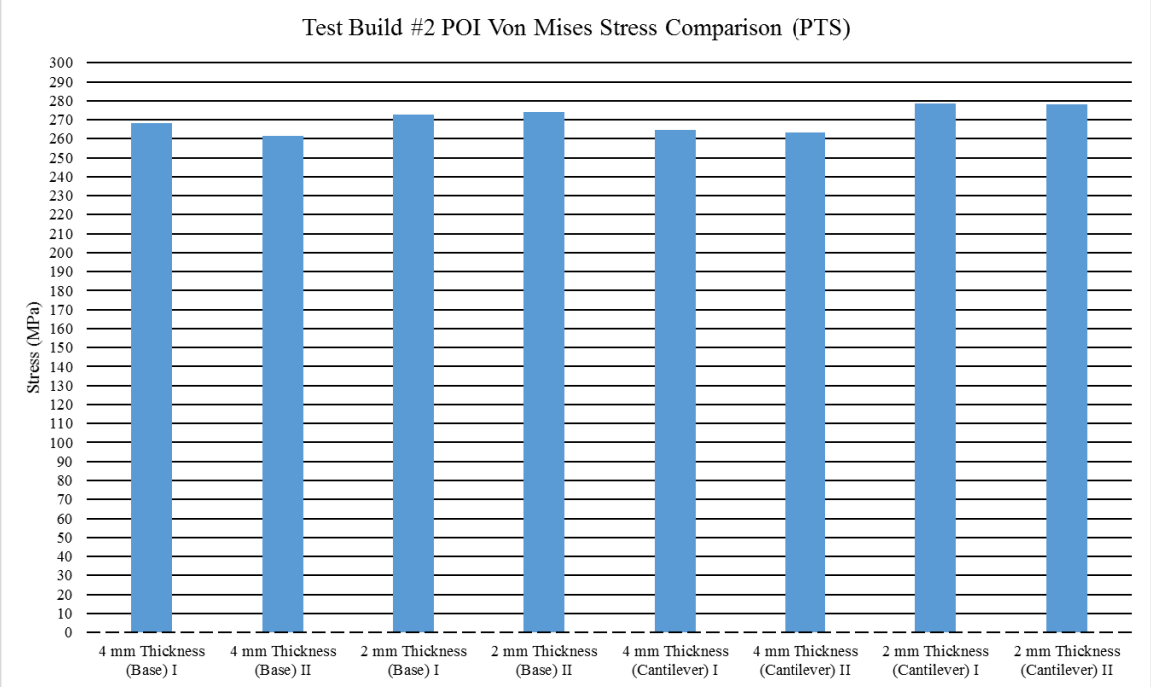

Figure 92: Von Mises stress (PTS) plot for Test Build #2

The PTS data at POI 1 for all the orientations of the “Bracket” part build are shown in Figure 93 through Figure 96: Figure 93 is the plot for the Cauchy stress data of the X orientation builds, Figure 94 is the plot for the Von Mises stress data of the X orientation builds, Figure 95 is the plot for the Cauchy stress data of the Y, and Figure 96 is the plot for the Von Mises stress data of the Y orientation builds. Based on the aforementioned plots, the following observations were made. First, the worst orientation of the “Bracket” part orientation at POI 1 was X90Y0 with a Von Mises stress of 311.85 MPa. Second, the best orientation of the “Bracket” part at POI 1 was X0Y150 with a Von Mises stress of 47.04 MPa.

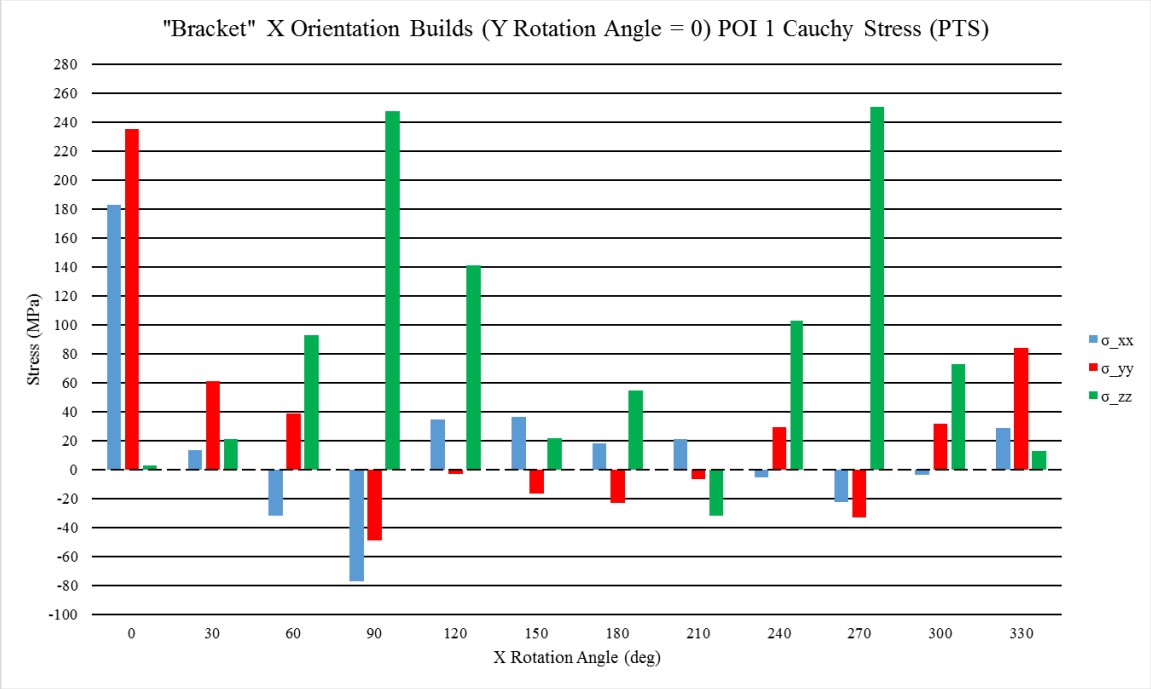

Figure 93: Cauchy stress (PTS) plot for “Bracket” X Orientation Builds (POI 1)

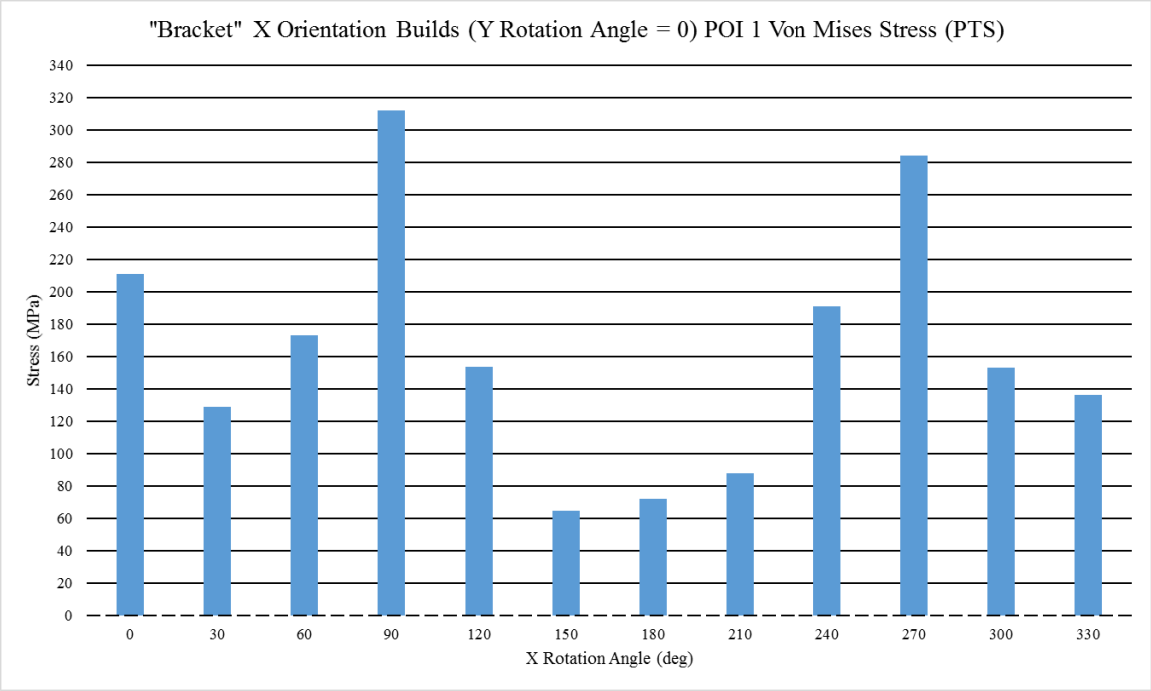

Figure 94: Von Mises stress (PTS) plot for "Bracket" X Orientation Builds (POI 1)

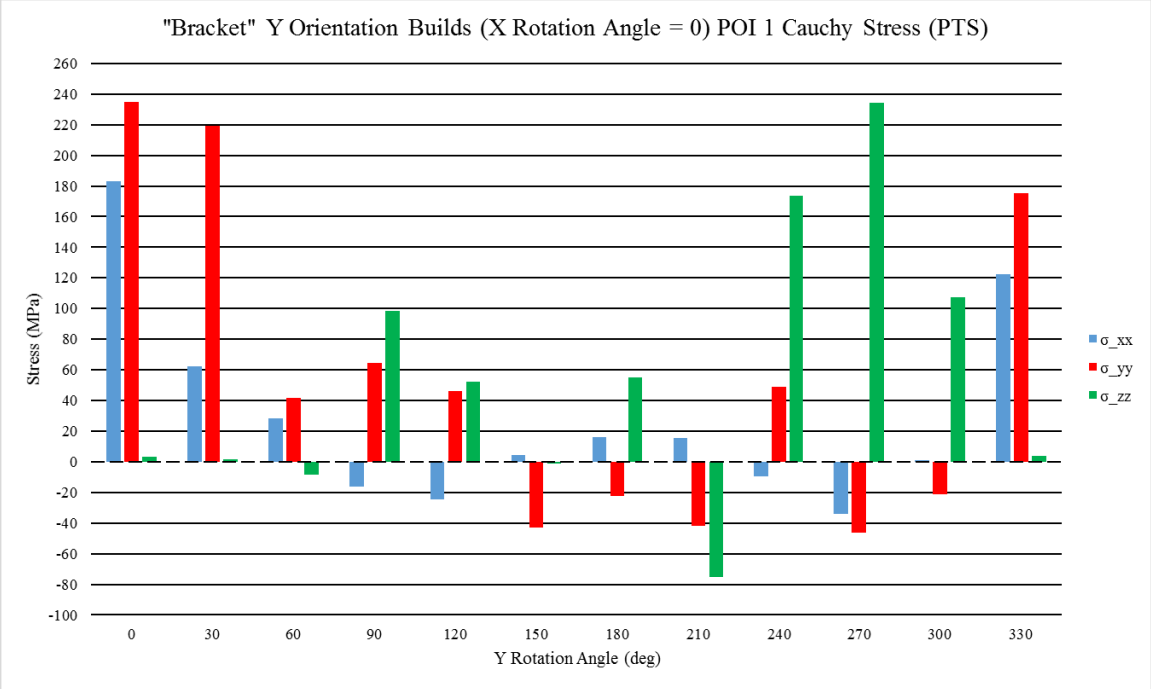

Figure 95: Cauchy stress (PTS) plot for "Bracket" Y Orientation Builds (POI 1)

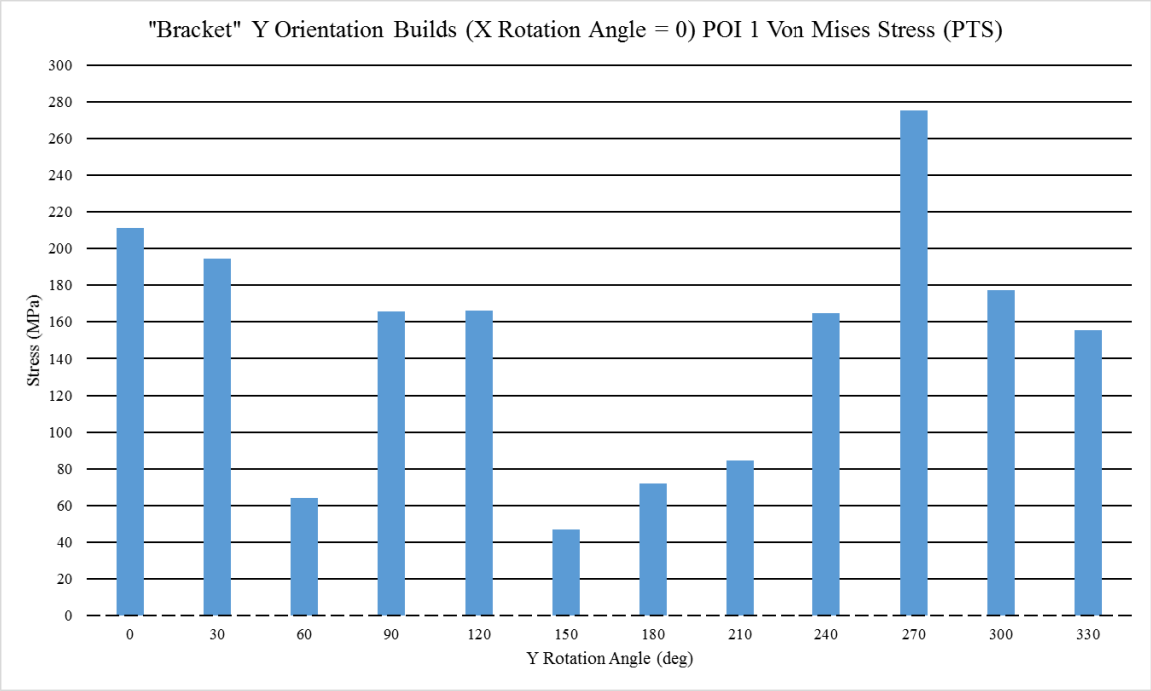

Figure 96: Von Mises stress (PTS) plot for "Bracket" Y Orientation Builds (POI 1)

The PTS data at POI 2 for all the orientations of the "Bracket" part build are shown in Figure 97 through Figure 100: Figure 97 is the plot for the Cauchy stress data of the X orientation builds, Figure 98 is the plot for the Von Mises stress data of the X orientation builds, Figure 99 is the plot for the Cauchy stress data of the Y, and Figure 100 is the plot for the Von Mises stress data of the Y orientation builds. Based on the aforementioned plots, the following observations were made. First, the worst orientation of the "Bracket" part orientation at POI 2 was X0Y120 with a Von Mises stress of 305.03 MPa. Second, the best orientation of the "Bracket" part at POI 2 was X0Y240 with a Von Mises stress of 67.97 MPa.

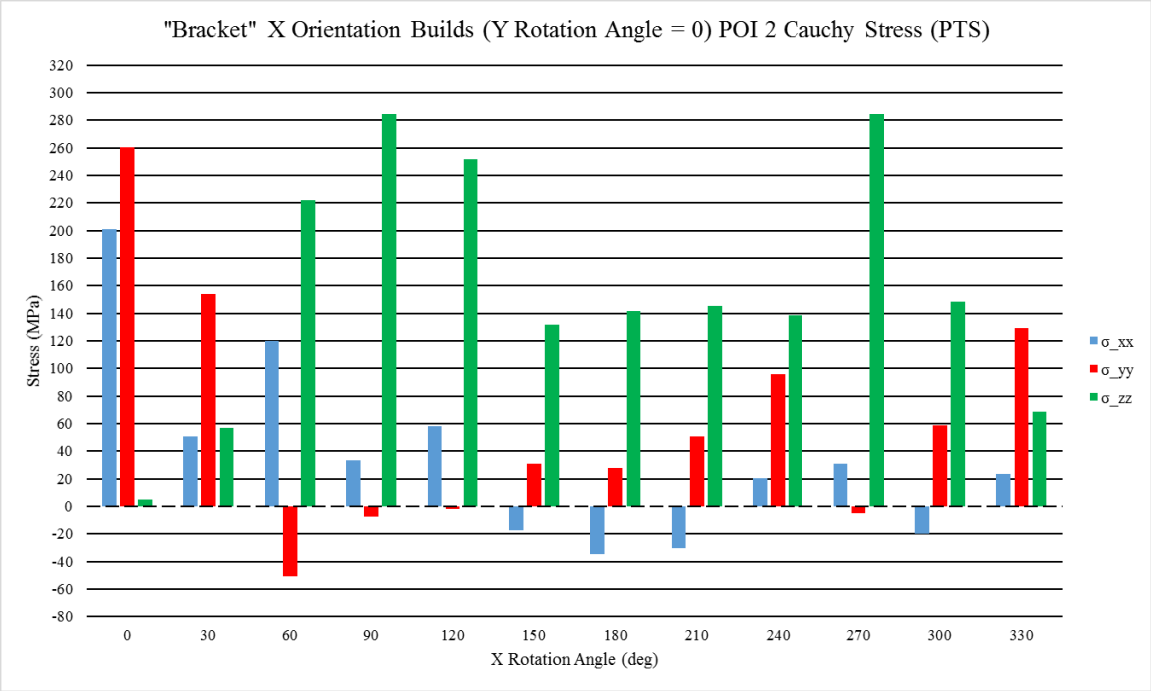

Figure 97: Cauchy stress (PTS) plot for "Bracket" X Orientation Builds (POI 2)

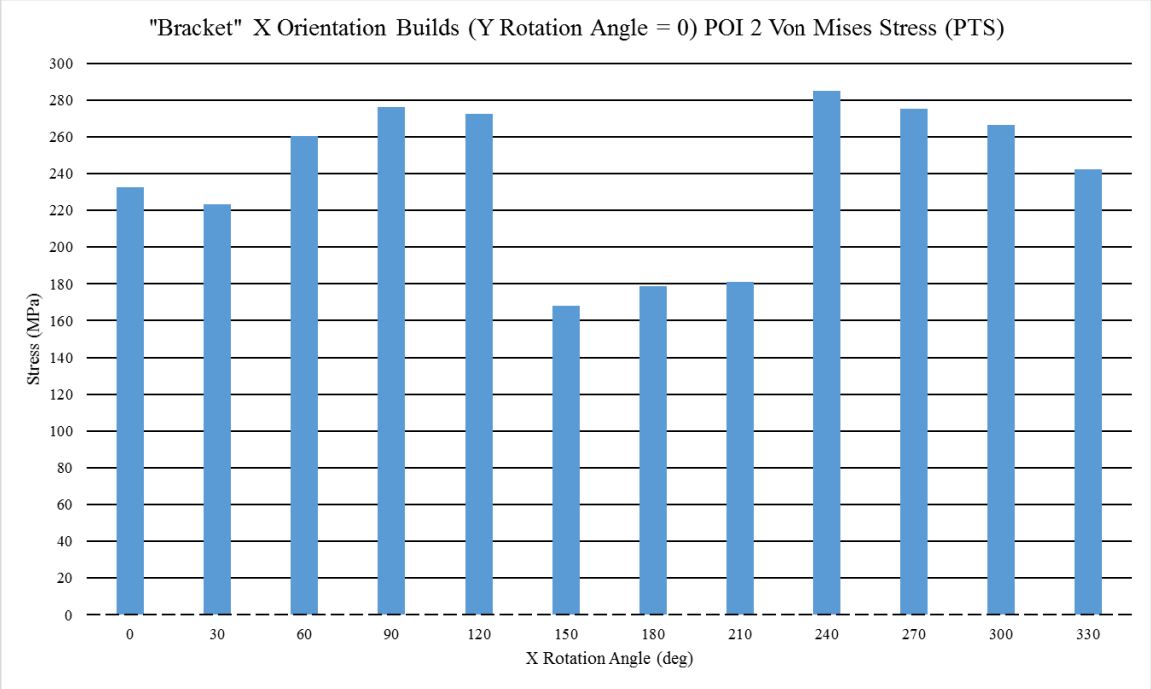

Figure 98: Von Mises stress (PTS) plot for "Bracket" X Orientation Builds (POI 2)

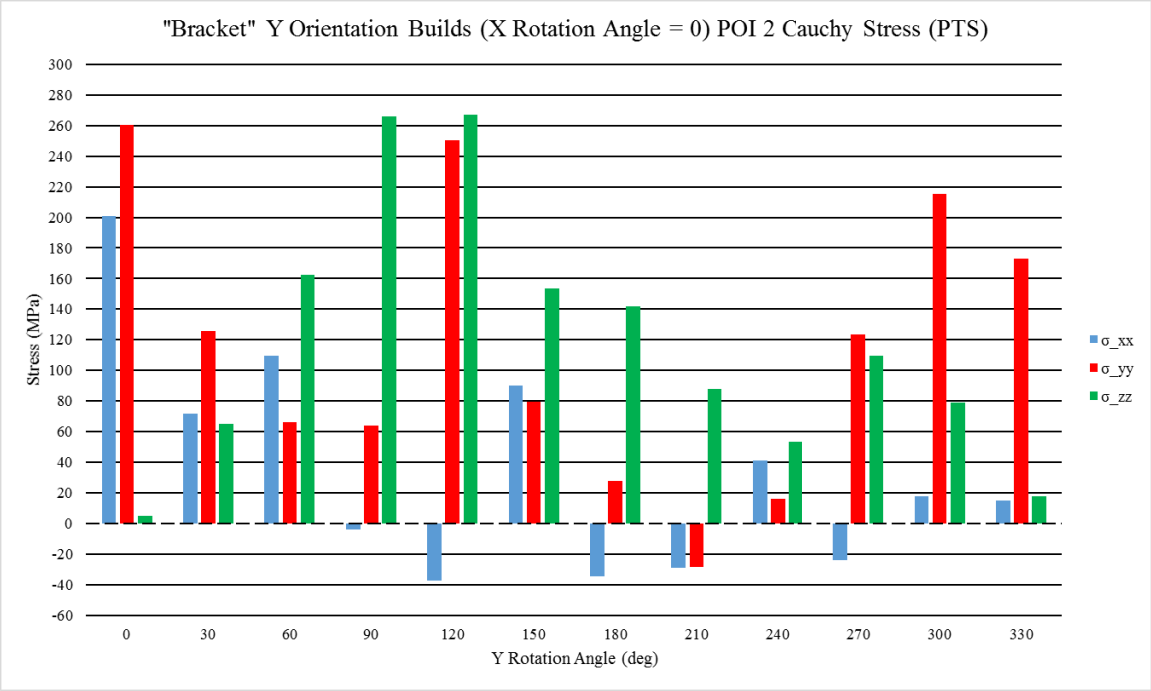

Figure 99: Cauchy stress (PTS) plot for "Bracket" Y Orientation Builds (POI 2)

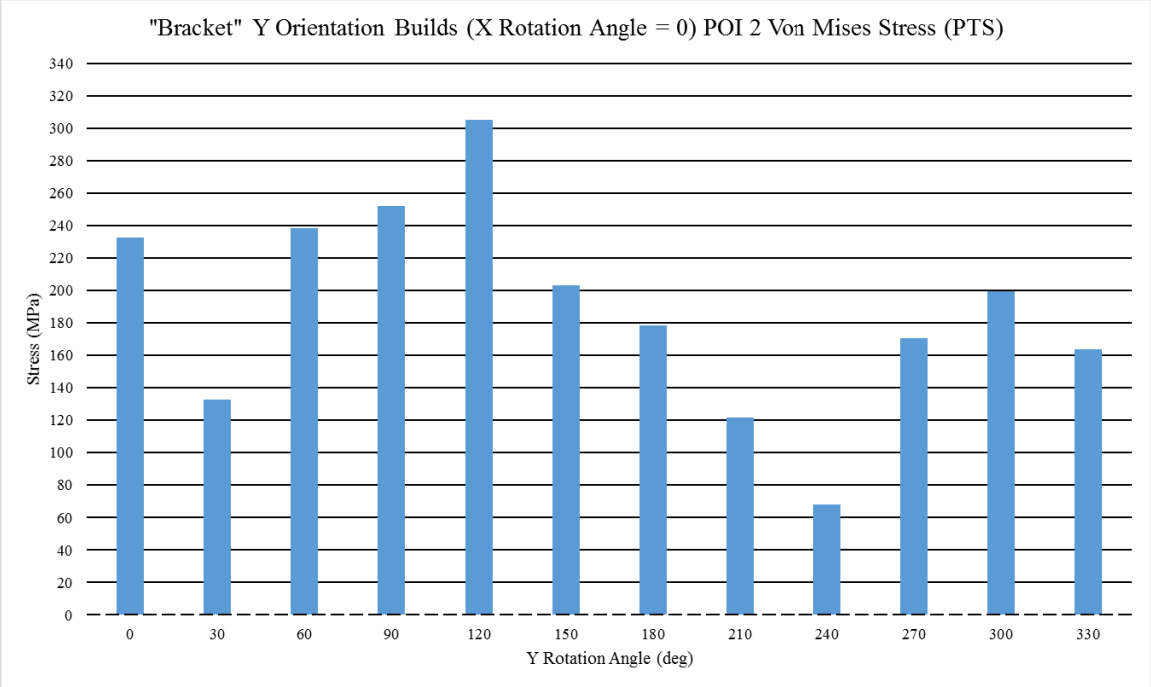

Figure 100: Von Mises stress (PTS) plot for "Bracket" Y Orientation Builds (POI 2)

The PTS data at POI 3 for all the orientations of the "Bracket" part build are shown in Figure 101 through Figure 104: Figure 101 is the plot for the Cauchy stress data of the X orientation builds, Figure 102 is the plot for the Von Mises stress data of the X orientation

builds, Figure 103 is the plot for the Cauchy stress data of the Y, and is Figure 104 the plot for the Von Mises stress data of the Y orientation builds. Based on the aforementioned plots, the following observations were made. First, the worst orientation of the "Bracket" part orientation at POI 3 was X0Y240 with a Von Mises stress of 339.83 MPa. Second, the best orientation of the "Bracket" part at POI 3 was X210Y0 with a Von Mises stress of 66.2 MPa.

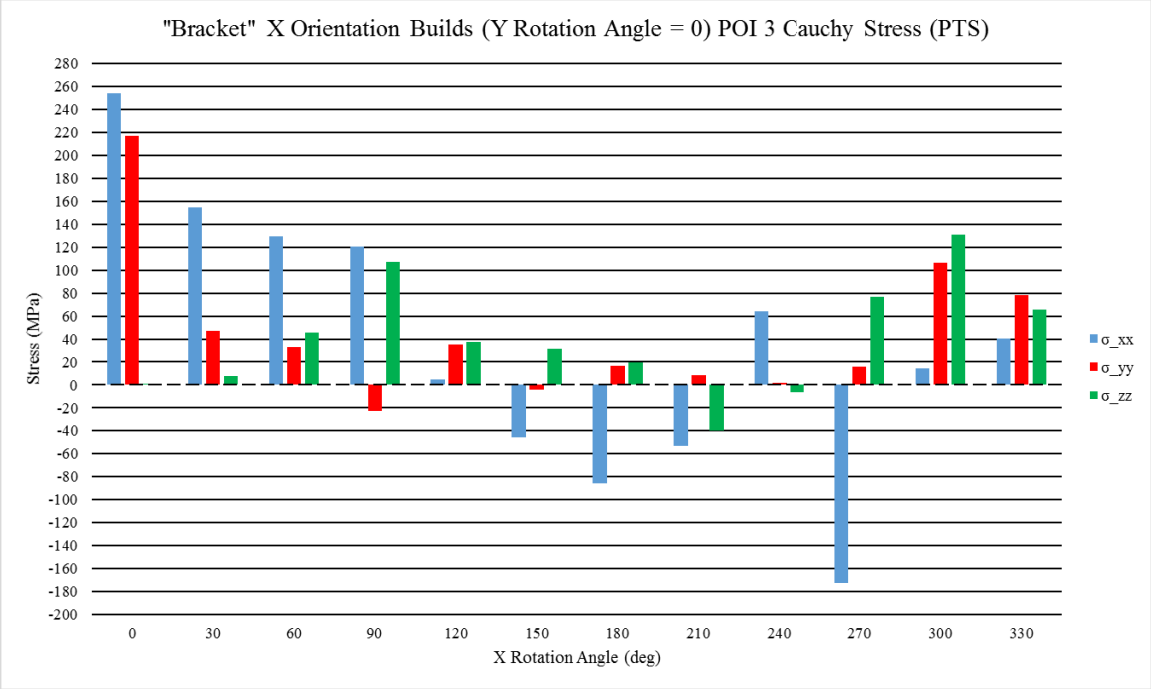

Figure 101: Cauchy stress (PTS) plot for "Bracket" X Orientation Builds (POI 3)

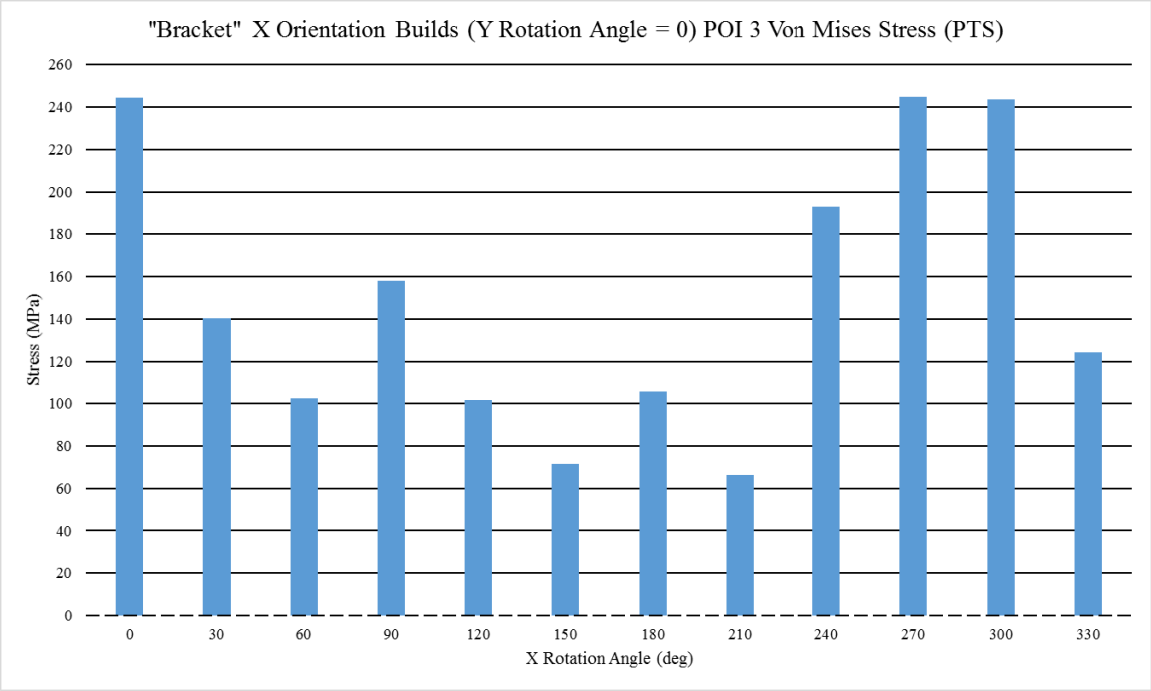

Figure 102: Von Mises stress (PTS) plot for "Bracket" X Orientation Builds (POI 3)

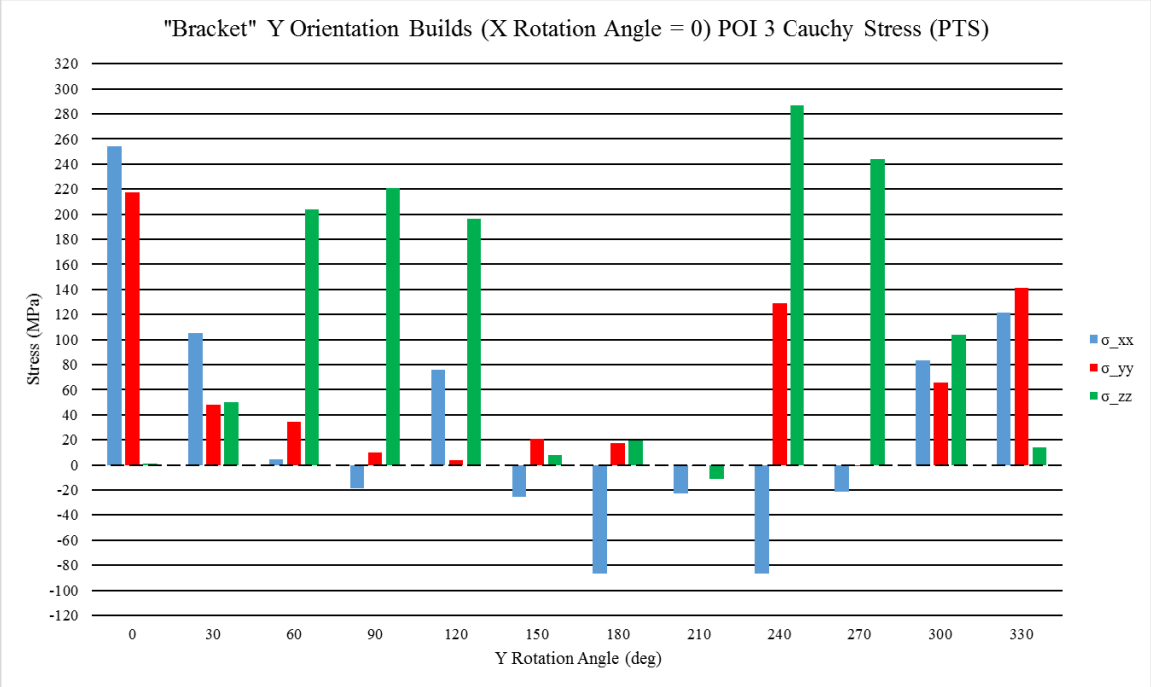

Figure 103: Cauchy stress (PTS) plot for "Bracket" Y Orientation Builds (POI 3)

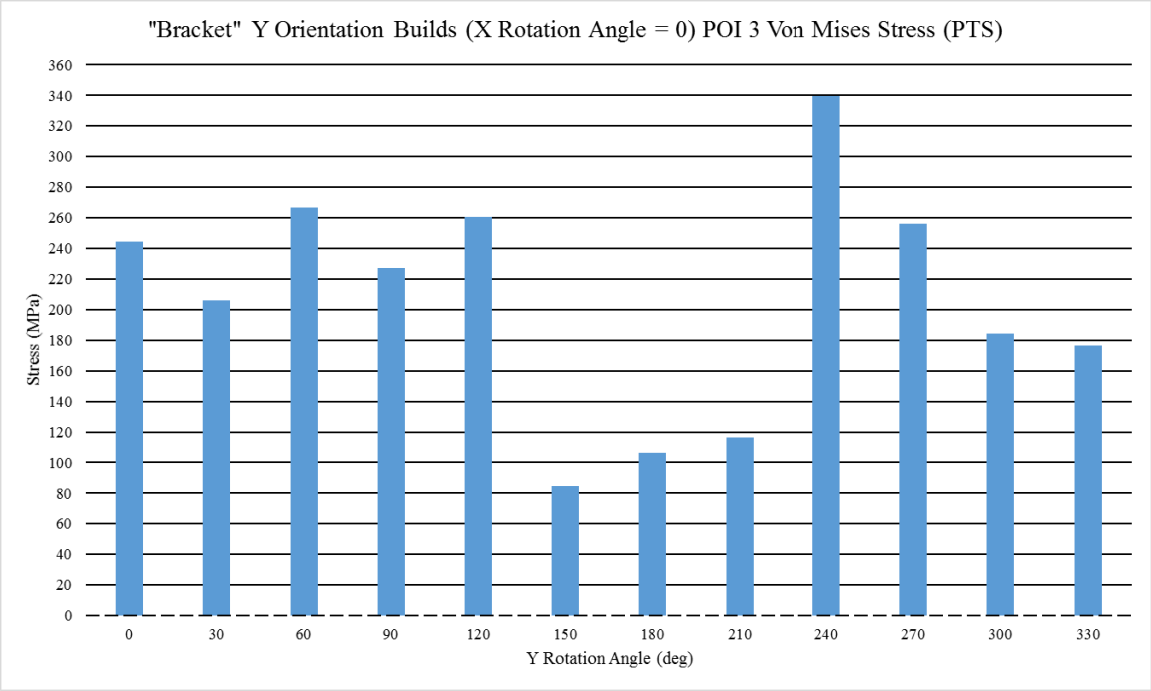

Figure 104: Von Mises stress (PTS) plot for "Bracket" Y Orientation Builds (POI 3)

The PTS data at POI 4 for all the orientations of the "Bracket" part build are shown in Figure 105 through Figure 108: Figure 105 is the plot for the Cauchy stress data of the X orientation builds, Figure 106 is the plot for the Von Mises stress data of the X orientation builds, Figure 107 is the plot for the Cauchy stress data of the Y, and Figure 108 is the plot for the Von Mises stress data of the Y orientation builds. Based on the aforementioned plots, the following observations were made. First, the worst orientation of the "Bracket" part orientation at POI 4 was X0Y330 with a Von Mises stress of 294.27 MPa. Second, the best orientation of the "Bracket" part at POI 4 was X180Y0 with a Von Mises stress of 51.39 MPa.

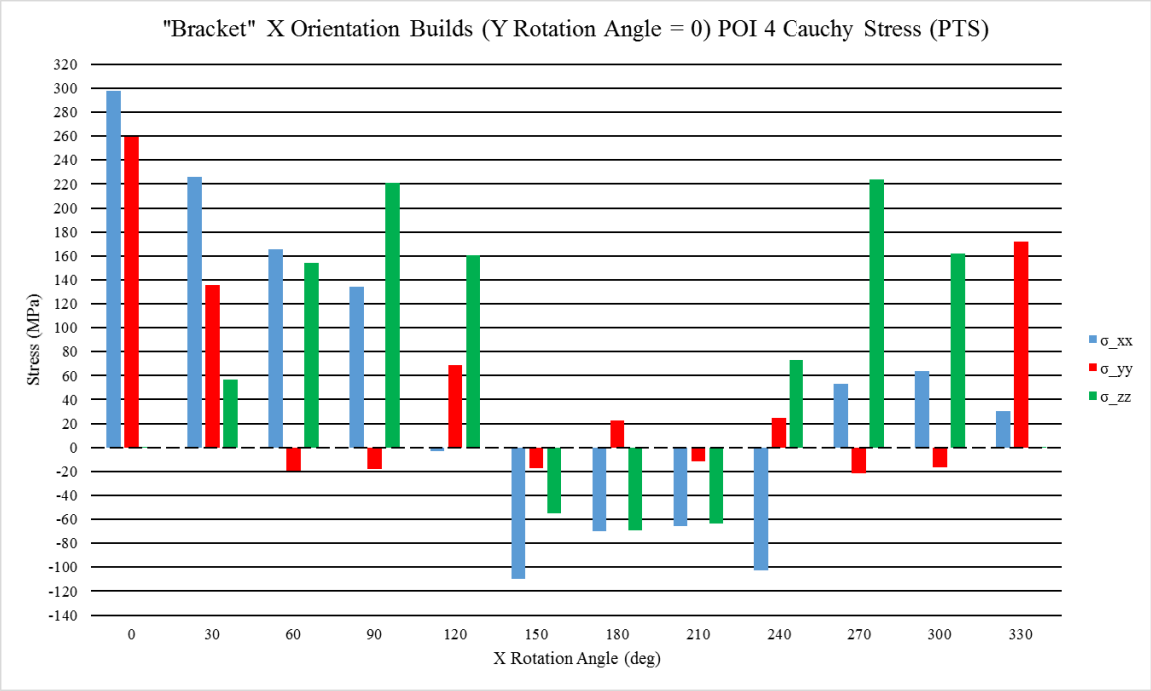

Figure 105: Cauchy stress (PTS) plot for "Bracket" X Orientation Builds (POI 4)

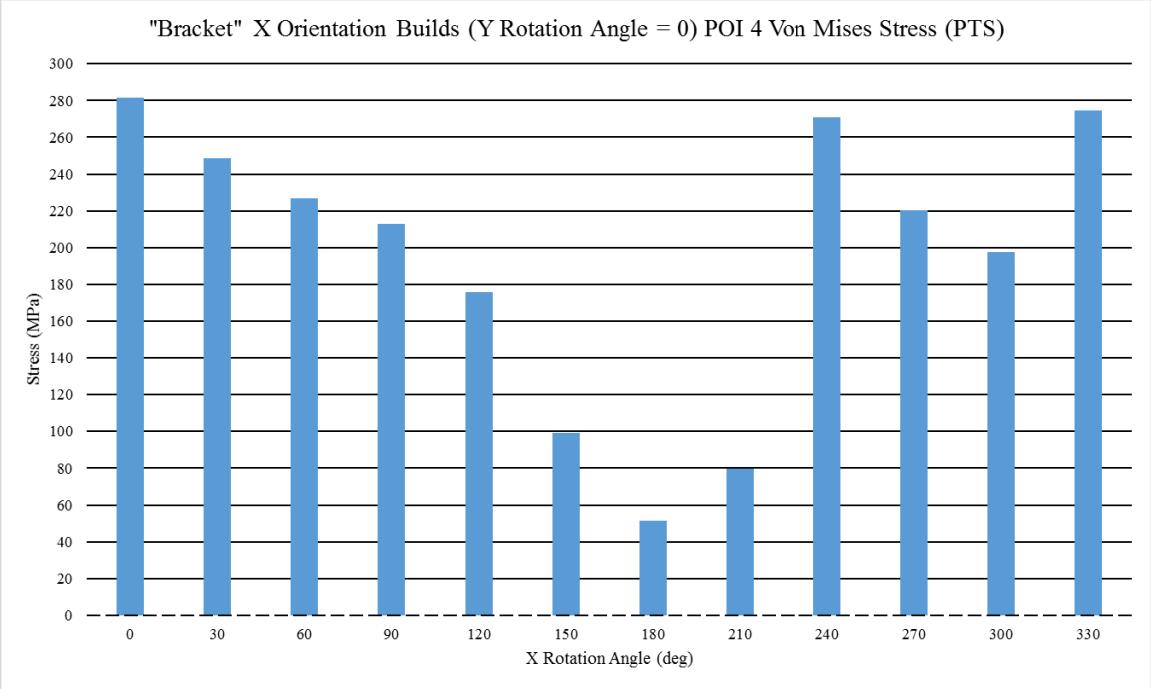

Figure 106: Von Mises stress (PTS) plot for "Bracket" X Orientation Builds (POI 4)

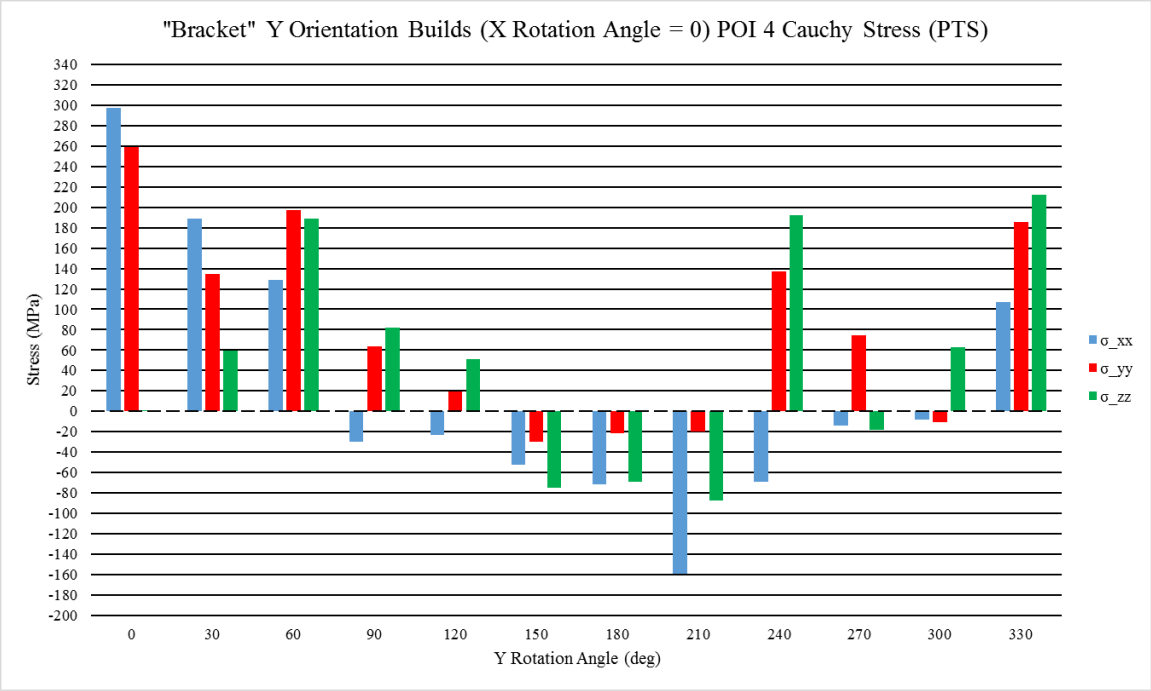

Figure 107: Cauchy stress (PTS) plot for "Bracket" Y Orientation Builds (POI 4)

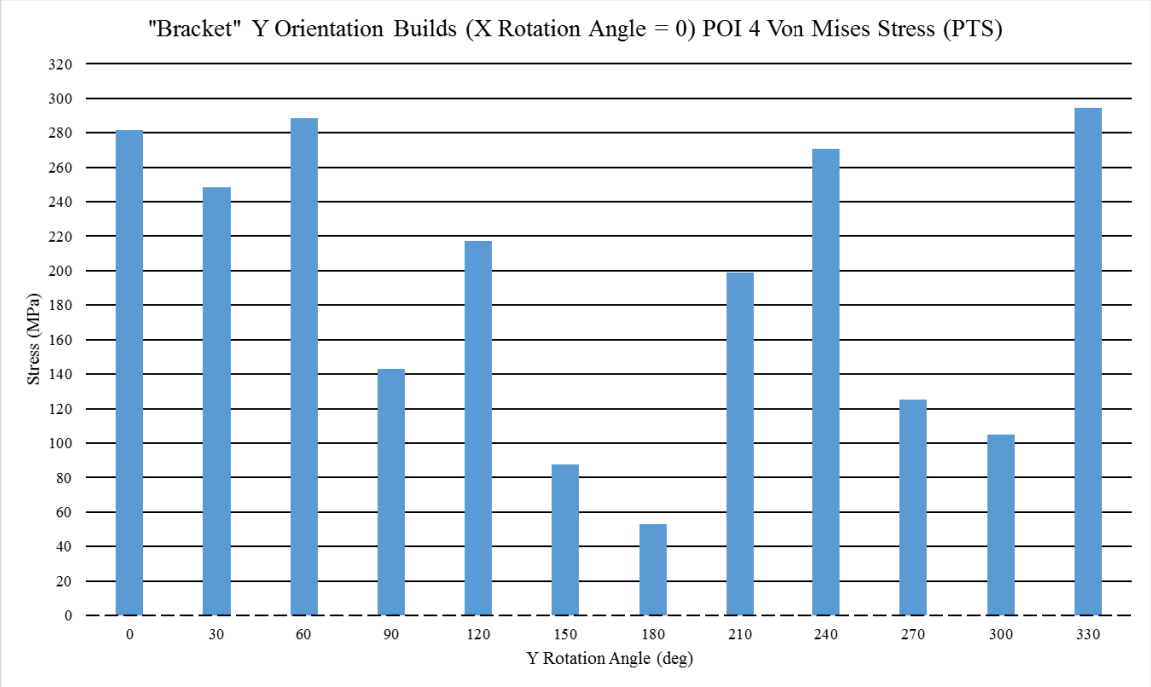

Figure 108: Von Mises stress (PTS) plot for "Bracket" Y Orientation Builds (POI 4)

In order to determine the best orientation for the entire "Bracket" part in terms of stress at the PTS, the following procedure was used. First, the best orientations for each POI on the "Bracket" part was found. A summary of the best orientations for each POI on

the “Bracket” part is found in Table 36. Second, for each orientation found in the previous step the Von Mises stresses of all 4 POIs were averaged, the result is shown in Table 33. Third, the minimum of the Von Mises stresses found in step two was taken as the best orientation of the entire “Bracket” part in terms of PTS stress, and that orientation was X180Y0.

Table 36: Summary of best orientation form each "Bracket" part POI (PTS stress)

POI #	Best Orientation	Von Mises Stress (MPa)
1	X0Y150	47.04
2	X0Y240	67.97
3	X210Y0	66.20
4	X180Y0	51.39

Table 37: Displacement magnitudes averages at each best orientation (PTS stress)

Best Orientation	Avg VM Stress (MPa)
X0Y150	105.61
X0Y240	210.76
X210Y0	103.76
X180Y0	102.06

3.1.4: Stress Results: SRTS

The plots generated form the stress results at the SRTS are shown in Figure 109 through Figure 128 below. The SRTS results for the first test build are shown in, Figure 109 and Figure 110. Figure 109 is the plot for the Cauchy stress data, and Figure 110 is the plot for the Von Mises stress data. The following observations were made from the data. First, the stresses were lower after substrate removal than before substrate removal. This is due to stress being released as the part was being detached from the build plate. Second, the XX stresses decreased more than the YY stresses did. Third, the cantilever and base sides of the parts sustained similar decreases.

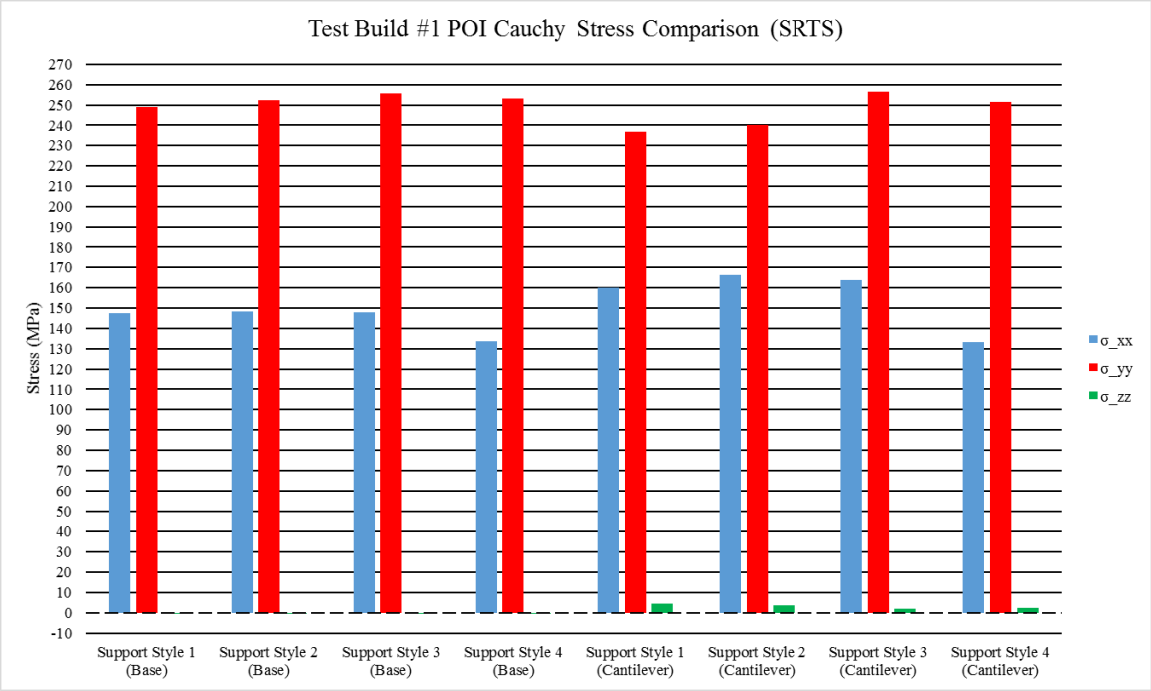

Figure 109: Cauchy stress (SRTS) plot for Test Build #1

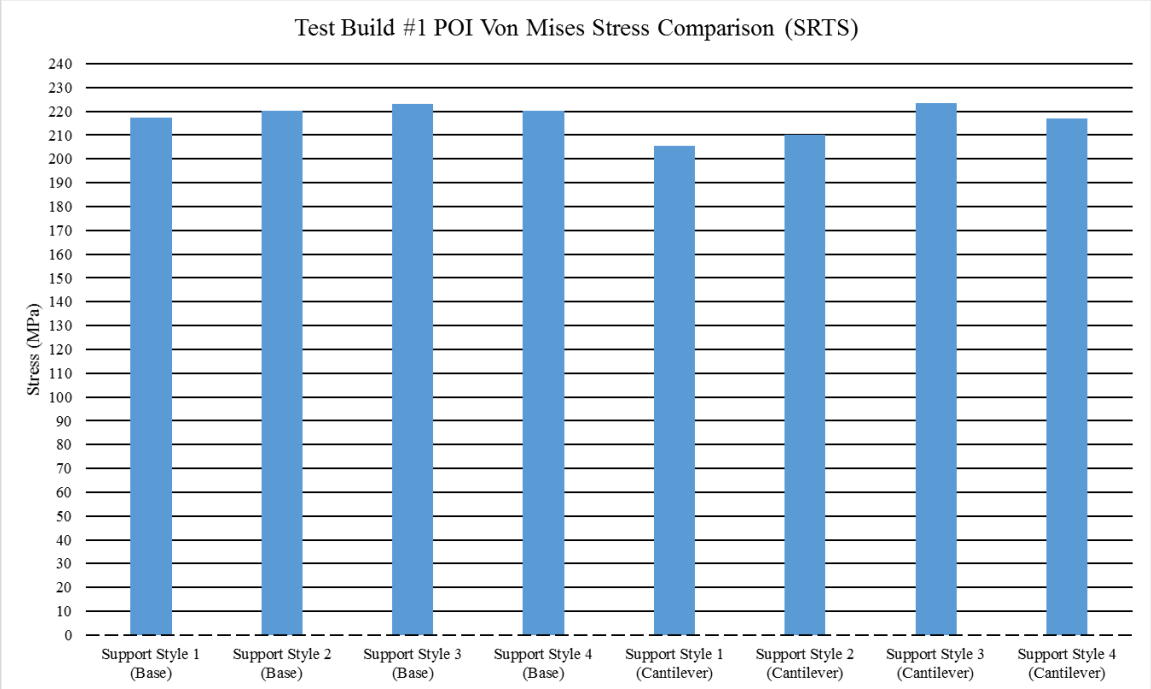

Figure 110: Von Mises stress (SRTS) plot for Test Build #1

The SRTS results for the second test build are shown in, Figure 111 and Figure 112. Figure 111 is the plot for the Cauchy stress data, and Figure 112 is the plot for the Von Mises stress data. The following observations were made from the data. First, similarly to

the first test build the stresses are lower compared to the PTS stress results. Second, the cantilever side stresses decreased far more than the base side stresses. This is due to the support structure holding less stresses than the solid block that exists under the base side.

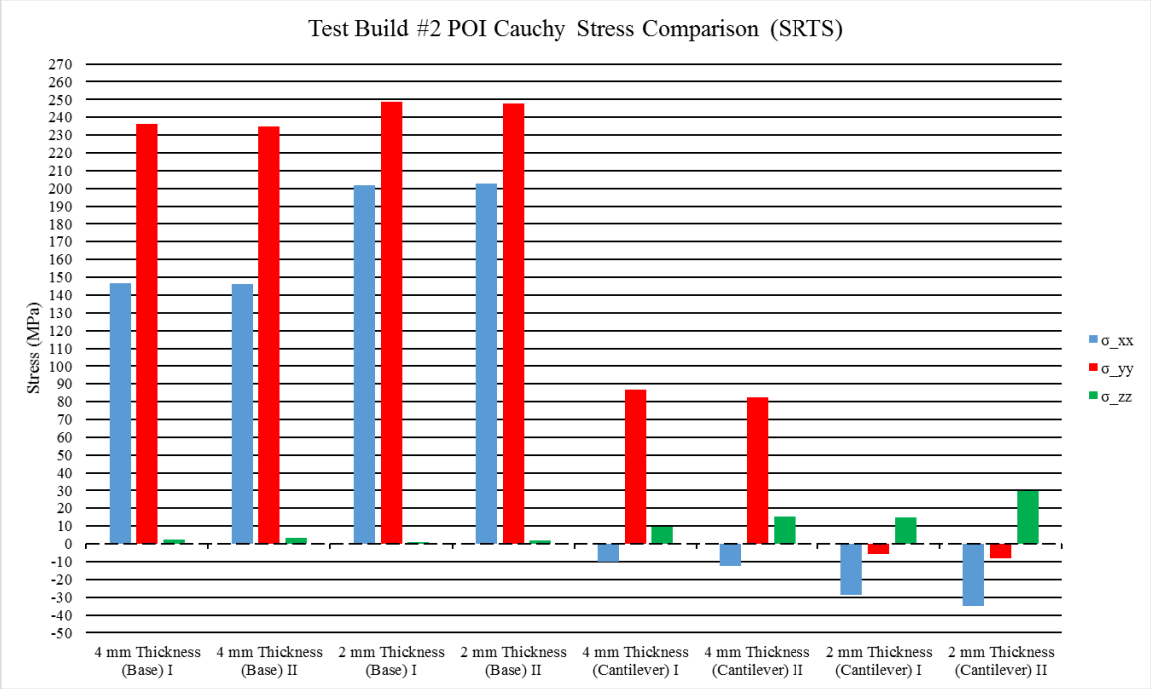

Figure 111: Cauchy stress (SRTS) plot for Test Build #2

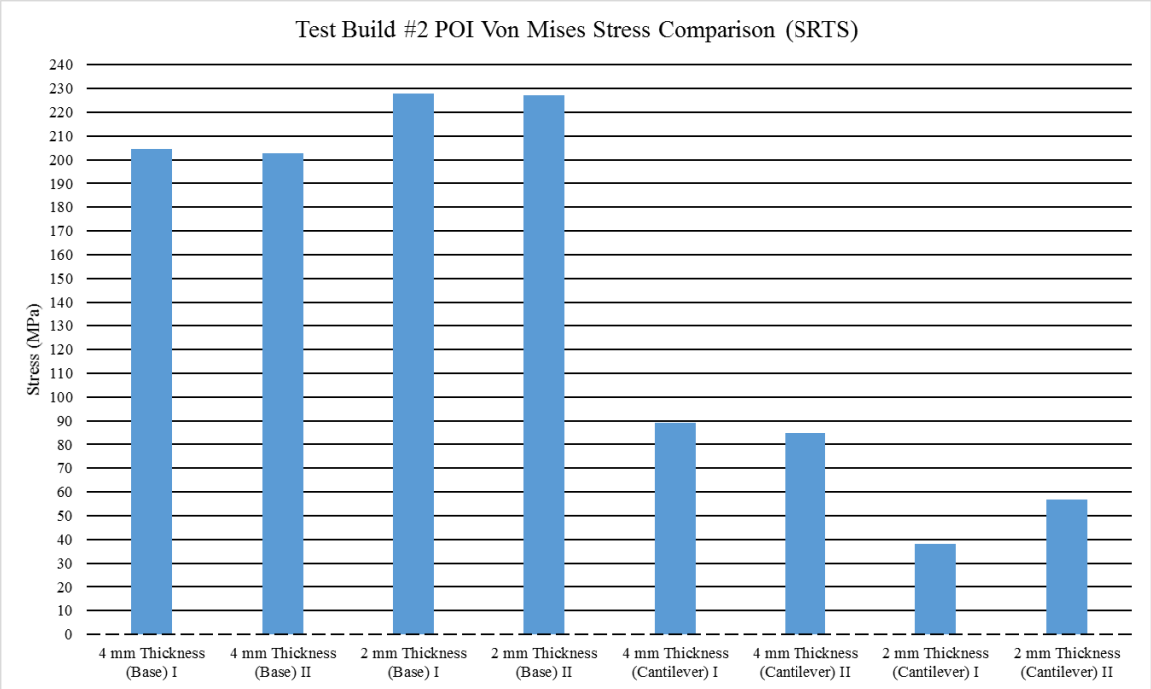

Figure 112: Von Mises stress (SRTS) plot for Test Build #2

The SRTS data at POI 1 for all the orientations of the “Bracket” part build are shown in Figure 113 through Figure 116: Figure 113 is the plot for the Cauchy stress data of the X orientation builds, Figure 114 is the plot for the Von Mises stress data of the X orientation builds, Figure 115 is the plot for the Cauchy stress data of the Y, and Figure 116 is the plot for the Von Mises stress data of the Y orientation builds. Based on the aforementioned plots, the following observations were made. First, the worst orientation of the “Bracket” part orientation at POI 1 was X90Y0 with a Von Mises stress of 293.52 MPa. Second, the best orientation of the “Bracket” part at POI 1 was X0Y150 with a Von Mises stress of 46.43 MPa.

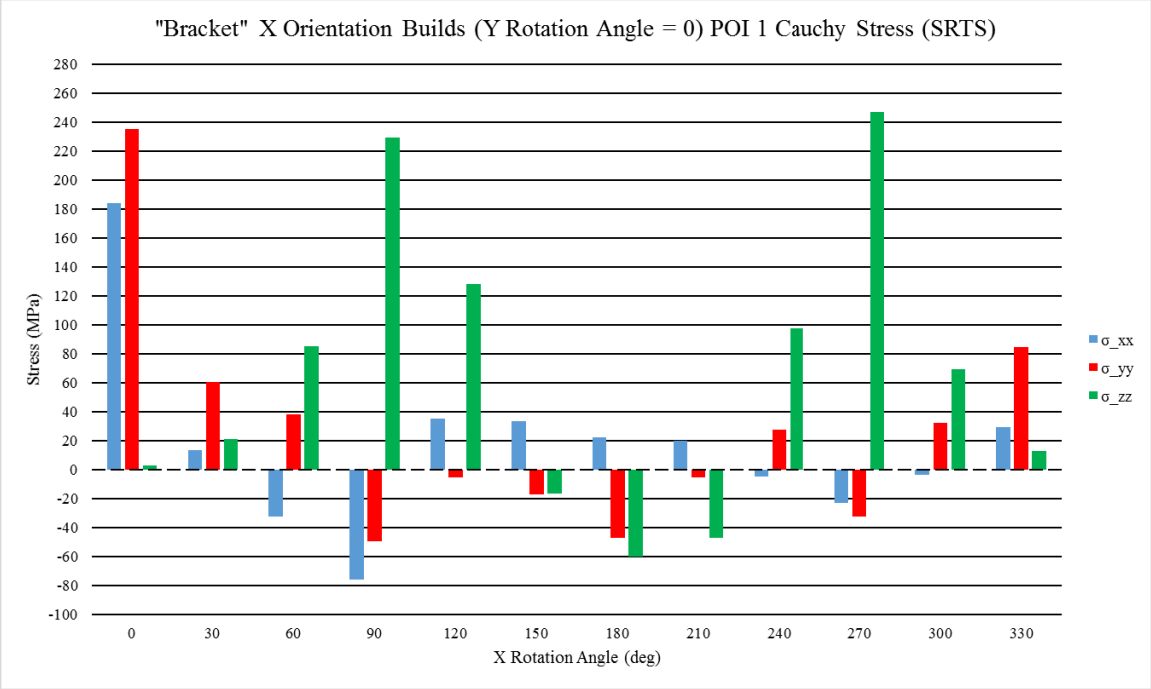

Figure 113: Cauchy stress (SRTS) plot for “Bracket” X Orientation Builds (POI 1)

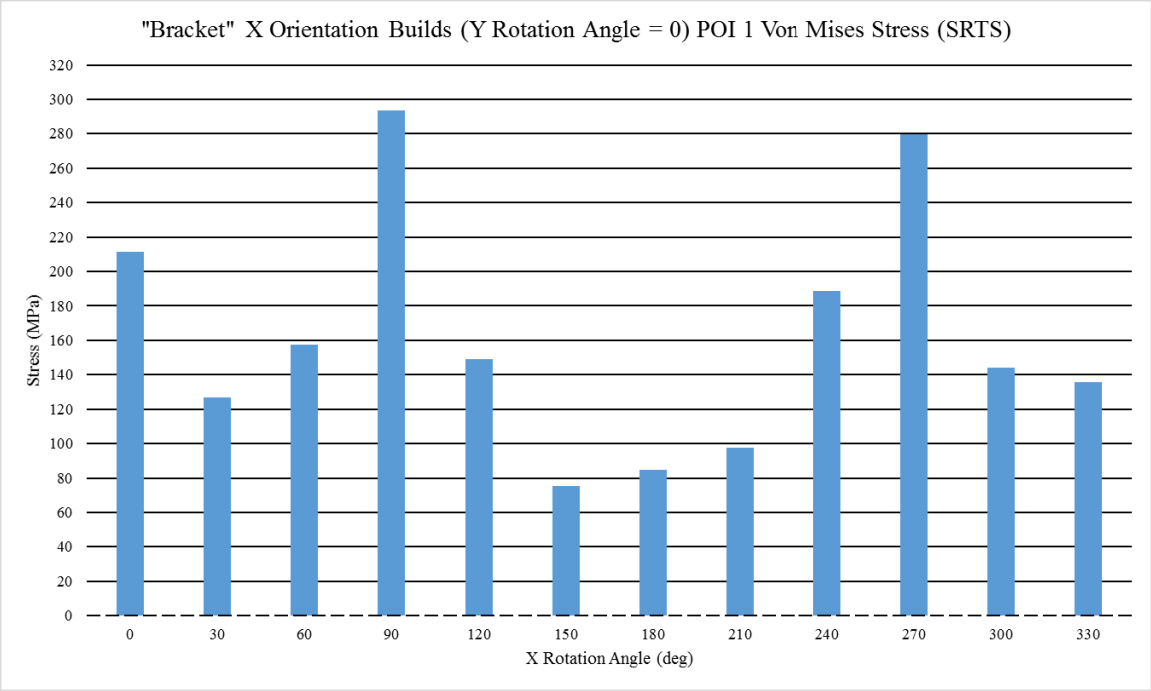

Figure 114: Von Mises stress (SRTS) plot for "Bracket" X Orientation Builds (POI 1)

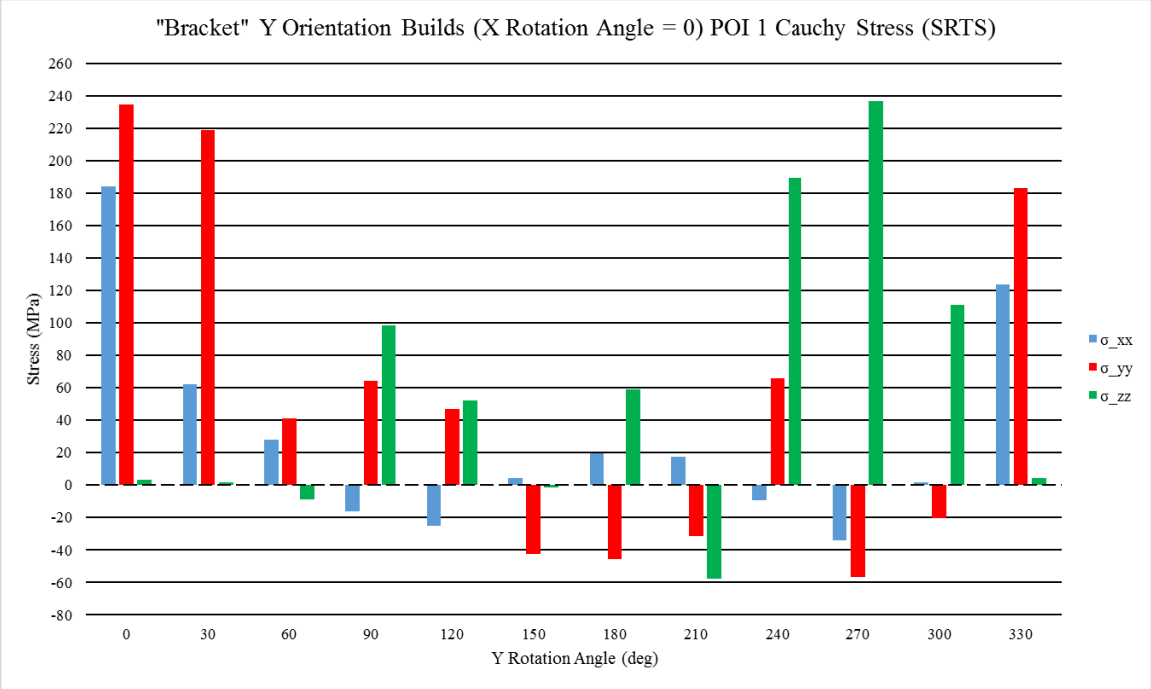

Figure 115: Cauchy stress (SRTS) plot for "Bracket" Y Orientation Builds (POI 1)

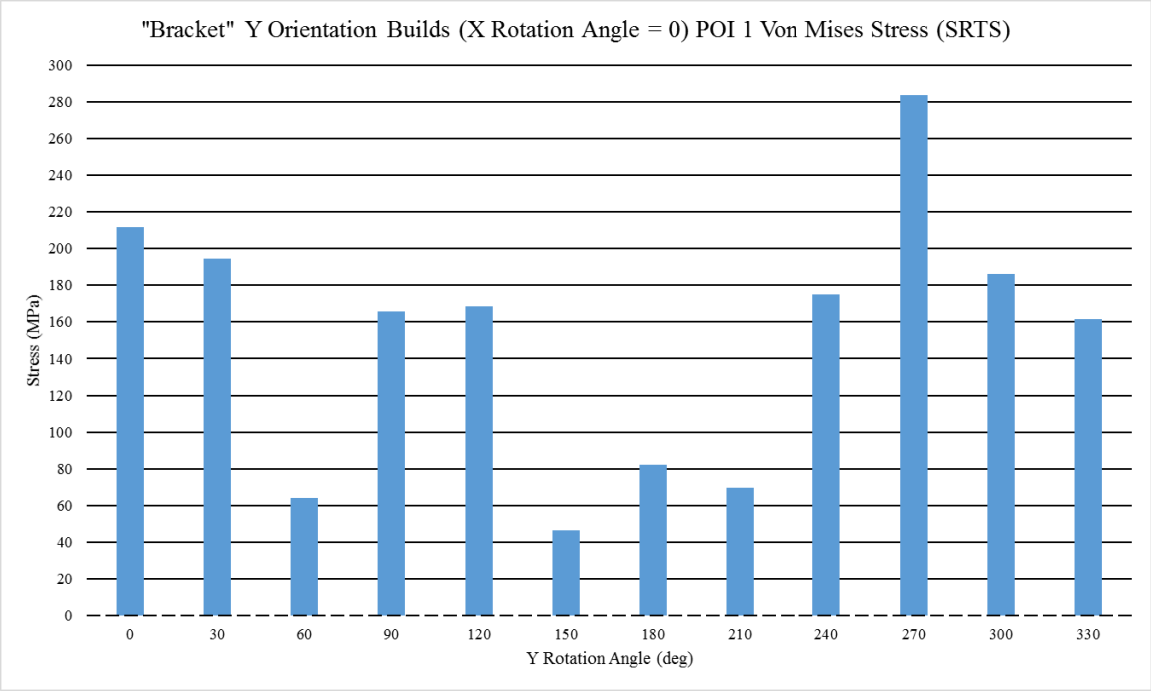

Figure 116: Von Mises stress (SRTS) plot for "Bracket" Y Orientation Builds (POI 1)

The SRTS data at POI 2 for all the orientations of the "Bracket" part build are shown in Figure 117 through Figure 120: Figure 117 is the plot for the Cauchy stress data of the X orientation builds, Figure 118 is the plot for the Von Mises stress data of the X orientation builds, Figure 119 is the plot for the Cauchy stress data of the Y, and Figure 120 is the plot for the Von Mises stress data of the Y orientation builds. Based on the aforementioned plots, the following observations were made. First, the worst orientation of the "Bracket" part orientation at POI 2 was X0Y120 with a Von Mises stress of 407.29 MPa. Second, the best orientation of the "Bracket" part at POI 2 was X210Y0 with a Von Mises stress of 15.36 MPa.

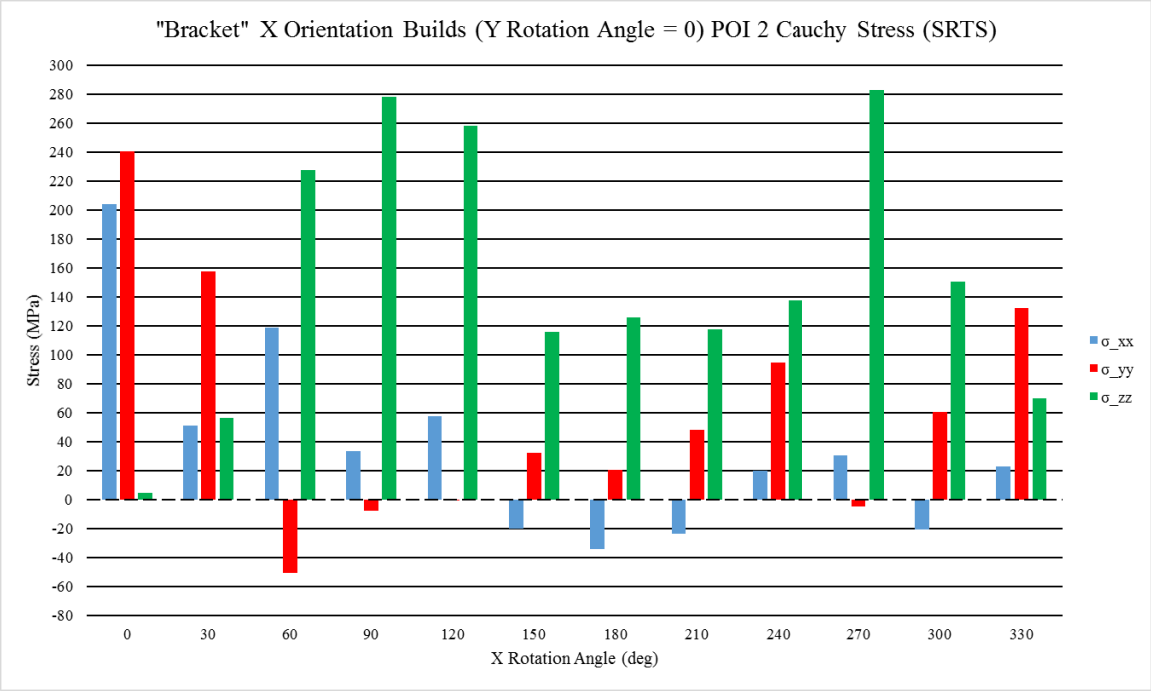

Figure 117: Cauchy stress (SRTS) plot for "Bracket" X Orientation Builds (POI 2)

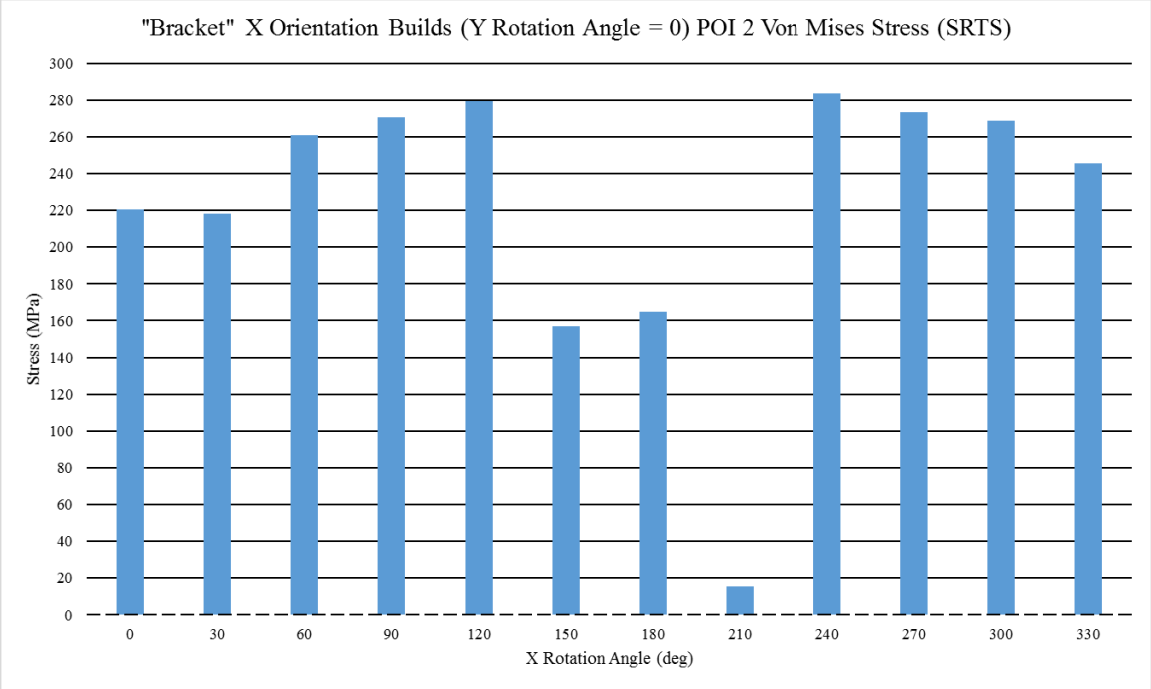

Figure 118: Von Mises stress (SRTS) plot for "Bracket" X Orientation Builds (POI 2)

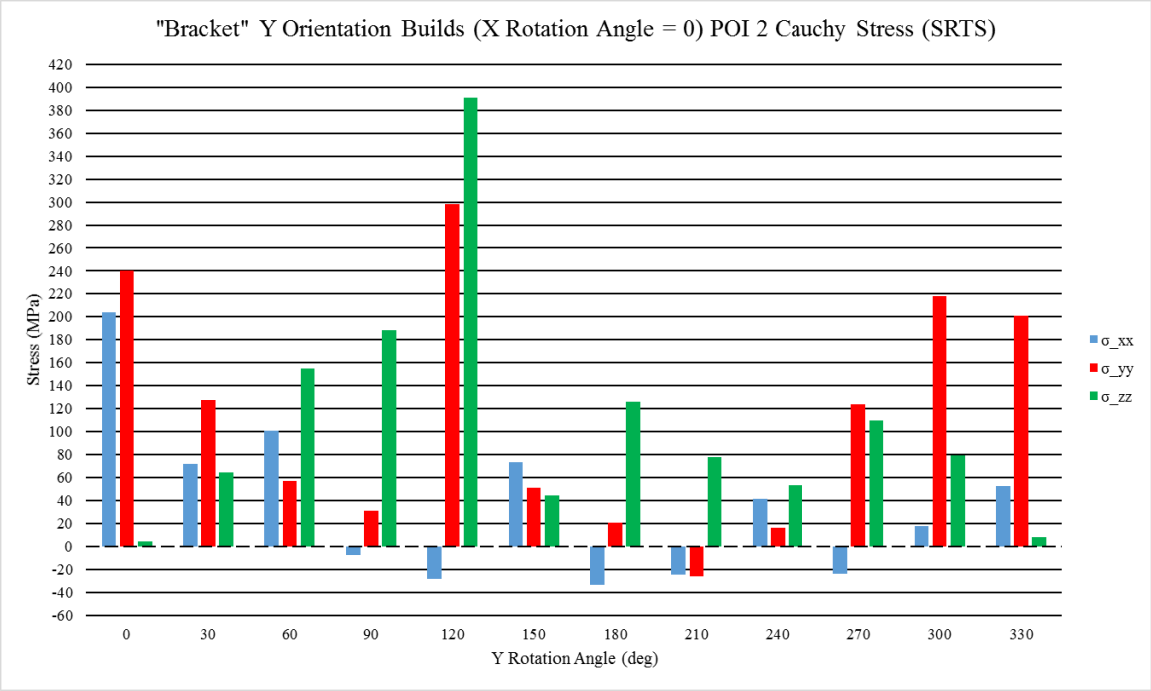

Figure 119: Cauchy stress (SRTS) plot for "Bracket" Y Orientation Builds (POI 2)

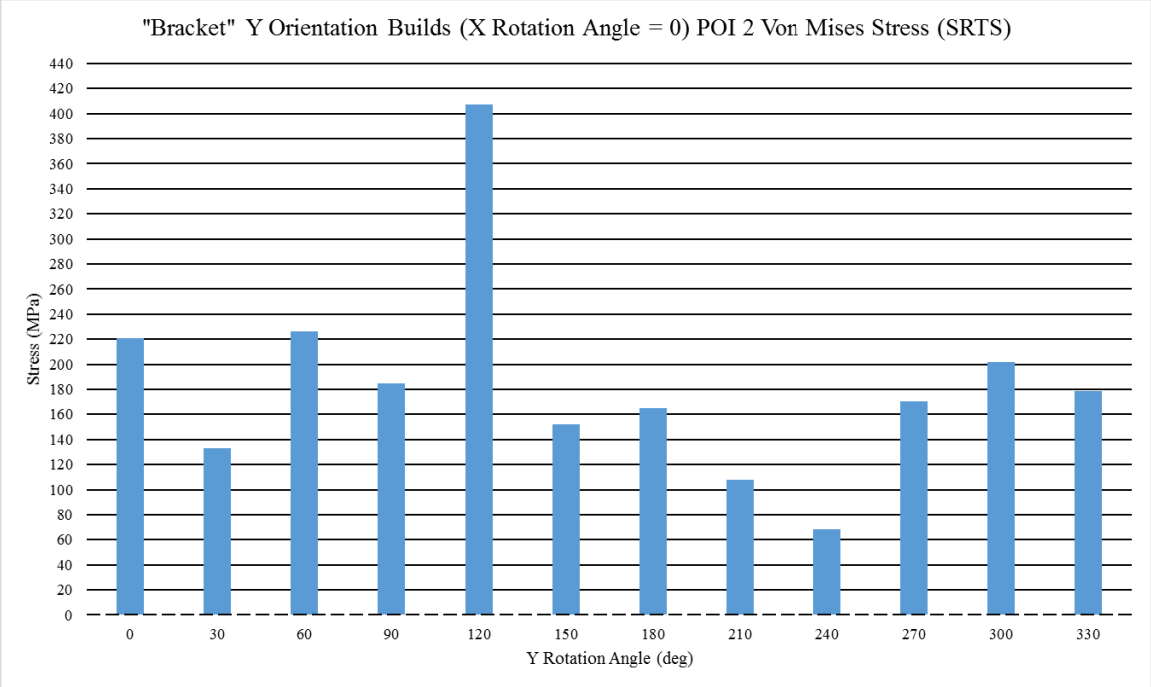

Figure 120: Von Mises stress (SRTS) plot for "Bracket" Y Orientation Builds (POI 2)

The SRTS data at POI 3 for all the orientations of the "Bracket" part build are shown in Figure 121 through Figure 124: Figure 121 is the plot for the Cauchy stress data of the X orientation builds, Figure 122 is the plot for the Von Mises stress data of the X

orientation builds, Figure 123 is the plot for the Cauchy stress data of the Y, and Figure 124 is the plot for the Von Mises stress data of the Y orientation builds. Based on the aforementioned plots, the following observations were made. First, the worst orientation of the "Bracket" part orientation at POI 3 was X0Y240 with a Von Mises stress of 340.98 MPa. Second, the best orientation of the "Bracket" part at POI 3 was X210Y0 with a Von Mises stress of 66.88 MPa.

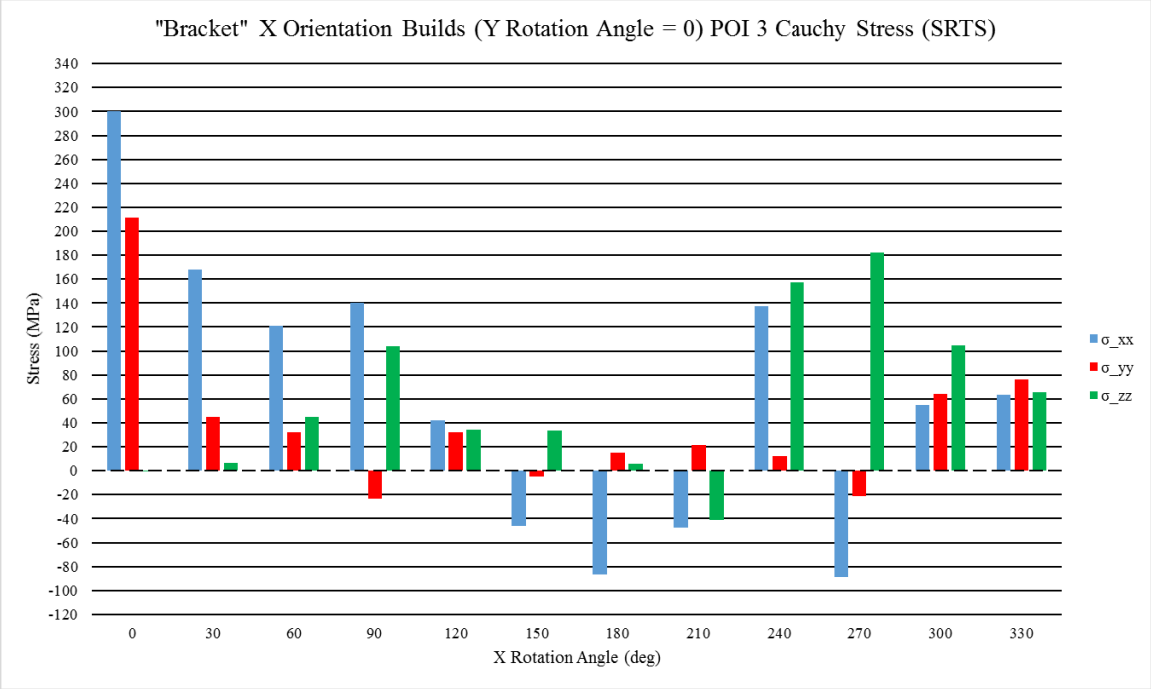

Figure 121: Cauchy stress (SRTS) plot for "Bracket" X Orientation Builds (POI 3)

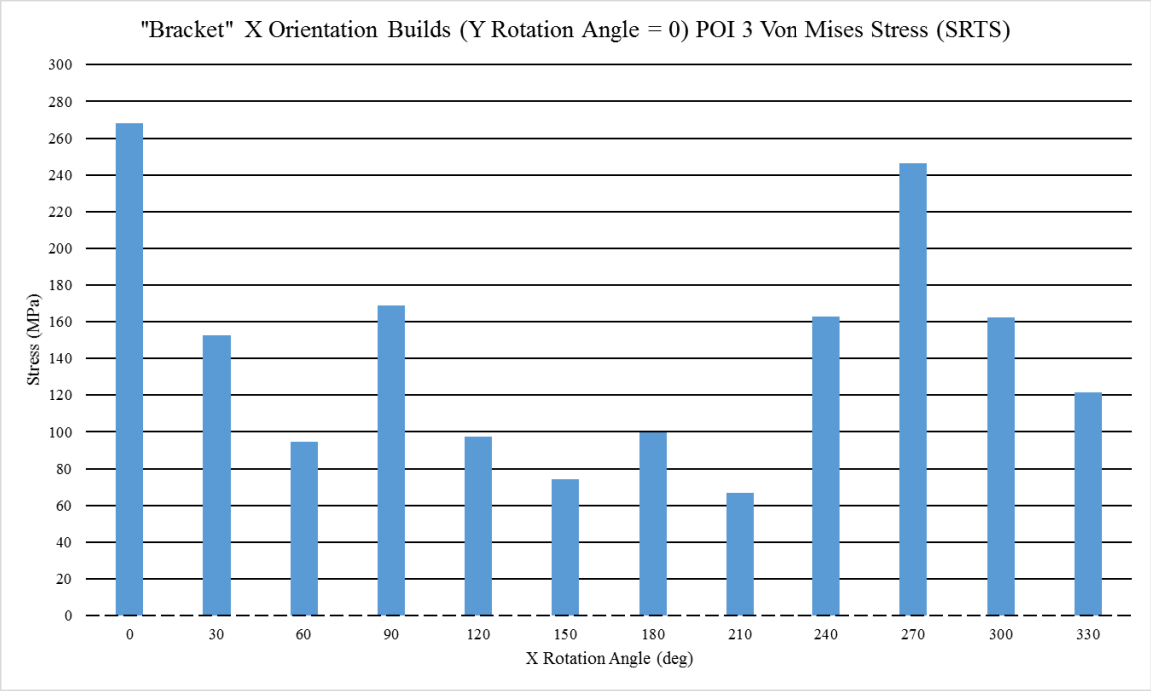

Figure 122: Von Mises stress (SRTS) plot for "Bracket" X Orientation Builds (POI 3)

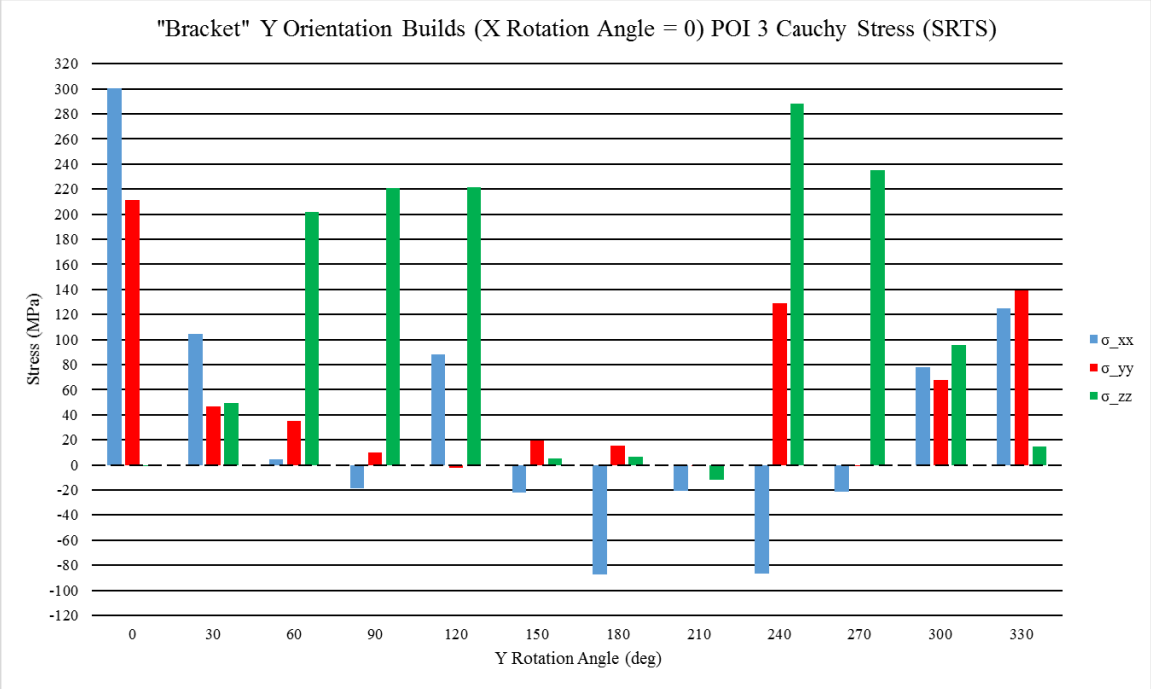

Figure 123: Cauchy stress (SRTS) plot for "Bracket" Y Orientation Builds (POI 3)

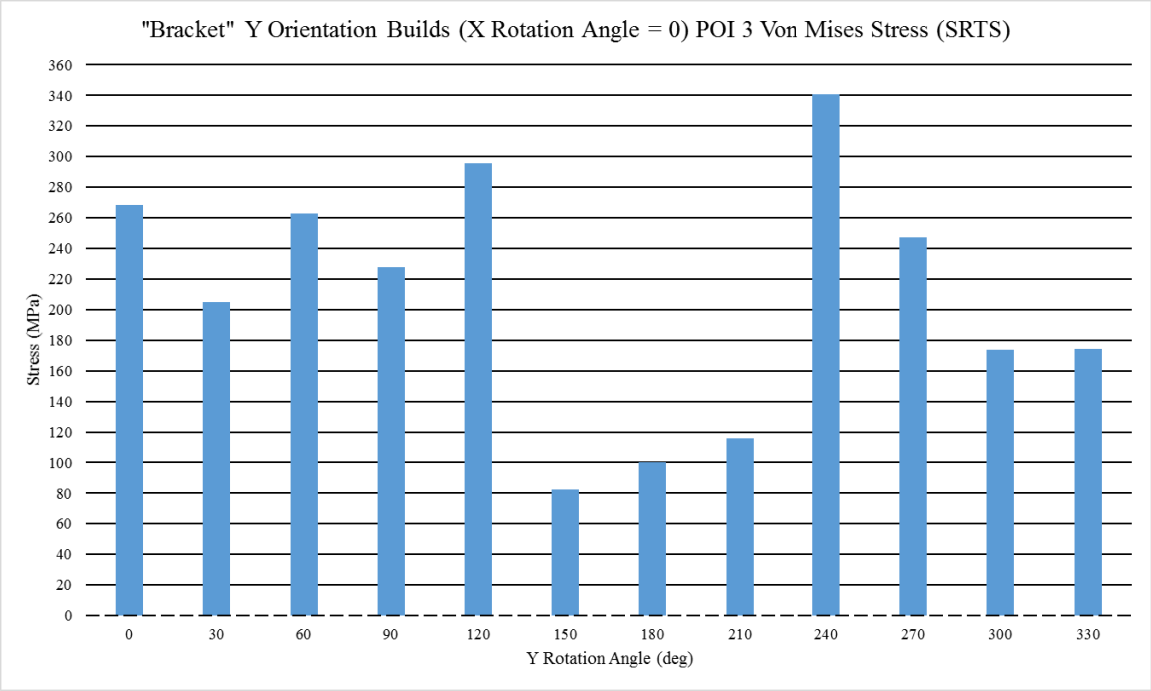

Figure 124: Von Mises stress (SRTS) plot for "Bracket" Y Orientation Builds (POI 3)

The SRTS data at POI 4 for all the orientations of the "Bracket" part build are shown in Figure 125 through Figure 128: Figure 125 is the plot for the Cauchy stress data of the X orientation builds, Figure 126 is the plot for the Von Mises stress data of the X orientation builds, Figure 127 is the plot for the Cauchy stress data of the Y, and Figure 128 is the plot for the Von Mises stress data of the Y orientation builds. Based on the aforementioned plots, the following observations were made. First, the worst orientation of the "Bracket" part orientation at POI 4 was X0Y60 with a Von Mises stress of 284.89 MPa. Second, the best orientation of the "Bracket" part at POI 4 was X180Y0 with a Von Mises stress of 63.86 MPa.

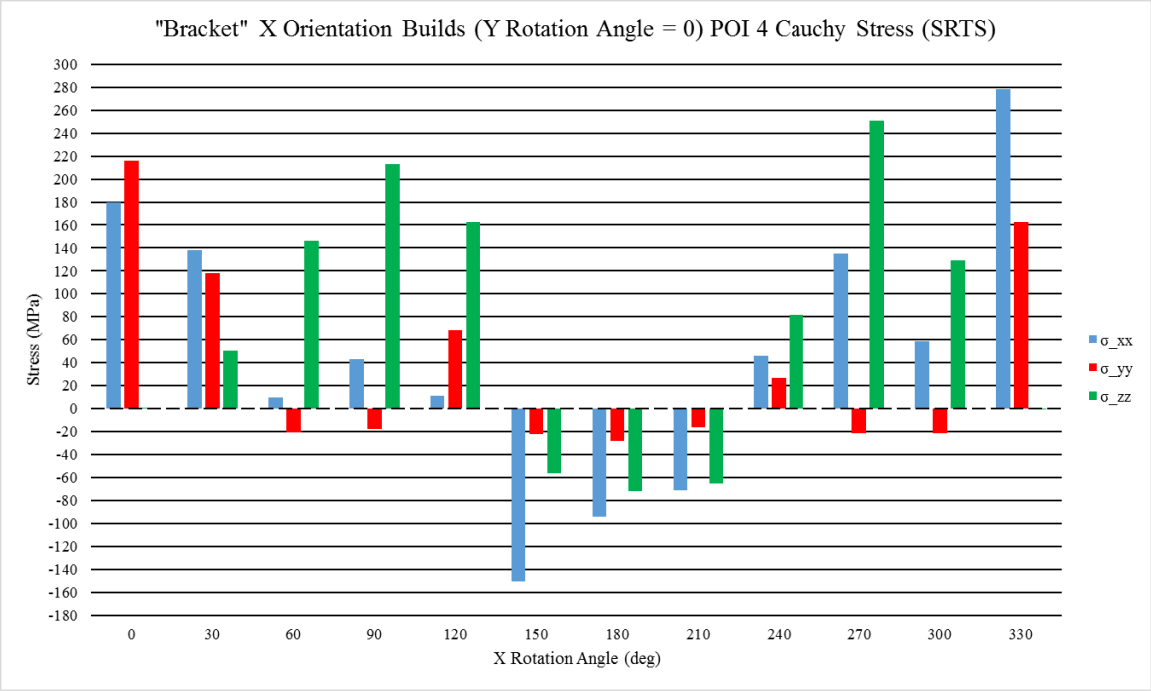

Figure 125: Cauchy stress (SRTS) plot for "Bracket" X Orientation Builds (POI 4)

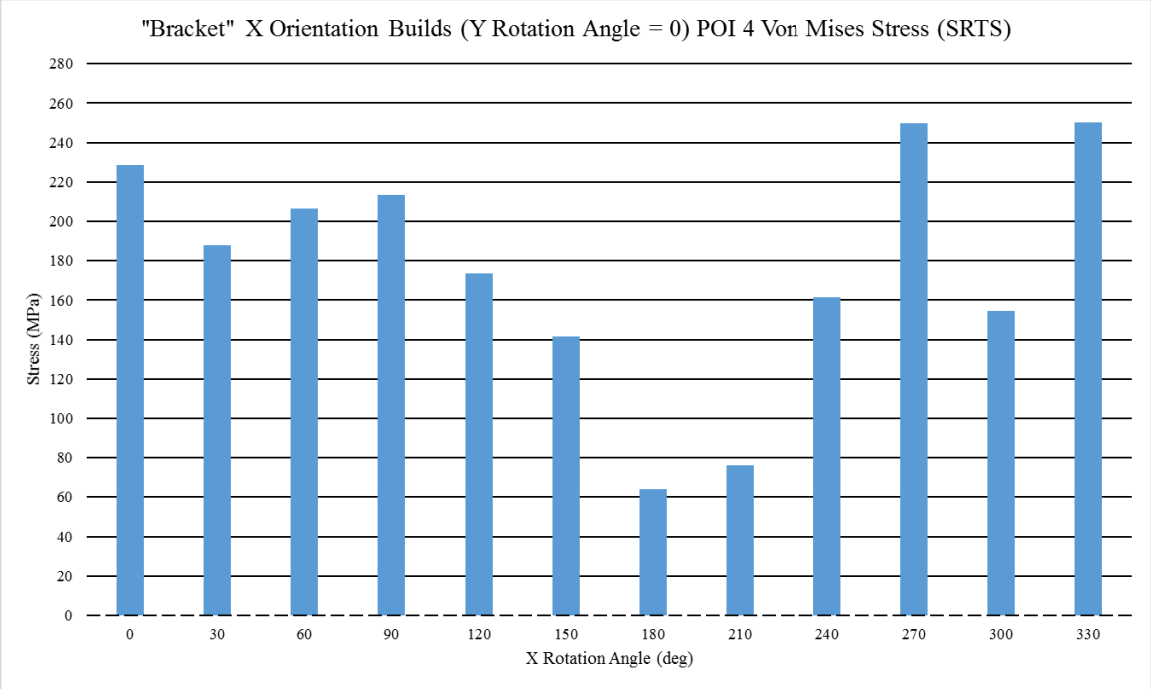

Figure 126: Von Mises stress (SRTS) plot for "Bracket" X Orientation Builds (POI 4)

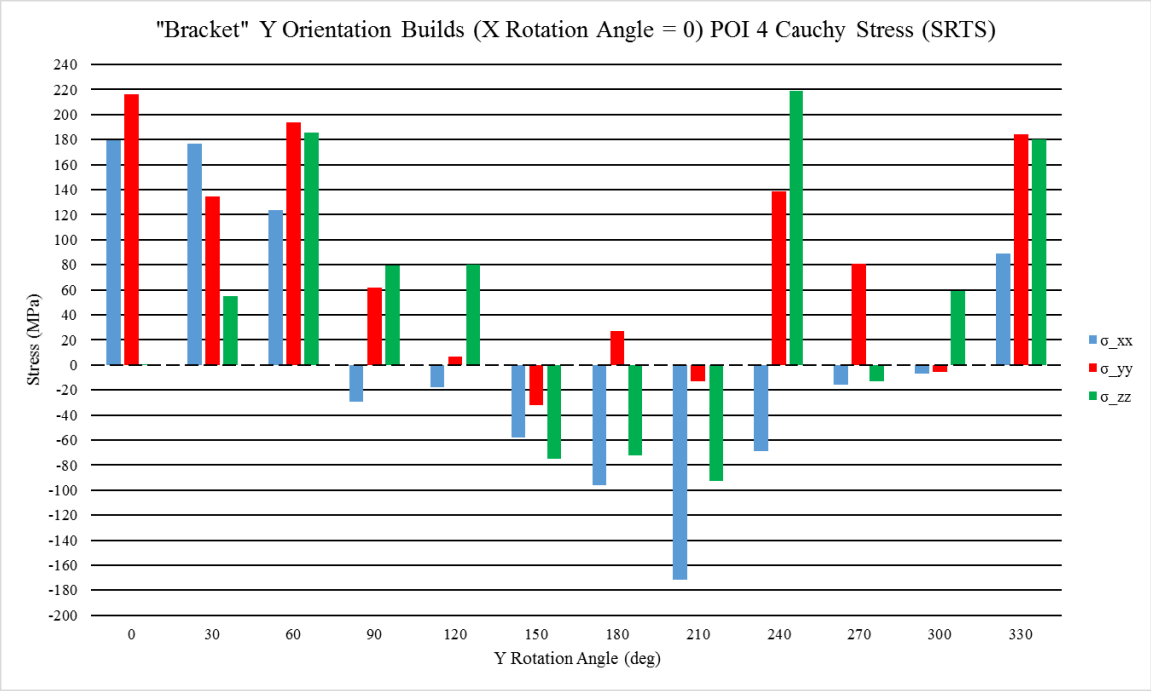

Figure 127: Cauchy stress (SRTS) plot for "Bracket" Y Orientation Builds (POI 4)

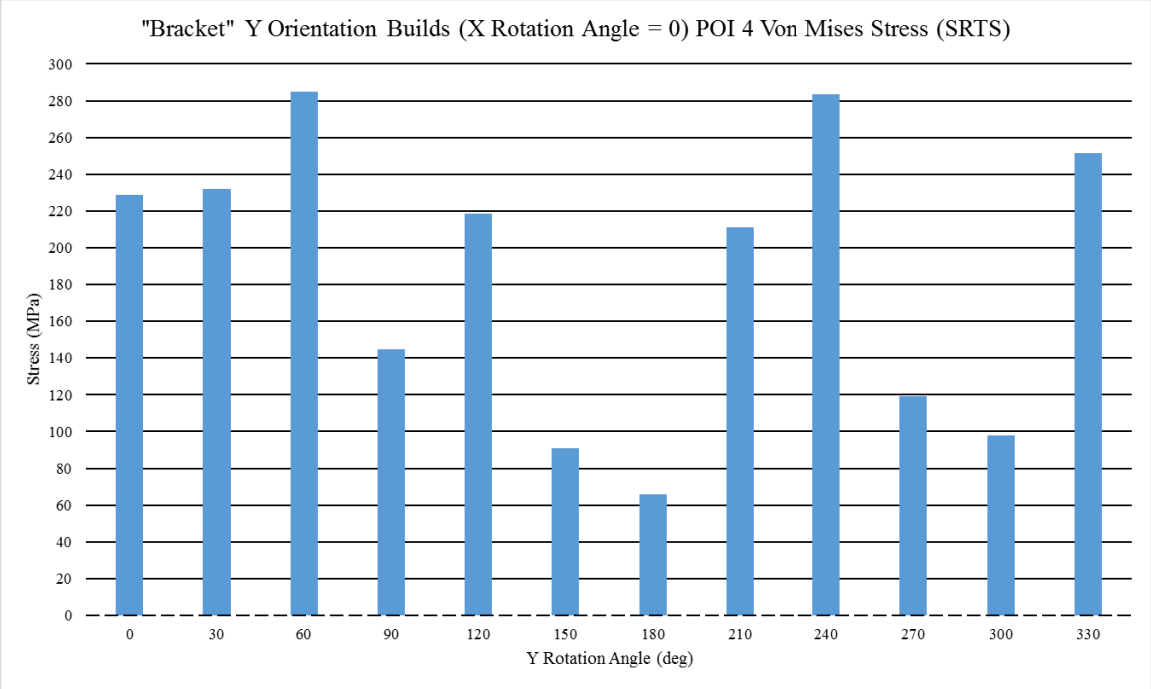

Figure 128: Von Mises stress (SRTS) plot for "Bracket" Y Orientation Builds (POI 4)

In order to determine the best orientation for the entire "Bracket" part in terms of stress at the SRTS, the following procedure was used. First, the best orientations for each POI on the "Bracket" part was found. A summary of the best orientations for each POI on

the “Bracket” part is found in Table 38. Second, for each orientation found in the previous step the Von Mises stresses of all 4 POIs were averaged, the result is shown in Table 39. Third, the minimum of the Von Mises stresses found in step two was taken as the best orientation of the entire “Bracket” part in terms of SRTS stress, and that orientation was X210Y0.

Table 38: Summary of best orientation form each "Bracket" part POI (SRTS stress)

POI #	Best Orientation	Von Mises Stress (MPa)
1	X0Y150	46.43
2	X210Y0	15.36
3	X210Y0	66.88
4	X180Y0	63.86

Table 39: Displacement magnitudes averages at each best orientation (SRTS stress)

Best Orientation	Avg VM Stress (MPa)
X0Y150	93.12
X210Y0	64.02
X210Y0	64.02
X180Y0	103.30

3.1.5: Recoater Results

The plots generated from the recoater data is shown in Figure 129 through Figure 131 below. Note that data from each simulation can come from a different time step, and the data was recorded from the same simulation as the displacement data not the FHT simulations. Because the two test builds only had one value each, the two test builds share the same plot. The value of zero for the y-axis is marked with a dotted line. Figure 129 is the plot of the MPLPD data for the two test builds, Figure 130 is the plot of the MPLPD data for the “Bracket” X orientation builds, and Figure 131 is the plot of the MPLPD data for the “Bracket” Y orientation builds. Based on the aforementioned plots, the following observations were made. First, both test builds can be predicted to print with no problem, due to the MPLPD being below the layer thickness set for the simulation which was 30 µm. This was confirmed by the fact that when they were being printed the recoater did not hit the part. Second, there were certain orientations of the “Bracket” part that would have recoater collision if printed: X120Y0, X240Y0, X300Y0, X0Y60, X0Y120, and X0Y300. Third, there a few orientations that have a probability of recoater interference but have MPLPD values less than 30 µm. This observation originated form the printing of the X60Y0 “Bracket” build. The build has a MPLPD of 28.17 µm which is less than the simulation layer thickness, and this build had recoater collision during the printing process. Therefore, for this work, it was assumed that any build that had MPLPD within 5 µm of

the layer thickness fell in this category of builds. The builds that fell into this category were X60Y0, X0Y30, and X0Y240.

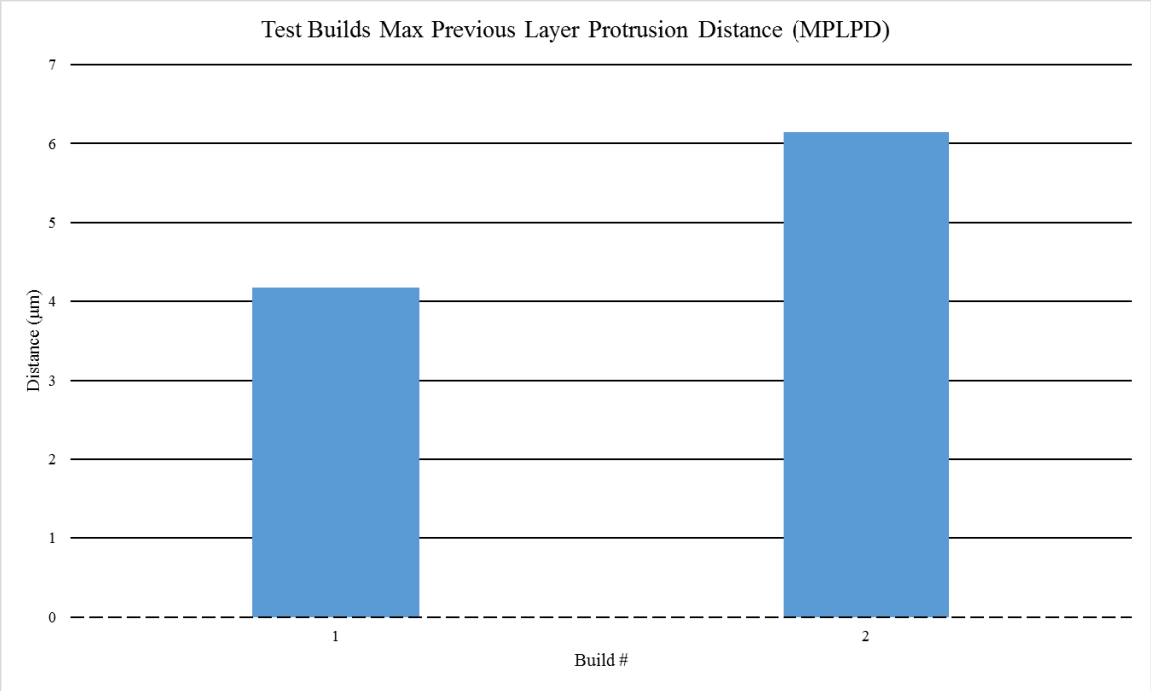

Figure 129: Recoater Plot for Test Build #1 & 2

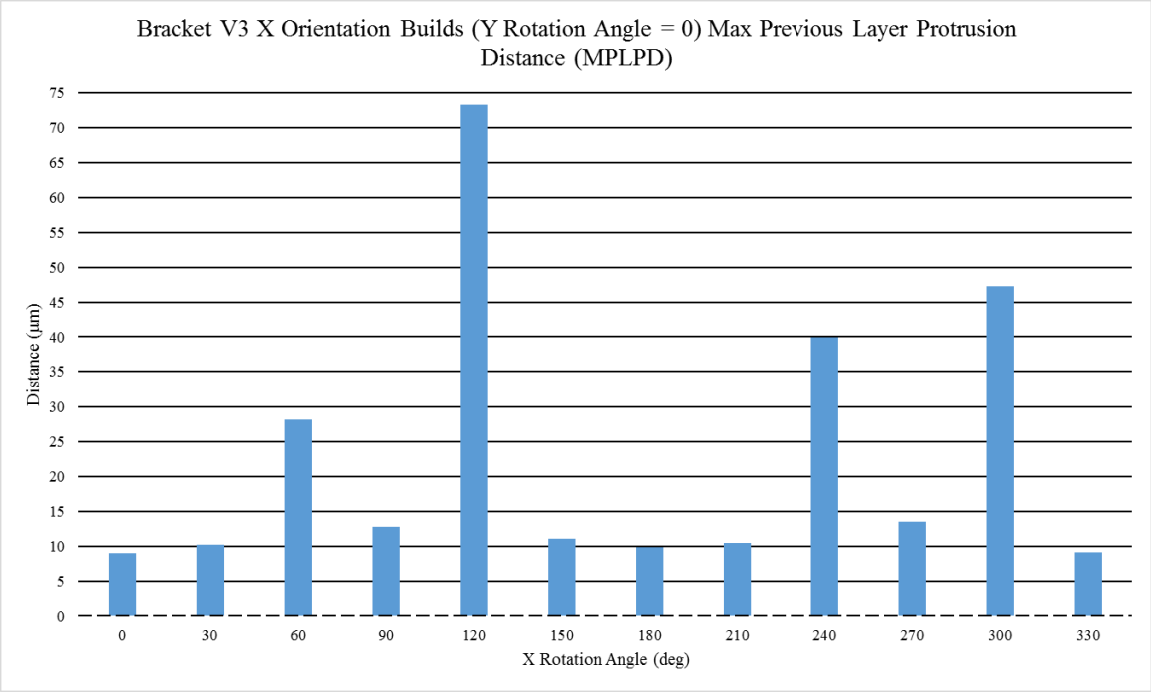

Figure 130: Recoater Plot for "Bracket" X Orientation Builds

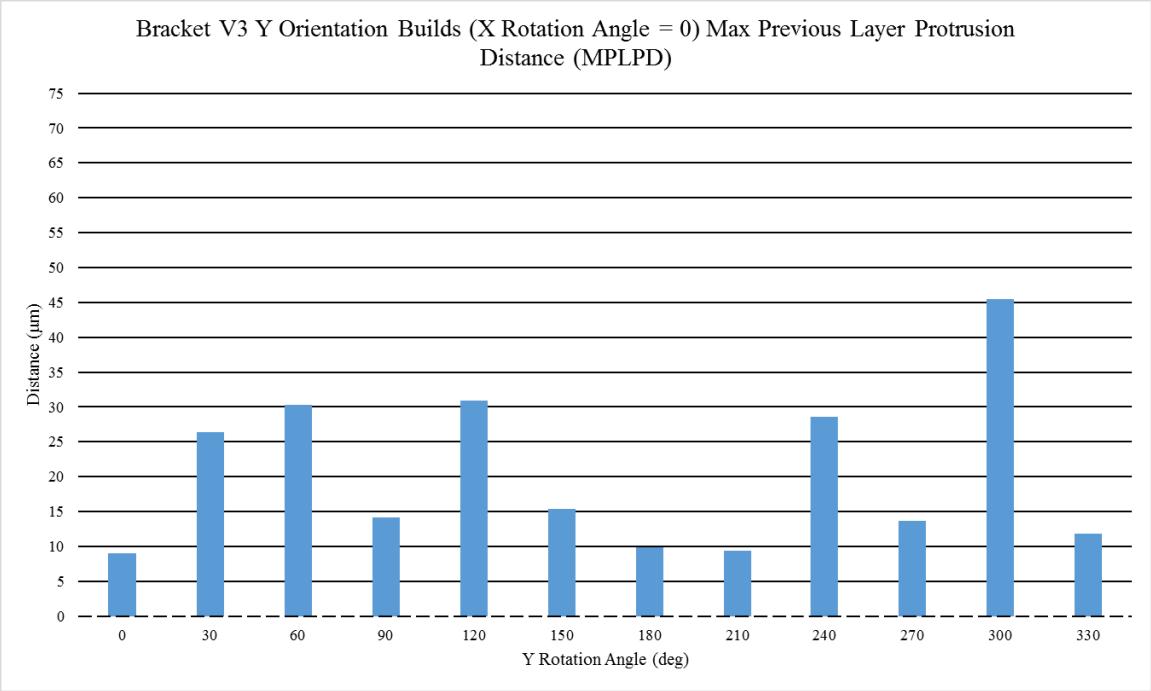

Figure 131: Recoater Plot for "Bracket" Y Orientation Builds

3.2: Measurement Results

Using the methods described in Section 2.3.1 through Section 2.3.3, the results of this work's measurements along with a discussion of those results are presented in Sections 3.2.1 through 3.2.2. Due to time constraints, the measurements were not taken of the printed builds after build plate removal as planned, therefore there was not any SRTS data collected.

3.2.1: Measured Results: PTS

The measured and simulation gap distance data at the PTS were placed on plots as shown in Figure 132 through Figure 136. To compensate for the 200 micron resolution of the scanner the measured results have a ± 100 micron tolerance placed on them, and this shown by the error bars on each plot. The measured results for the X0Y90 "Bracket" build at POI 2 were not available due scanning issues. The value of zero for the y-axis is marked with a dotted line. The y-axis resolution was kept the same across all plots. Figure 132 is the plot of the gap distance data for Test Build #2, Figure 133 is the plot of the gap distance data for the printed "Bracket" builds at POI 1, Figure 134 is the plot of the gap distance data for the printed "Bracket" builds at POI 2, Figure 135 is the plot of the gap distance data for the printed "Bracket" builds at POI 3, and Figure 136 is the plot of the gap distance data for the printed "Bracket" builds at POI 4. The following observations were made from the data. First, the results for Test Build #2 are inconclusive. All the simulation gap

distances are within tolerance of the measured results for Test Build #2, and this indicates that there is a possibly that the results agrees with each other. However, the overall trend of the simulation results does not match the measured results very well which means so that the results may not agree with each other. Second, the simulations and measured results show a high possibility of agreeing for the printed "Bracket" builds for POI 1. The trends of the simulation and measured results match each other well, and only one of the three simulation results being outside tolerance. Third, the results for printed "Bracket" builds for POI 2 do not agree, because the simulation results are not with tolerance of the measured results and the trends do not line up. Fourth, for POIs 3 and 4 on the "Bracket", the results are inconclusive.

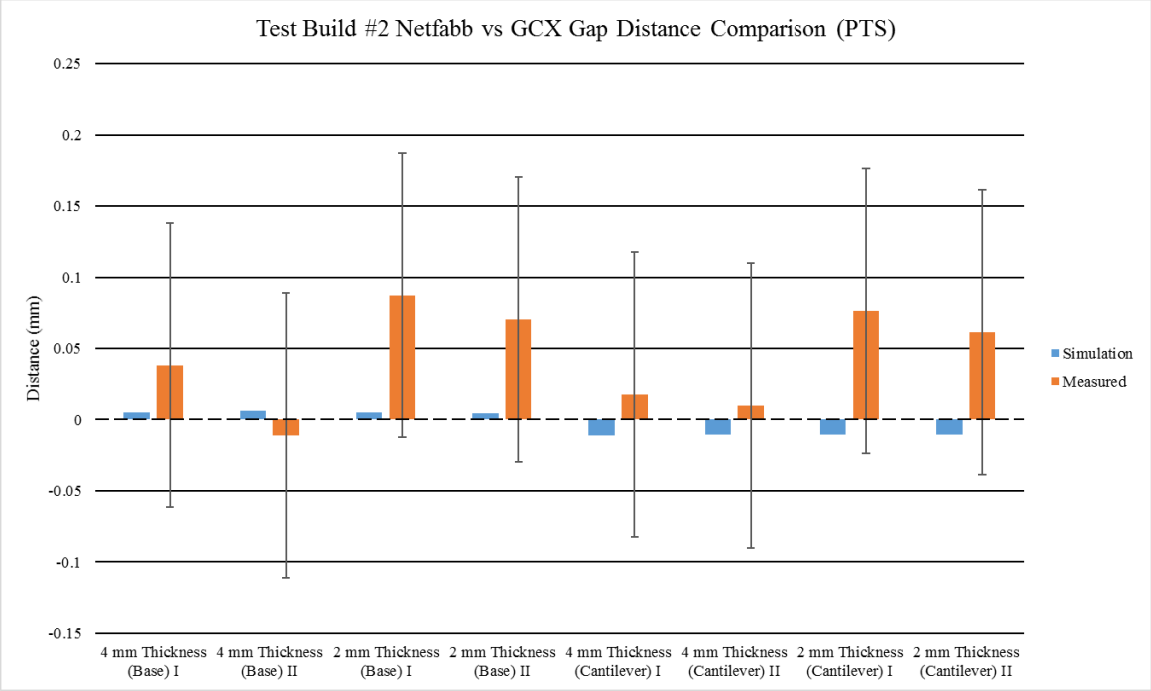

Figure 132: Simulation vs. measured results (PTS) plot for Test Build #2

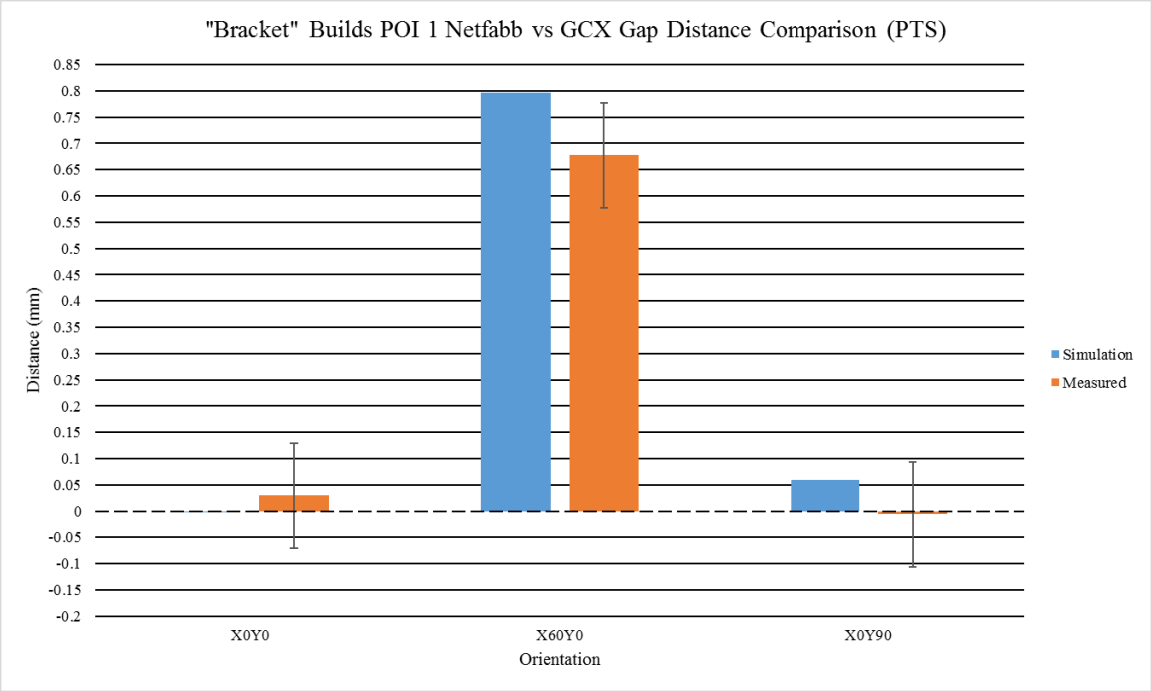

Figure 133: Simulation vs. measured results (PTS) plot for the printed "Bracket" builds (POI 1)

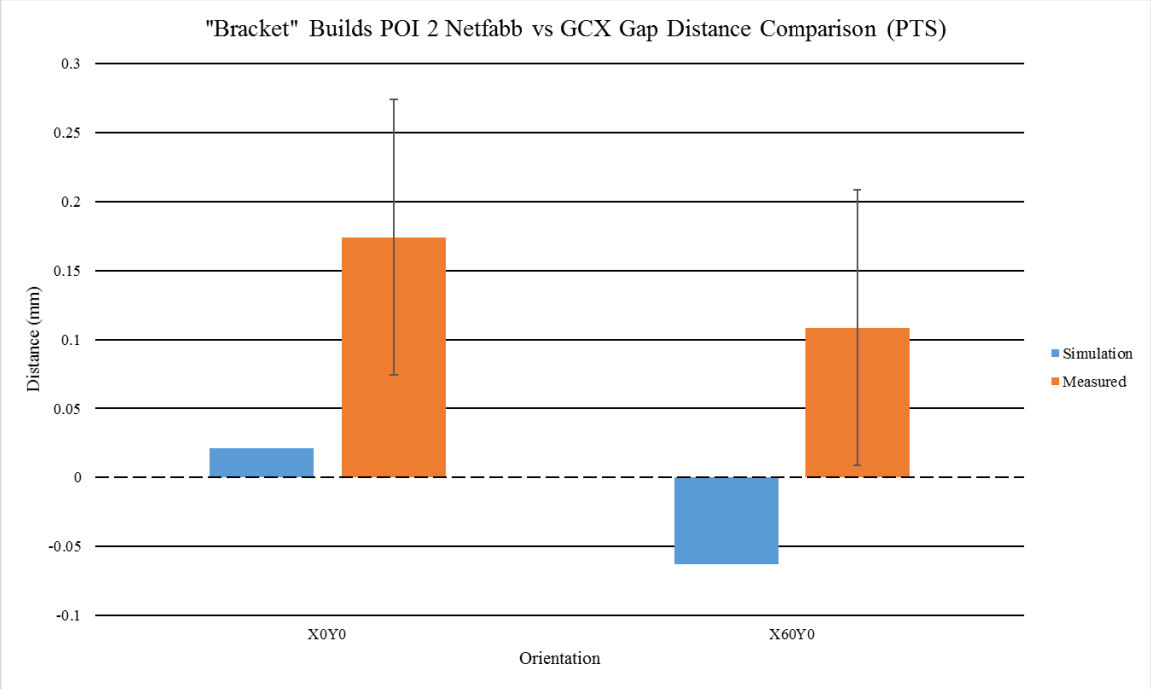

Figure 134: Simulation vs. measured results (PTS) plot for the printed "Bracket" builds (POI 2)

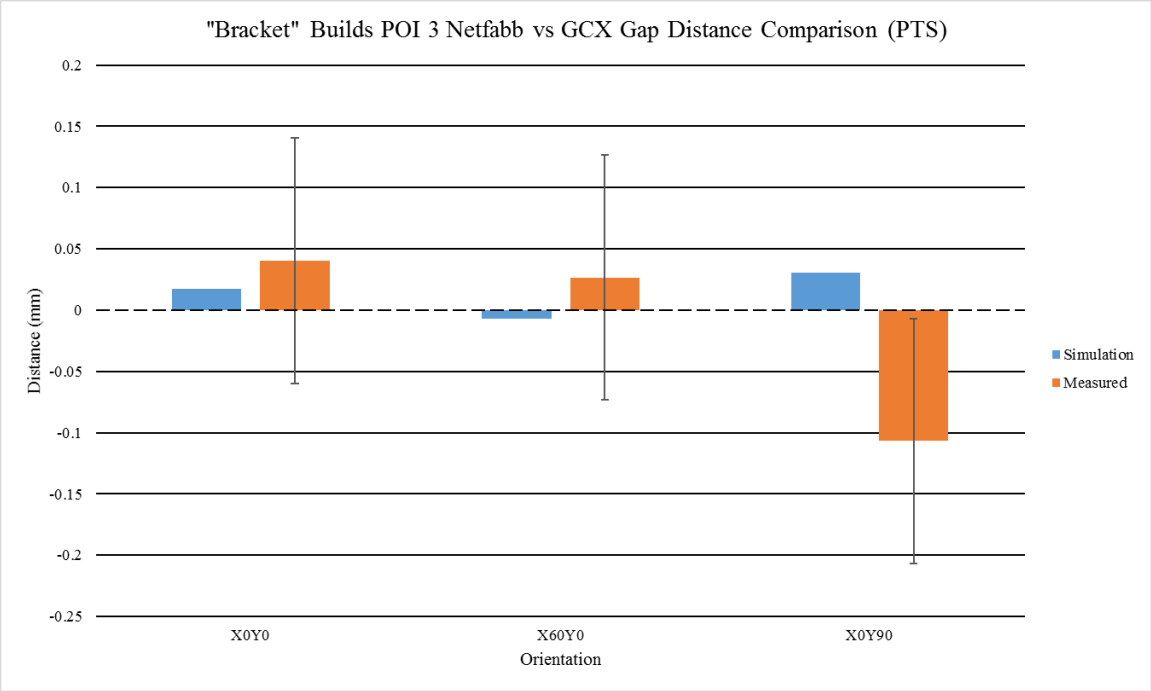

Figure 135: Simulation vs. measured results (PTS) plot for the printed "Bracket" builds (POI 3)

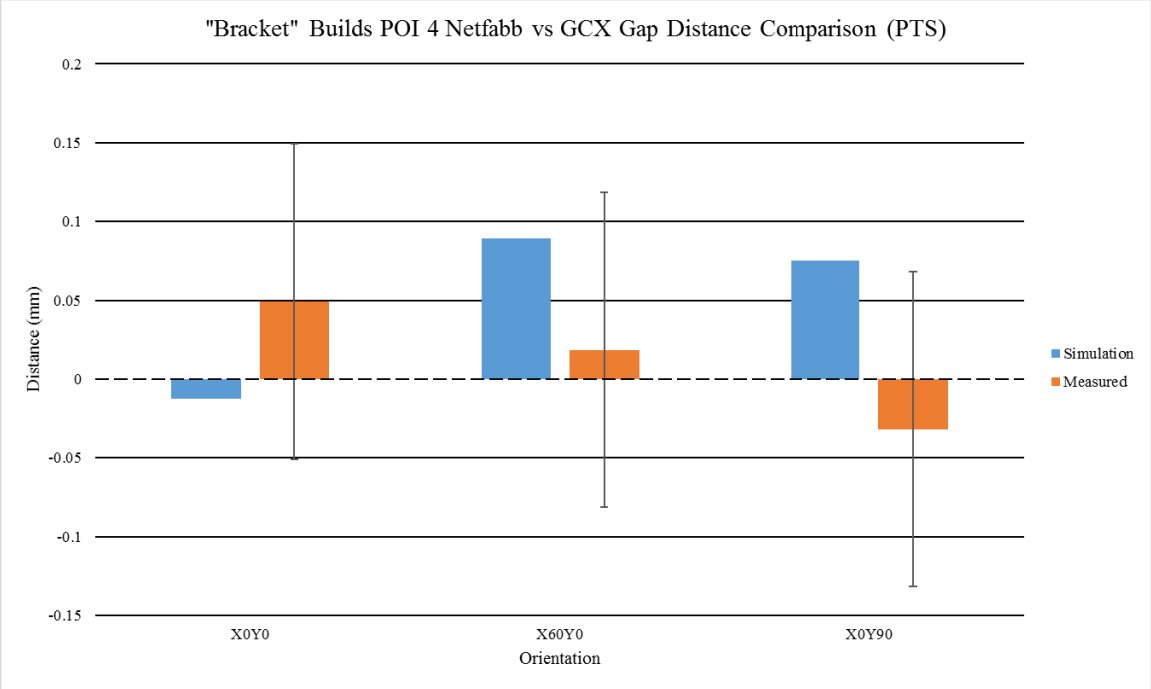

Figure 136: Simulation vs. measured results (PTS) plot for the printed "Bracket" builds (POI 4)

3.2.2: Error Analysis: PTS

The results for the gap distance percentage error calculations are shown in Table 40 through Table 44. Due the existence of the tolerance in the measured data (see Section 3.2.1), the maximum and minimum percentage error values calculated for each simulation gap distance. The calculation procedure was as follows. First, Equations (2-25) and (2-26) were used to calculate the gap distance percentage error on the upper and lower bounds of each measured data point. Second, the absolute value was taken of the percentage errors found in step one. Third, the minimum error was found. For the simulation gap distance values that were within the tolerance of the measured values, the minimum error was given a value of zero. For all other simulation values, the minimum of the values found in step two was used. Forth, the maximum values were found by taken the maximum of the values found in step two.

Table 40 shows the minimum and maximum errors at each POI for Test Build #2, Table 41 shows the minimum and maximum errors at each orientation at POI 1, Table 42 shows the minimum and maximum errors at each orientation at POI 2, Table 43 shows the minimum and maximum errors at each orientation at POI 3, and Table 44 shows the minimum and maximum errors at each orientation at POI 4. The following observations were made from the data. First, the data points with smaller simulated and measured gap distances tended to have lager errors. Second, the data point with the smallest maximum error was the X60Y0 “Bracket” at POI 1. Third, the data point with largest maximum error was at the same POI but at the X0Y0 “Bracket”. Fourth, the error ranges at each data point are quite large.

Table 40: Min and max gap distance percentage error (PTS) for each POI for Test Build #2

POI #	Min Gap Distance Percentage Error	Max Gap Distance Percentage Error
1	0%	2516.46%
2	0%	1259.65%
3	0%	3543.75%
4	0%	3532.33%
5	0%	648.00%
6	0%	772.62%
7	0%	126.97%
8	0%	263.09%

Table 41: Min and max gap distance percentage error (PTS) for each printed “Bracket” build at POI 1

Orientation	Min Gap Distance Percentage Error	Max Gap Distance Percentage Error
X0Y0	0%	10725.57%
X60Y0	2.40%	27.51%
X0Y90	0%	276.22%

Table 42: Min and max gap distance percentage error (PTS) for each printed "Bracket" build at POI 2

Orientation	Min Gap Distance Percentage Error	Max Gap Distance Percentage Error
X0Y0	246.39%	1180.07%
X60Y0	113.75%	430.21%

Table 43: Min and max gap distance percentage error (PTS) for each printed "Bracket" build at POI 3

Orientation	Min Gap Distance Percentage Error	Max Gap Distance Percentage Error
X0Y0	0%	711.59%
X60Y0	0%	1872.11%
X0Y90	446.17%	771.22%

Table 44: Min and max gap distance percentage error (PTS) for each printed "Bracket" build at POI 4

Orientation	Min Gap Distance Percentage Error	Max Gap Distance Percentage Error
X0Y0	0%	1297.66%
X60Y0	0%	191.30%
X0Y90	9.17%	275.54%

There were plenty sources of error within this work. First, there some of the simulation process parameters there were different then the parameters that were used when the builds were printed. Second, the scanning resolution was too large to measure some of the smaller distortions. Third, there were slight differences between the placement of the cantilevers in Test Builds #1 and #2 between the simulation and the printed builds. Fourth, the manual nature of the scanning process introduces human error into measured results.

CHAPTER 4 :
CONCLUSIONS AND FUTURE WORK

4.1: Conclusions

The use of simulation tools in order to find the optimal orientation of additive manufactured parts has been demonstrated and validated. The simulation tool that was used in this work was Autodesk Netfabb simulation utility. Netfabb was used to simulation a total of 25 different builds: 2 test cantilever builds and 23 different orientations of a more complex part. The orientations used were: counter-clockwise rotations about the x-axis in 30-degree increments from 0 to 330 degrees while having no rotations about the y and z axis, and counter-clockwise rotations about the y-axis in 30-degree increments from 0 to 330 degrees while having no rotations about the x and z axis. The complex part used for this work was the "Bracket" part. Both cantilever builds and the three orientations of the "Bracket" part were printed in order to be used to validate the 25 build simulations. The verification involved the 3D scanning of the printed builds and the use of Geomagic Control X software in order to measure the distortions and then comparing those distortions against the simulation distortions. The optimal orientation was selected based on three criteria: distortion, stress, and printability. For the distortion and stress criteria, a four points on the complex part were selected to be averaged. For the printability criteria, recoater clearance information that was provided by the software was examined. Also, all three of those criteria were examined before and after the substrate was removed. From this work, the following conclusions were made. First, the optimal orientation for the "Bracket" part was different for each of the three criteria. Therefore, the selection of the best orientation must also be made based on the application of the part. Second, the measurement methodology used for validation was very flawed. This was due to the relatively high tolerance introduced by the scanning, and the fact that measuring distortions on parts before substrate removal is not optimal. Third, geometry of part as well as the placement of the supports on the part have large impacts on stress and distortion. Overall, this work demonstrated the use of simulation tools to predict residual stresses and during laser powder bed fusion. This work also showed the importance of part geometry and functionality in controlling the stress and distortions within the part.

4.2: Future Work

In order to expand upon this work, the following is suggested. First, select more points on the "Bracket" part. This will allow a more accurate section of the best ordination. Second, preforming a validation on the stresses in the simulations. This will provide additional validation of the simulations. Third, perform the mentioned measurement procedure on the printed builds after the substrate removal. This will provide more conclusive distortion measurement validation. Fourth, study different support designs for

the “Bracket” part, in order to further optimize the part. Fifth, apply the methodology presented in this work using different complex geometries and/or different test geometries.

BIBLIOGRAPHY

[1] Gouge, Michael, and Pan Michaleris. "An Introduction to Additive Manufacturing Processes and Their Modeling Challenges." In *Thermo-Mechanical Modeling of Additive Manufacturing*, pp. 3-18. Butterworth-Heinemann, 2018.

[2] Lam, Christopher Xu Fu, X. M. Mo, Swee-Hin Teoh, and D. W. Hutmacher. "Scaffold development using 3D printing with a starch-based polymer." *Materials Science and Engineering: C* 20, no. 1-2 (2002): 49-56. doi: 10.1016/S0928-4931(02)00012-7

[3] Chen, Zhangwei, Ziyong Li, Junjie Li, Chengbo Liu, Changyong Liu, Yang Li, Pei Wang, He Yi, Changshi Lao, and Fu Yuelong. "3D printing of ceramics: a review." *Journal of the European Ceramic Society* (2018). doi: 10.1016/j.jeurceramsoc.2018.11.013

[4] Martin, John H., Brennan D. Yahata, Jacob M. Hundley, Justin A. Mayer, Tobias A. Schaedler, and Tresa M. Pollock. "3D printing of high-strength aluminum alloys." *Nature* 549, no. 7672 (2017): 365. doi: 10.1038/nature23894

[5] Trombetta, Ryan, Jason A. Inzana, Edward M. Schwarz, Stephen L. Kates, and Hani A. Awad. "3D printing of calcium phosphate ceramics for bone tissue engineering and drug delivery." *Annals of biomedical engineering* 45, no. 1 (2017): 23-44. doi: 10.1007/s10439-016-1678-3

[6] Ueda, Yukio, Eiji Takahashi, Keiji Fukuda, Koichi Sakamoto, and Keiji Nakacho. "Multi-pass welding stresses in very thick plates and their reduction from stress relief annealing." *Transactions of JWRI* 5, no. 2 (1976): 179-189.

[7] Nickell, Robert E., and Hugh D. Hibbitt. "Thermal and mechanical analysis of welded structures." *Nuclear Engineering and Design* 32, no. 1 (1975): 110-120. doi: 10.1016/0029-5493(75)90093-X

[8] Carroll, Beth E., Todd A. Palmer, and Allison M. Beese. "Anisotropic tensile behavior of Ti–6Al–4V components fabricated with directed energy deposition additive manufacturing." *Acta Materialia* 87 (2015): 309-320. doi: 10.1016/j.actamat.2014.12.054

[9] Denlinger, Erik R., Michael Gouge, Jeff Irwin, and Pan Michaleris. "Thermomechanical model development and in situ experimental validation of the Laser Powder-Bed Fusion process." *Additive Manufacturing* 16 (2017): 73-80. doi: 10.1016/j.addma.2017.05.001

[10] Ueda, Yukio, Eiji Takahashi, Keiji Fukuda, and Keiji Nakacho. "Transient and residual stresses in multi-pass welds." *Transactions of JWRI* 3, no. 1 (1974): 59-67.

[11] Ueda, Yukio, and Keiji Nakacho. "Simplifying methods for analysis of transient and residual stresses and deformations due to multi-pass welding (welding mechanics, strength, and design)." *Transactions of JWRI* 11, no. 1 (1982): 95-103.

[12] Lindgren, Lars-Erik, Henrik Runnemalm, and Mats O. Näsström. "Simulation of multi-pass welding of a thick plate." *International journal for numerical methods in engineering* 44, no. 9 (1999): 1301-1316. doi: 10.1002/(SICI)1097-0207(19990330)44:9<1301::AID-NME479>3.0.CO;2-K

[13] Brickstad, Björn, and B. L. Josefson. "A parametric study of residual stresses in multi-pass butt-welded stainless-steel pipes." *International Journal of Pressure Vessels and Piping* 75, no. 1 (1998): 11-25. doi: 10.1016/S0308-0161(97)00117-8

[14] Heinze, Christoph, Christopher Schwenk, and Michael Rethmeier. "Numerical calculation of residual stress development of multi-pass gas metal arc welding." *Journal of Constructional Steel Research* 72 (2012): 12-19. doi: 10.1016/j.jcsr.2011.08.011

[15] Mirshekari, G. R., E. Tavakoli, M. Atapour, and B. Sadeghian. "Microstructure and corrosion behavior of multi-pass gas tungsten arc welded 304L stainless steel." *Materials & Design* 55 (2014): 905-911. doi: 10.1016/j.matdes.2013.10.064

[16] Zhang, Zhiqiang, Hongyang Jing, Lianyong Xu, Yongdian Han, and Lei Zhao. "Investigation on microstructure evolution and properties of duplex stainless steel joint multi-pass welded by using different methods." *Materials & Design* 109 (2016): 670-685. doi: 10.1016/j.matdes.2016.07.110

[17] Kolhe, Kishor P., and C. K. Datta. "Prediction of microstructure and mechanical properties of multi-pass SAW." *Journal of materials processing technology* 197, no. 1-3 (2008): 241-249. doi: 10.1016/j.jmatprotec.2007.06.066

[18] Kar, A., and J. Mazumder. "One-dimensional diffusion model for extended solid solution in laser cladding." *Journal of applied physics* 61, no. 7 (1987): 2645-2655. doi: 10.1063/1.337895

[19] Keist, Jayme S., and Todd A. Palmer. "Role of geometry on properties of additively manufactured Ti-6Al-4V structures fabricated using laser based directed energy deposition." *Materials & Design* 106 (2016): 482-494. doi: 10.1016/j.matdes.2016.05.045

[20] Al-Bermani, S. S., M. L. Blackmore, W. Zhang, and I. Todd. "The origin of microstructural diversity, texture, and mechanical properties in electron beam melted Ti-6Al-4V." *Metallurgical and materials transactions a* 41, no. 13 (2010): 3422-3434. doi: 10.1007/s11661-010-0397-x

[21] Zheng, B., Y. Zhou, J. E. Smugeresky, J. M. Schoenung, and E. J. Lavernia. "Thermal behavior and microstructure evolution during laser deposition with laser-engineered net shaping: part II. Experimental investigation and discussion." *Metallurgical and materials transactions A* 39, no. 9 (2008): 2237-2245. doi: 10.1007/s11661-008-9566-6

[22] Denlinger, Erik R., Jarred C. Heigel, and Panagiotis Michaleris. "Residual stress and distortion modeling of electron beam direct manufacturing Ti-6Al-4V." *Proceedings of the Institution of Mechanical Engineers, Part B: Journal of Engineering Manufacture* 229, no. 10 (2015): 1803-1813. doi: 10.1177/0954405414539494

[23] Anca, Andrés, Víctor D. Fachinotti, Gustavo Escobar-Palafox, and Alberto Cardona. "Computational modelling of shaped metal deposition." *International journal for numerical methods in engineering* 85, no. 1 (2011): 84-106. doi: 10.1002/nme.2959

[24] Gibson, Ian, David Rosen, and Brent Stucker. "Directed energy deposition processes." In Additive Manufacturing Technologies, pp. 245-268. Springer, New York, NY, 2015.

[25] Wang, Liang, and Sergio Felicelli. "Analysis of thermal phenomena in LENS™ deposition." *Materials Science and Engineering: A* 435 (2006): 625-631. doi: 10.1016/j.msea.2006.07.087

[26] Peyre, P., P. Aubry, R. Fabbro, R. Neveu, and Arnaud Longuet. "Analytical and numerical modelling of the direct metal deposition laser process." *Journal of Physics D: Applied Physics* 41, no. 2 (2008): 025403. doi: 10.1088/0022-3727/41/2/025403

[27] Griffith, M. L., M. E. Schlienger, L. D. Harwell, M. S. Oliver, M. D. Baldwin, M. T. Ensz, M. Essien *et al.* "Understanding thermal behavior in the

LENS process." *Materials & design* 20, no. 2-3 (1999): 107-113. doi: 10.1016/S0261-3069(99)00016-3

[28] Keicher, Dave M., and John E. Smugeresky. "The laser forming of metallic components using particulate materials." *Jom* 49, no. 5 (1997): 51-54. doi: 10.1007/BF02914686

[29] Keicher, David M., John E. Smugeresky, Joseph A. Romero, Michelle L. Griffith, and Lane D. Harwell. "Using the laser engineered net shaping (LENS) process to produce complex components from a CAD solid model." In *Lasers as Tools for Manufacturing II*, vol. 2993, pp. 91-97. International Society for Optics and Photonics, 1997. doi: 10.1117/12.270018

[30] Ensz, Mark, Michelle Griffith, William Hofmeister, Joel A. Philliber, John Smugeresky, and Melissa Wert. *Investigation of solidification in the laser engineered net shaping (LENS) process*. No. SAND--99-1550J. Sandia National Laboratories (SNL), 1999.

[31] Kruth, J-P., Ming-Chuan Leu, and Terunaga Nakagawa. "Progress in additive manufacturing and rapid prototyping." *Cirp Annals* 47, no. 2 (1998): 525-540. doi: 10.1016/S0007-8506(07)63240-5

[32] Levy, Gideon N., Ralf Schindel, and Jean-Pierre Kruth. "Rapid manufacturing and rapid tooling with layer manufacturing (LM) technologies, state of the art and future perspectives." *CIRP annals* 52, no. 2 (2003): 589-609. doi: 10.1016/S0007-8506(07)60206-6

[33] Santos, Edson Costa, Masanari Shiomi, Kozo Osakada, and Tahar Laoui. "Rapid manufacturing of metal components by laser forming." *International Journal of Machine Tools and Manufacture* 46, no. 12-13 (2006): 1459-1468. doi: 10.1016/j.ijmachtools.2005.09.005

[34] Vastola, Guglielmo, Gang Zhang, Qingxiang Pei, and Yong-Wei Zhang. “Controlling of residual stress in additive manufacturing of Ti6Al4V by finite element modeling”. *Additive Manufacturing* 12, part B (2016): 231-239. doi: 10.1016/j.addma.2016.05.010

[35] Roberts, Ibiye Aseibichin, C. J. Wang, R. Esterlein, M. Stanford, and D. J. Mynors. "A three-dimensional finite element analysis of the temperature field during laser melting of metal powders in additive layer manufacturing." *International Journal of Machine Tools and Manufacture* 49, no. 12-13 (2009): 916-923. doi: 10.1016/j.ijmachtools.2009.07.004

[36] Gao, Wei, Yunbo Zhang, Devarajan Ramanujan, Karthik Ramani, Yong Chen, Christopher B. Williams, Charlie CL Wang, Yung C. Shin, Song Zhang, and Pablo D. Zavattieri. "The status, challenges, and future of additive manufacturing in engineering." *Computer-Aided Design* 69 (2015): 65-89. doi: 10.1016/j.cad.2015.04.001

[37] Calignano, F. "Design optimization of supports for overhanging structures in aluminum and titanium alloys by selective laser melting." *Materials & Design* 64 (2014): 203-213. doi: 10.1016/j.matdes.2014.07.043

[38] Kempen, Karolien, Lore Thijs, Jan Van Humbeeck, and J-P. Kruth. "Mechanical properties of AlSi10Mg produced by selective laser melting." *Physics Procedia* 39 (2012): 439-446. doi: 10.1016/j.phpro.2012.10.059

[39] Vilaro, Thomas, Stephane Abed, and Wolfgang Knapp. "Direct manufacturing of technical parts using selective laser melting: example of automotive application." In *Proc. of 12th European Forum on Rapid Prototyping*. 2008.

[40] ASM International. Handbook Committee, ed. *Properties and selection: nonferrous alloys and special-purpose materials*. Vol. 2. ASM Intl, 1990.

[41] Louvis, Eleftherios, Peter Fox, and Christopher J. Sutcliffe. "Selective laser melting of aluminum components." *Journal of Materials Processing Technology* 211, no. 2 (2011): 275-284. doi: 10.1016/j.jmatprotec.2010.09.019

[42] Wong, Matthew, Sozon Tsopanos, Chris J. Sutcliffe, and Ieuan Owen. "Selective laser melting of heat transfer devices." *Rapid Prototyping Journal* 13, no. 5 (2007): 291-297. doi: 10.1108/13552540710824797

[43] Aboulkhair, Nesma T., Nicola M. Everitt, Ian Ashcroft, and Chris Tuck. "Reducing porosity in AlSi10Mg parts processed by selective laser melting." *Additive Manufacturing* 1 (2014): 77-86. doi: 10.1016/j.addma.2014.08.001

[44] Boivineau, M., Claus Cagran, D. Doytier, V. Eyraud, M-H. Nadal, Boris Wilthan, and Gernot Pottlacher. "Thermophysical properties of solid and liquid Ti-6Al-4V (TA6V) alloy." *International journal of thermophysics* 27, no. 2 (2006): 507-529. doi: 10.1007/PL00021868

[45] Duerig, T. W., and A. R. Pelton. "Materials properties handbook: titanium alloys." *Materials Park, OH: ASM International, The Materials Information Society* (1994).

[46] Bauccio, Michael, ed. *ASM metals reference book*. ASM international, 1993.

[47] Schreuder, Duco. Outdoor lighting: physics, vision, and perception. Dordrecht: Springer, 2008.

[48] Macleod, H. Angus, and H. Angus Macleod. *Thin-film optical filters*. CRC press, 2010.

[49] Standard, A. S. T. M. "Standard test methods for flow rate of metal powders using the hall flowmeter funnel." (2013). doi: 10.1520/B0213-13

[50] Thijs, Lore, Karolien Kempen, Jean-Pierre Kruth, and Jan Van Humbeeck. "Fine-structured aluminum products with controllable texture by selective laser melting of pre-alloyed AlSi10Mg powder." *Acta Materialia* 61, no. 5 (2013): 1809-1819. doi: 10.1016/j.actamat.2012.11.052

[51] Louvis, Eleftherios, Peter Fox, and Christopher J. Sutcliffe. "Selective laser melting of aluminum components." *Journal of Materials Processing Technology* 211, no. 2 (2011): 275-284. doi: 10.1016/j.jmatprotec.2010.09.019

[52] Nandy, Jyotirmoy, Hrushikesh Sarangi, and Seshadev Sahoo. "Modeling of microstructure evolution in direct metal laser sintering: a phase field approach." In *IOP Conference Series: Materials Science and Engineering*, vol. 178, no. 1, p. 012028. IOP Publishing, 2017. doi: 10.1088/1757-899X/178/1/012028

[53] Shiomi, M., K. Osakada, K. Nakamura, T. Yamashita, and F. Abe. "Residual stress within metallic model made by selective laser melting process." *CIRP Annals* 53, no. 1 (2004): 195-198. doi: 10.1016/S0007-8506(07)60677-5

[54] Mercelis, Peter, and Jean-Pierre Kruth. "Residual stresses in selective laser sintering and selective laser melting." *Rapid prototyping journal* 12, no. 5 (2006): 254-265. doi: 10.1108/13552540610707013

[55] Ganeriwala, R. K., M. Strantza, W. E. King, B. Clausen, T. Q. Phan, L. E. Levine, D. W. Brown, and N. E. Hodge. "Evaluation of a thermomechanical model for prediction of residual stress during laser powder bed fusion of Ti-6Al-4V." *Additive Manufacturing* 27 (2019): 489-502. doi: 10.1016/j.addma.2019.03.034

[56] Dunbar, A.J., E.R. Denlinger, J. Heigel, P. Michaleris, P. Guerrier, R. Martukanitz, and T.W. Simpson. “Development of experimental method for in situ distortion and temperature measurements during the laser powder bed fusion additive manufacturing process”. *Additive Manufacturing* 12, part A (2016): 5-30. doi: 10.1016/j.addma.2016.04.007

[57] Zaeh, Michael F., and Gregor Branner. "Investigations on residual stresses and deformations in selective laser melting." *Production Engineering* 4, no. 1 (2010): 35-45. doi: 10.1007/s11740-009-0192-y

[58] Dunbar, Alexander J., Erik R. Denlinger, Michael F. Gouge, and Pan Michaleris. "Experimental validation of finite element modeling for laser powder bed fusion deformation." *Additive Manufacturing* 12 (2016): 108-120. doi: 10.1016/j.addma.2016.08.003

[59] Yaghi, Anas, Sabino Ayvar-Soberanis, Shanmukha Moturu, Ravi Bilkhu, and Shukri Afazov. "Design against distortion for additive manufacturing." *Additive Manufacturing* 27 (2019): 224-235. doi: 10.1016/j.addma.2019.03.010

[60] Yaghi, A., S. Afazov, A. Holloway, and W. Denmark. "Comparison of fast finite element modelling techniques for prediction of distortion and residual stresses in laser powder bed fusion." *Design and Manufacturing Simulation of Additive Manufacturing* (2017).

[61] Yang, Y. P., M. Jamshidinia, P. Boulware, and S. M. Kelly. "Prediction of microstructure, residual stress, and deformation in laser powder bed fusion process." Computational Mechanics 61, no. 5 (2018): 599-615. doi: 10.1007/s00466-017-1528-7

[62] Papadakis, L., A. Loizou, J. Risse, and J. Schrage. "Numerical computation of component shape distortion manufactured by selective laser melting." *Procedia CIRP* 18 (2014): 90-95. doi: 10.1016/j.procir.2014.06.113

[63] Gouge, Michael, Pan Michaleris, Erik Denlinger, and Jeff Irwin. "The Finite Element Method for the Thermo-Mechanical Modeling of Additive Manufacturing Processes." In *Thermo-Mechanical Modeling of Additive Manufacturing*, pp. 19-38. Butterworth-Heinemann, 2018.

[64] “ASTM F3318-18: Additive Manufacturing – Finished Part Properties – Specification for AlSi10Mg with Powder Bed Fusion – Laser Beam”. *ASTM International* (2018). doi: 10.1520/F3318-18

[65] "AMS 2771: Heat Treatment of Aluminum Alloy Castings." *SAE International* (1987).